

ABSTRACT

Title of Dissertation: GRAVITY DRIVEN INSTABILITIES OF
TRANSIENT DIFFUSIVE BOUNDARY
LAYERS IN POROUS MEDIA

Don Daniel, Doctor of Philosophy, 2014

Dissertation directed by: Assistant Professor Amir Riaz
Department of Mechanical Engineering

This study is motivated by the geological storage of carbon dioxide in subsurface saline aquifers. After injection in an aquifer, CO_2 dissolves in brine to form a diffusive solute boundary layer that is gravitationally unstable leading to natural convection within the aquifer. The exploration of the underlying hydrodynamic instability is of practical importance because of enhanced CO_2 dissolution and storage in aquifers. In comparison to the classical Rayleigh-Bénard convection in a heated fluid cell, the analysis is not straightforward because the CO_2 boundary layer is unsteady and nonlinear. The physics of the convective instability is described by a mathematical operator that is both non-autonomous and non-normal. Consequently, it is uncertain whether classical stability results for the onset of convection are valid. In addition, it is unclear how theoretical predictions compare with experiments.

To explore these issues, the physical mechanisms and perturbation structures of transient, diffusive boundary layers are examined using multiple theoretical and computational tools. Traditional schemes based on linear stability theory, due to unique physical constraints, are unlikely to produce physically relevant perturbation structures. Therefore, a novel optimization procedure is formulated such that the optimization is restricted to physically admissible fields. The new method is compared with traditional stability approaches such as quasi-steady eigenvalue and classical optimization procedures along with fully resolved nonlinear direct numerical simulations.

After establishing a suitable analytical framework, the role of viscosity and permeability variation is examined on the onset of natural convection. Onset of convection occurs sooner when viscosity decreases with aquifer depth. These effects of viscosity variation are in contrast to observations in classical viscous fingering problems. When the porous medium is horizontally layered, qualitatively different instability characteristics can occur depending on the relative length scales of the boundary layer and the permeability variation. For sufficiently high permeability

contrast, small changes in the permeability field can lead to large variations in the onset times for convection. Resonance effects are observed only when the porous medium is vertically layered. The current study provides a framework to explore gravity driven instabilities arising both in pure fluid and porous media applications. The framework can be extended to study more complex systems such as those involving chemically reacting species and random anisotropic permeability fields.

GRAVITY DRIVEN INSTABILITIES OF TRANSIENT
DIFFUSIVE BOUNDARY LAYERS IN POROUS MEDIA

by

Don Daniel

Dissertation submitted to the Faculty of the Graduate School of the
University of Maryland, College Park in partial fulfillment
of the requirements for the degree of
Doctor of Philosophy
2014

Advisory Committee:

Assistant Professor Amir Riaz, Chair/Advisor,

Professor Bala Balachandran,

Professor James Duncan,

Professor Kenneth Kiger,

Professor Dianne P. O'Leary, Dean's Representative.

© Copyright by
Don Daniel
2014

Dedication

To Issac Samuel and David Daniel!

Acknowledgments

To my Ph.D. advisor Amir Riaz for timely research guidance, care and for providing me with a very strong learning platform.

To Nils Tilton for several important discussions in improving my research and writing skills, especially during his post-doc stint at the University of Maryland.

To Hamdi Tchelepi for insightful discussions and collaboration opportunities.

To Azar Nazeri and the Petroleum Institute, Abu Dhabi for funding during various stages of my academic career.

To my dissertation defense and proposal committee members, Bala Balachandran, Dianne P. O’Leary, James Duncan, Kenneth Kiger, and Konstantina Trivisa for helpful suggestions and recommendations that aided in the prompt completion of this dissertation.

To my colleagues for their valuable discussions, input, and support over the years: Marcos Vanella, Grigoris Panagakos, Khaled Abdelaziz, Clarence Baney, Moon Soo Lee, Mohammad Alizadeh, Zhipeng Qin, Abishek Gopal, Siavash Toosi, Zohreh Ghorbani, Kevin Shipley, and Meiqian Chen.

To friends and acquaintances: O.V. Kiran, Ben Jacob, Bonney Luke Thomas, Deepu Prasad, Ashraf T. P., Rohit Jacob, Ajay Mathew Thomas, Vaishag, Jithin, Siddarth Sashidharan, Ebrahim Kheriwala, and others for having helped me in ways that I sometimes do not perceive. Thank you.

To the many kind authors who provided free open source information on several topics such as tutorials on Matlab, Latex, etc, all of which helped me in completing

my academic and research work in an efficient manner.

To my family: mom Susen Daniel, dad Geevarghese Daniel Kutty, sister-in-law Sarah Daniel, brother Dan Daniel for understanding and love.

To all my spiritual guides!

To my dear God in whom I live, I breath, and I have my being!

Table of Contents

| | |
|--|------|
| List of Tables | vii |
| List of Figures | viii |
| List of Abbreviations | x |
| 1 Introduction | 1 |
| 1.1 Motivation | 1 |
| 1.2 Review | 3 |
| 1.3 Challenges and Objectives | 8 |
| 1.4 Outline of Dissertation | 10 |
| 2 Natural convection in homogeneous porous media | 12 |
| 2.1 Overview | 12 |
| 2.2 Geometry and governing equations | 13 |
| 2.3 Linear stability methods | 15 |
| 2.3.1 Quasi-steady eigenvalue analysis | 15 |
| 2.3.2 Classical Optimization | 16 |
| 2.4 Results | 20 |
| 2.4.1 Effect of amplification measure | 20 |
| 2.4.2 Optimal perturbation structures | 24 |
| 2.4.3 Sensitivity to initial perturbation time | 26 |
| 2.4.4 Influence of final time on initial perturbation profiles | 34 |
| 2.4.5 Comparison with quasi-steady eigenvalue analysis | 36 |
| 2.5 Modified Optimization Procedure | 39 |
| 2.5.1 Methodology | 41 |
| 2.5.2 Filter Functions | 42 |
| 2.5.3 Comparison with classical optimization scheme | 44 |
| 2.5.4 Comparison with eigenvalue and initial value problems | 50 |
| 2.6 Direct Numerical Simulations | 53 |
| 2.6.1 Simulations of physical systems | 53 |
| 2.6.2 Extent of linear regime and onset of convection | 56 |
| 2.7 Conclusions and summary | 59 |

| | | |
|-------|--|-----|
| 3 | Effect of viscosity contrast on gravity-driven instabilities in porous media | 63 |
| 3.1 | Overview | 64 |
| 3.2 | Governing equations | 67 |
| 3.3 | Results and discussion | 73 |
| 3.3.1 | The fixed interface model | 73 |
| 3.3.2 | The moving interface model | 80 |
| 3.3.3 | Effect of non-monotonic density profiles | 82 |
| 3.3.4 | Effect of uniform flow | 88 |
| 3.4 | Conclusions | 95 |
| 4 | Natural convection in horizontally layered porous media | 98 |
| 4.1 | Overview | 98 |
| 4.2 | Governing equations | 100 |
| 4.3 | Linear perturbation growth | 103 |
| 4.3.1 | Influence of permeability variance and phase | 104 |
| 4.3.2 | Stability mechanisms | 106 |
| 4.3.3 | Effect of correlation length | 111 |
| 4.4 | Onset of natural convection | 114 |
| 4.4.1 | Critical time of convection onset | 116 |
| 4.4.2 | Influence of mode switching on convection onset | 118 |
| 4.5 | Conclusions | 121 |
| 5 | Natural convection in vertically layered porous media | 123 |
| 5.1 | Overview | 123 |
| 5.2 | Governing equations and methodology | 124 |
| 5.3 | Linear growth characteristics | 128 |
| 5.3.1 | Quasi-steady 2D eigenmodes | 128 |
| 5.3.2 | Perturbation growth | 130 |
| 5.3.3 | Scaling with Rayleigh number | 134 |
| 5.4 | Onset of natural convection | 135 |
| 5.5 | Conclusions | 139 |
| 6 | Contributions and Future work | 140 |
| 6.1 | Contributions | 140 |
| 6.2 | Future work | 141 |

List of Tables

| | | |
|-----|--|-----|
| 2.1 | Negative concentrations of classical optimal profiles | 39 |
| 2.2 | Gaussian parameters for Direct Numerical Simulation | 54 |
| 3.1 | Vorticity components in the fixed interface model | 76 |
| 3.2 | Vorticity components in the displaced interface model | 91 |
| 4.1 | Vorticity components due to permeability heterogeneity | 110 |

List of Figures

| | | |
|------|---|----|
| 1.1 | Sketch of CO ₂ sequestration | 2 |
| 1.2 | Dissolution flux of CO ₂ | 6 |
| | | |
| 2.1 | Geometry of study | 13 |
| 2.2 | Optimization results when maximizing various amplification measures | 21 |
| 2.3 | Dominant perturbations | 25 |
| 2.4 | Effect of initial perturbation time | 28 |
| 2.5 | Effect of initial time on perturbation profiles | 29 |
| 2.6 | Optimal point | 31 |
| 2.7 | Convergence of the optimal initial profiles | 34 |
| 2.8 | IVP results using random initial profiles | 35 |
| 2.9 | Comparing optimal perturbations with least stable QSSA mode | 37 |
| 2.10 | Optimization using filter functions, Ψ_1 and Ψ_2 | 42 |
| 2.11 | Optimization using filter function Ψ_3 | 45 |
| 2.12 | Comparison of the COP and MOP schemes | 46 |
| 2.13 | Optimal MOP point | 49 |
| 2.14 | Comparison of MOP with QSSA _{ξ} and IVP | 51 |
| 2.15 | Validation of MOP with randomly perturbed DNS | 55 |
| 2.16 | Onset of nonlinear convection – MOP and COP | 57 |
| | | |
| 3.1 | Sketch of CO ₂ sequestration | 66 |
| 3.2 | Nonmonotonic density and viscosity profiles | 67 |
| 3.3 | Various types of transient boundary layers | 70 |
| 3.4 | Marginal stability contours of FI model | 72 |
| 3.5 | Most dominant growthrates and wavenumbers of FI model | 75 |
| 3.6 | Eigenmodes of FI model | 76 |
| 3.7 | Comparison between MI and FI models | 78 |
| 3.8 | Agreement between FI and MI models | 79 |
| 3.9 | Eigenmodes of MI model | 83 |
| 3.10 | Effect of varying nonmonotonicity of density variation | 84 |
| 3.11 | Effect of density profiles on velocity eigenmode | 86 |
| 3.12 | Critical viscosity ratio of the displaced interface model. | 89 |
| 3.13 | Effect of displacement velocity on the velocity eigenmode | 93 |

| | | |
|------|--|-----|
| 3.14 | Time invariance of critical viscosity ratio | 94 |
| 4.1 | Marginal stability contours of zero growth rate | 104 |
| 4.2 | Perturbation and permeability profiles | 107 |
| 4.3 | Spatial variation of vorticity | 109 |
| 4.4 | Marginal stability contours for permeability phase of zero | 111 |
| 4.5 | Spatial variation of perturbation and vorticity | 112 |
| 4.6 | Critical time for the onset of instability | 114 |
| 4.7 | Onset of convection | 116 |
| 4.8 | Role of perturbation amplitude | 120 |
| 5.1 | Quasi-steady 2D eigenmodes | 127 |
| 5.2 | Fourier components of 2D eigenmode | 129 |
| 5.3 | Temporal evolution of growth rate | 131 |
| 5.4 | Effect of permeability amplitude | 132 |
| 5.5 | Scaling with Rayleigh number | 134 |
| 5.6 | Critical onset of natural convection | 138 |

List of Abbreviations

| | |
|----------------------------------|---|
| NOAA | National Oceanic and Atmospheric Administration |
| ESRL | Earth System Research Laboratory |
| EVP | Eigenvalue Problem |
| QSSA | Quasi-Steady EVP |
| QSSA _{ξ} | QSSA in transformed space |
| COP | Classical Optimization Procedure |
| MOP | Modified Optimization procedure |
| DNS | Direct Numerical Simulations |
| IVP | Initial Value Problem |
| FI | Fixed Interface model |
| MI | Moving Interface model |
| DMA | Dominant Mode Analysis |

Chapter 1: Introduction

1.1 Motivation

The past decades have seen a rapid increase in the man-made production of greenhouse gases such as carbon dioxide. Recent estimates of the concentration of atmospheric CO₂ are at an all time high of about 397 ppm (NOAA-ESRL, 2014). The primary sources of CO₂ emissions are attributed to the combustion of fossil fuels in power plants. To reduce emissions, it has been proposed to store CO₂ in subsurface porous rock formations (Orr, 2009). The process of capturing and storing CO₂ is referred to in past literature as CO₂ sequestration.

According to the sequestration procedure, CO₂ would be captured from power plants and then injected into brine-saturated aquifers with large storage capacity. CO₂ is stored within rocks through a combination of several mechanisms such as:

- *Structural trapping*

This trapping occurs when a layer of impermeable caprock prevents CO₂ from leaking back into the atmosphere.

- *Residual trapping*

This occurs due to capillary trapping of CO₂ within small pore spaces.

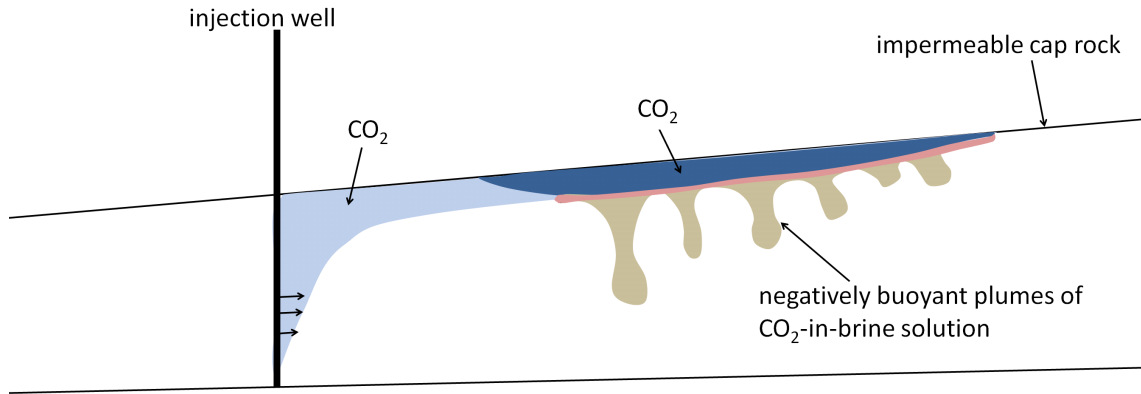


Figure 1.1: Sketch of CO₂ sequestration process

- *Mineral trapping*

Given sufficient time, CO₂ reacts with surrounding brine in aquifer to form stable carbonate minerals.

- *Solubility trapping*

CO₂ dissolves into the surrounding brine and thus stored within the brine.

This study explores the fluid mechanics of the solubility trapping mechanism. A schematic of the process is shown in figure 1. After injection, the buoyant CO₂ initially rises and forms a horizontal layer beneath an impermeable caprock. With time, free CO₂ dissolves into the underlying brine across the two-phase interface and forms a downwardly growing diffusive boundary layer. Because the CO₂-rich brine in the boundary layer is denser than the underlying brine, a gravitational instability eventually results in finger-like structures that break away from the boundary layer and convect CO₂ downwards into the aquifer. Due to the ensuing natural convection, free CO₂ dissolves more faster into the brine. A clear understanding of the physical

mechanisms behind natural convection is vital to the modelling of CO₂ sequestration (Huppert & Neufeld, 2014; Riaz & Cinar, 2014).

1.2 Review

A gravitational instability usually occurs when a heavier fluid is present above a lighter fluid. When the interface between the two fluids is perturbed, the fluids interpenetrate to produce buoyant unstable fingers. Such an instability, which is referred to in literature as the Rayleigh–Taylor instability (Drazin & Reid, 2004), is observable in a wide scale of systems ranging from a modern lava lamp to the outer atmosphere of the sun. Similar instabilities are also formed when unstable density distributions exist within a single fluid, as in the case of Rayleigh–Bénard convection. In this classical scenario, a horizontal layer fluid is heated from below such that a linear temperature profile is formed within the fluid, leading to a buoyancy-driven convection. For many natural phenomena, convection occurs well before the formation of the linear temperature profile, because of strong unfavorable density gradients within the developing thermal boundary layer. This form of early onset of natural convection in a transient, developing boundary layer is a common feature of several important porous media applications such as CO₂ sequestration and groundwater flow (Wooding *et al.*, 1997) as well as pure fluid applications such as heat transfer devices (Goldstein, 1959).

The onset of natural convection can be explored using analogous experiments in laboratory conditions (Blair & Quinn, 1969). In addition to experiments, they can

also be analyzed using various theoretical methods. One popular method is to examine the eigenvalues of the operator or matrix that describes the physical evolution of instabilities. Instabilities are also investigated by performing a computational simulation of the nonlinear equations that govern the physics. This dissertation explores gravity-driven instabilities that lead to natural convection in transient, diffusive boundary layers using a combination of theoretical and computational methods.

The archetypal problem of Rayleigh–Bénard convection in which a horizontal fluid heated from below is well understood as the underlying thermal gradient or boundary layer is steady and linear. The stability characteristics are determined by the dimensionless Rayleigh number, which is the ratio of the destabilizing buoyancy forces that drive convection to the stabilizing effects of diffusion. Convection occurs when the thermal gradients are strong enough to drive motion. Similar behavior is also observed for porous media flows (Horton & Rogers, 1945; Lapwood, 1948). For the classical Rayleigh–Bénard convection, there is excellent agreement between experiments and theory.

In comparison to classical Rayleigh–Bénard convection, the diffusive boundary layers of CO₂ sequestration are unsteady and nonlinear. This renders the linear stability operator non-autonomous. In comparison, popular stability operators in fluid mechanics such as the Orr–Sommerfeld operator are not a function of time (Reddy *et al.*, 1993). Furthermore, the governing equations are also non-self-adjoint and the resultant eigenmodes are non-orthogonal. The superposition of non-orthogonal eigenmodes may result in transient growth (Schmid, 2007). Because of these effects, it is uncertain whether existing theoretical methods predict the physics accurately.

It is also unclear how theoretical and experimental methods of transient boundary layers compare with each other.

Earlier experimental studies provide a sound qualitative understanding of the evolution of transient diffusive boundary layers (Blair & Quinn, 1969; Elder, 1968). In the early stages of the boundary layer formation, perturbations to the layer are damped due to an *initial diffusive period* during which the stabilizing effects of viscosity dominate the physics. Eventually a *critical time* is reached at which the vertical density gradient is sufficient to drive fluid motion (Foster, 1965; Goldstein, 1959) such that perturbations begin to grow. Computational simulations suggest that for small initial perturbations, nonlinear effects increase slowly and, linear mechanisms can dominate for considerable time beyond the critical onset time for instabilities (Farajzadeh *et al.*, 2007; Riaz *et al.*, 2006; Selim & Rees, 2007*b*). Within this linear regime, the flux of CO₂ into the brine decreases monotonically, see figure 1.2. Eventually nonlinear mechanisms cause the flux of CO₂ to increase from that predicted by linear theory such that there is a turning point across which flux starts to increase. This turning point is referred to as the *onset time of natural convection*.

The linear stability of diffusive boundary layers has been studied using three main approaches. The quasi-steady-state approach (QSSA) approximates the boundary layer as steady in comparison to the rapid growth of perturbations. The method was first applied to convection in fluid layers by Morton (1957), Goldstein (1959), and Lick (1965), and subsequently to porous layers by Robinson (1976). The QSSA is considered to be invalid for small times when the boundary layer grows rapidly. The stability of diffusive boundary layers has also been studied using energy meth-

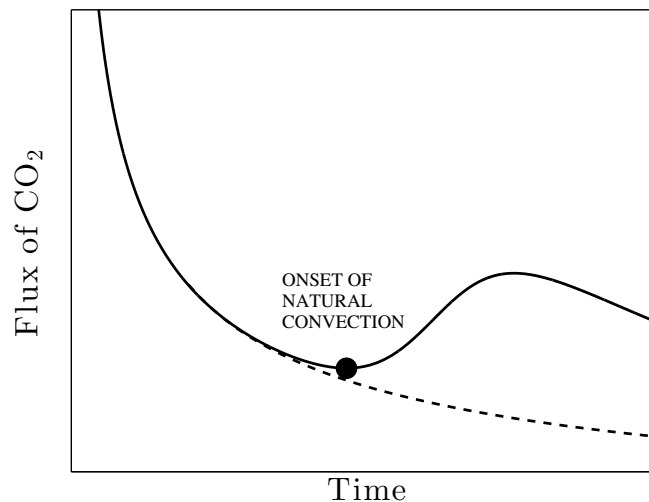


Figure 1.2: Dissolution flux of CO_2 (solid line) into brine. The diffusive flux (dashed line) corresponds to the linear regime. Nonlinear effects begin to dominate at the onset of natural convection (solid dot).

ods (Caltagirone, 1980; Homsy, 1973; Kim & Choi, 2007; Slim & Ramakrishnan, 2010). These methods determine lower bounds below which all perturbations decay, but do not provide information for the subsequent evolution of unstable perturbations in the linear regime. The third, and most popular, approach avoids the QSSA by solving the non-autonomous, linear, initial value problem (IVP) numerically for given initial conditions.

The IVP was first considered by Foster (1965) to study thermal convection in pure fluid media. Foster focused on white noise initial conditions that excited all vertical Fourier modes equally. Gresho & Sani (1971) noted several drawbacks to this approach. First, white noise conditions produce initial temperature perturbations that vary far outside the boundary layer. In experiments, however, perturbations originate in the boundary layer (Blair & Quinn, 1969; Elder, 1968; Green & Foster,

1975; Spangenberg & Rowland, 1961; Wooding *et al.*, 1997). Second, initial conditions may play a secondary role in systems continuously forced by noise. Lastly, the onset time for convection is due to nonlinear effects and cannot be predicted by the linear IVP. Subsequently, Jhaveri & Homsy (1982) modelled noise by adding random forcing to the momentum equation and reported good agreement with experiments.

The IVP for thermal boundary layers in porous media was first considered by Caltagirone (1980) and Kaviany (1984), and subsequently applied to CO₂ sequestration by Ennis-King & Paterson (2005). All three studies used initial white noise conditions that spanned the entire domain. However, these initial conditions contradict previous experimental observations that suggest that perturbations originate within the boundary layer. Consequently, two methods have emerged that suggest more appropriate initial conditions for the IVP. The first approach (Ben *et al.*, 2002; Kim & Choi, 2011; Riaz *et al.*, 2006) involves a similarity transformation of the linear stability operator. As a result, the newly transformed eigenmodes are always localized within the boundary layer. Riaz *et al.* (2006) also developed the “dominant mode analysis” (DMA) that involved a projection of the dynamics onto a weighted Hermite polynomial. This technique produced analytical expressions for onset time that showed good agreement with corresponding results of IVP simulations.

The second approach to determining initial conditions for the IVP uses non-modal stability theory (Farrell & Ioannou, 1996*a,b*; Schmid, 2007) to determine optimal initial perturbations with maximum amplification over a certain period of time. In this manner, Rapaka *et al.* (2008), using a singular value decomposition method, showed that optimal perturbations tend to be more localized within the boundary

layer than white noise conditions. Subsequently, Doumenc *et al.* (2010) studied non-modal growth in transient Rayleigh-Bénard-Marangoni convection. This was performed using an adjoint-based method. An approach similar to that of Rapaka *et al.* (2008) or Doumenc *et al.* (2010) is to optimize for the growth rate by formulating an eigenvalue problem to determine the numerical abscissa. This approach has been taken by Slim & Ramakrishnan (2010) and Kim & Choi (2012).

1.3 Challenges and Objectives

Though the stability of diffusive boundary layers has been studied extensively using multiple methods, it is still uncertain which methodology best reflects the physics of the problem. This uncertainty is best illustrated by examining recent works. Ghesmat *et al.* (2011) performed a QSSA eigenvalue analysis to study the effect of chemical reactions within the boundary layer. Elenius *et al.* (2012) employed a self-similar QSSA eigenvalue analysis to investigate the effect of a capillary transition zone above the transient boundary layer. Meanwhile, Cheng *et al.* (2012) investigated the effect of permeability anisotropy using the method of Slim & Ramakrishnan (2010). Because of uncertainties in methodology, comparing experimental and theoretical studies is not straightforward.

In addition, there are other challenges in relating theoretical and experimental studies of transient diffusive boundary layers. For example, the linear stability analyses (Ennis-King *et al.*, 2003; Riaz *et al.*, 2006; Selim & Rees, 2007*a*) of CO₂ solute boundary layers employ a constant viscosity. On the other hand, experimental

studies (Backhaus *et al.*, 2011), due to practical limitations, use miscible fluids with large viscosity contrast. It is therefore important to characterize the effect of fluid viscosity within the boundary layer.

An important measure for subsurface flows is the permeability of the porous medium. The magnitude of permeability signifies the ability of the fluid to move with ease through the porous medium. Typical aquifers are made of sedimentary rocks with grain sizes varying from coarser sand to finer clay, which in turn causes permeability to change within position (Bear, 1988). Depending on grain shape, permeability may also be anisotropic due to preferential flow in a particular direction. Currently, there is no clear understanding on the effect of a spatially varying permeability field on the onset times for natural convection in transient boundary layers. Though the effect of permeability anisotropy on transient boundary layers have been addressed by some studies (Cheng *et al.*, 2012; Ennis-King & Paterson, 2005; Rapaka *et al.*, 2009; Xu *et al.*, 2006), the linear stability of transient boundary layers in an aquifer with vertically (Rapaka *et al.*, 2009) and horizontally varying permeability is less explored. This is partly because of complications in the theoretical formulation of the linear stability problem especially in the case of a horizontally varying permeability field.

The current study addresses these issues by

- developing a robust physical basis from which to study the influence of physical effects, such as permeability heterogeneity and anisotropy as well as chemically active boundary layers.

- investigating the role of viscosity on transient boundary layers, and to relate experimental and theoretical studies.
- exploring the effect of vertical and horizontal variations in the permeability field.

1.4 Outline of Dissertation

Chapter 2 explores the onset of natural convection in homogeneous isotropic porous media using a combination of linear stability analysis and direct numerical simulations. Various linear stability approaches are investigated simultaneously in order to develop a robust analytical framework. A new optimization procedure to analyze the onset of instabilities is proposed.

Chapter 3 examines the effect of viscosity contrast on the linear stability of transient, diffusive layers in porous media. This analysis helps evaluate experimental observations of various boundary layer models that are commonly used to study CO₂ sequestration. Comparisons are also made with classical viscous fingering systems.

Chapter 4 explores the stability of transient diffusive boundary layers in a horizontally layered porous medium. Permeability is assumed to vary periodically along the direction of the unstable gravity force. The behavior of instability is studied with respect to modes of vorticity production related to the coupling of perturbations with the magnitude and gradients of permeability.

Chapter 5 analyzes the onset of natural convection in a vertically layered porous medium. The results are obtained using multi-dimensional eigenvalue prob-

lems and non-linear direct numerical simulations.

Finally, Chapter 6 lists the journal publications produced by this study. Avenues for future research are suggested.

Chapter 2: Natural convection in homogeneous porous media

2.1 Overview

In this chapter, it is shown that classical optimal perturbation profiles that maximize perturbation amplification cannot lead to onset of convection in finite time. Rather, onset of convection results from the growth of “suboptimal” perturbations localized within the diffusive boundary layer. The chapter is divided into three broad categories: (i) analysis of the classical optimization procedure; (ii) development of a new methodology to study constrained optimal perturbations; and (iii) validation that the new approach predicts optimal perturbations closely related to physical systems.

This chapter is organized as follows. The governing equations are presented in §2.2. The classical modal and nonmodal approaches are described in §2.3. The classical optimization results are presented in §2.4. The proposed modifications to the classical optimization procedure and associated results are presented in §2.5. DNS results are reported in §2.6. The main findings are summarized in §2.7.

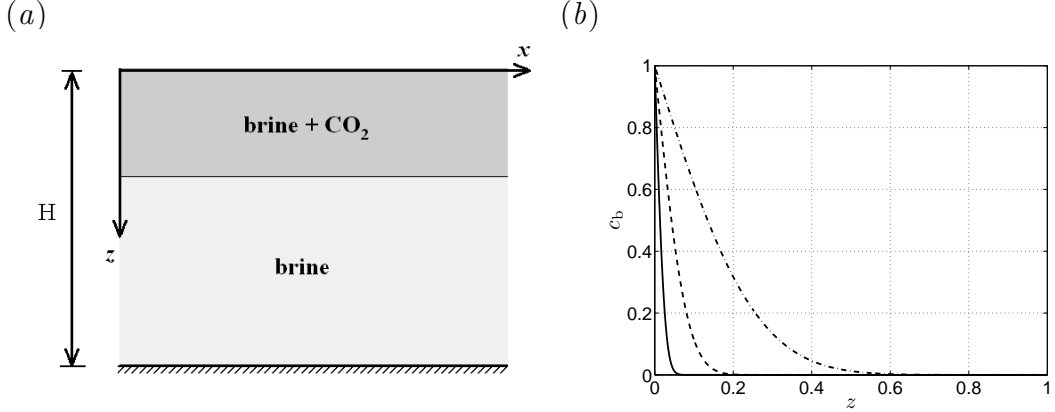


Figure 2.1: (a) Sketch, not to scale, of the geometry considered in this study. (b) Base-state (2.3) for $Ra = 500$ and $t = 0.1$ (solid line), $t = 1$ (dashed line), and $t = 10$ (dash-dotted line).

2.2 Geometry and governing equations

Due to the fundamental nature of the current study, the porous medium is modeled as being fluid-saturated, isotropic, homogeneous, of infinite horizontal extent in the x and y directions, and of finite depth H in the vertical z direction, see figure 2.1(a). The vertical z direction is positive in the downward direction of gravity, g . The domain is bounded by an impermeable wall at $z = H$. The top boundary at $z = 0$ represents the fixed two-phase interface between CO_2 gas and CO_2 -saturated brine. The porous medium is characterized by its permeability, K , dispersivity, D , and porosity, ϕ , respectively. Initially, the brine is quiescent with zero CO_2 concentration, $c = 0$, and constant density, $\rho = \rho_0$. At time $t = 0$, saturated brine is supplied at $z = 0$ with a constant concentration $c = C_1$ and density ρ_1 . The fluid viscosity, μ , is assumed to be constant. The density difference $\Delta\rho = \rho_1 - \rho_0$

is assumed to be much less than ρ_0 , i.e. $\Delta\rho \ll \rho_0$.

Fluid flow and mass transport in the porous medium are governed by Darcy's law and volume averaged forms of the continuity and advection-diffusion equations (Whitaker, 1999). The governing equations are written in nondimensional form as,

$$\mathbf{v} + \nabla p - c\mathbf{e}_z = 0, \quad \nabla \cdot \mathbf{v} = 0, \quad \frac{\partial c}{\partial t} + \mathbf{v} \cdot \nabla c - \frac{1}{Ra} \nabla^2 c = 0, \quad (2.1)$$

using the characteristic length $L = H$, time $T = \phi H/U$, buoyancy velocity $U = K\Delta\rho g/\mu$, pressure $P = \Delta\rho gH$, and concentration $C = C_1$. The dimensionless equations (2.1) have been obtained using the Boussinesq approximation and a linear fluid density profile, $\rho = \rho_0 + \Delta\rho(c/C_1)$. The Rayleigh number is defined as $Ra = UH/(\phi D)$. The symbol $\mathbf{v} = [u, v, w]$ is the nondimensional velocity vector, c is the nondimensional concentration and p is the nondimensional pressure obtained from the dimensional pressure \hat{p} through the relation $p = (\hat{p} - \rho_0 g z)/P$. The symbol \mathbf{e}_z is the unit vector in the z direction. Equations (2.1) must satisfy the following boundary conditions,

$$c \Big|_{z=0} = 1, \quad \frac{\partial c}{\partial z} \Big|_{z=1} = 0, \quad w \Big|_{z=0} = w \Big|_{z=1} = 0, \quad t \geq 0. \quad (2.2)$$

Equations (2.1) admit the transient base state,

$$\mathbf{v}_b = \mathbf{0}, \quad c_b(z, t) = 1 - \frac{4}{\pi} \sum_{n=1}^{\infty} \frac{1}{2n-1} \sin \left[\left(n - \frac{1}{2} \right) \pi z \right] \exp \left[- \left(n - \frac{1}{2} \right)^2 \frac{\pi^2 t}{Ra} \right], \quad (2.3)$$

The linear stability of base-state (2.3) is studied with respect to small wavelike perturbations of the form,

$$\tilde{c} = \hat{c}(z, t)e^{i(\alpha x + \beta y)}, \quad \tilde{\mathbf{v}} = \hat{\mathbf{v}}(z, t)e^{i(\alpha x + \beta y)}, \quad \tilde{p} = \hat{p}(z, t)e^{i(\alpha x + \beta y)}, \quad (2.4)$$

where $i = \sqrt{-1}$, α and β are wavenumbers in the x and y directions respectively, and $\widehat{c}(z, t)$, $\widehat{v}(z, t)$ and $\widehat{p}(z, t)$ are time-dependent perturbation profiles in the z direction. Following the standard procedure (see Riaz *et al.*, 2006), the linear stability problem can be written as the following initial value problem for \widehat{c} and \widehat{w} ,

$$\frac{\partial \widehat{c}}{\partial t} + \widehat{w} \frac{\partial c_b}{\partial z} - \frac{1}{Ra} \mathcal{D} \widehat{c} = 0, \quad \mathcal{D} \widehat{w} + k^2 \widehat{c} = 0, \quad (2.5)$$

$$\widehat{c} \Big|_{z=0} = 0, \quad \frac{\partial \widehat{c}}{\partial z} \Big|_{z=1} = 0, \quad \widehat{w} \Big|_{z=0} = \widehat{w} \Big|_{z=1} = 0, \quad (2.6)$$

where $\mathcal{D} = \partial^2 / \partial z^2 - k^2$ and $k = \sqrt{\alpha^2 + \beta^2}$. Because the base-state is transient, the boundary layer is sensitive to the time at which it is perturbed. The boundary layer is perturbed at time $t = t_p$ with the following initial perturbation profiles,

$$\widehat{c} \Big|_{t=t_p} = c_p(z), \quad \widehat{w} \Big|_{t=t_p} = w_p(z), \quad (2.7)$$

where c_p and w_p must satisfy equations (2.5)–(2.6).

2.3 Linear stability methods

This study explores a wide range of complementary modal and nonmodal analysis methods. The various methods used for the linear stability analysis of equations (2.5)–(2.6) are discussed in this section.

2.3.1 Quasi-steady eigenvalue analysis

The QSSA approach reduces equations (2.5)–(2.6) to an autonomous eigenvalue problem. For a prescribed final time t_f , this approach approximates the base-state, $c_b(z, t)$, as steady and decomposes perturbations into separable functions of

z and t ,

$$\widehat{c} = c_e(z; t_f)e^{\sigma(t_f)t}, \quad \widehat{w} = w_e(z; t_f)e^{\sigma(t_f)t}, \quad (2.8)$$

where $\sigma(t_f)$ is the instantaneous growth rate at $t = t_f$. Substituting (2.8) into (2.5)–(2.6) produces an eigenvalue problem for eigenvalues σ and eigenfunctions c_e and w_e ,

$$\frac{1}{Ra} \left(\frac{d^2}{dz^2} - k^2 \right) c_e + k^2 \frac{\partial c_b}{\partial z} \left(\frac{d^2}{dz^2} - k^2 \right)^{-1} c_e = \sigma c_e, \quad c_e \Big|_{z=0} = \frac{dc_e}{dz} \Big|_{z=1} = 0. \quad (2.9)$$

The QSSA eigenvalue problem can also be written in terms of w_e . In practice, however, solving (2.9) was more stable.

2.3.2 Classical Optimization

The initial perturbation profiles, c_p and w_p , are determined so that the perturbation amplification is maximized at some prescribed final time $t = t_f$. Tan & Homsy (1986) and Doumenc *et al.* (2010) have observed that the perturbation amplification is sensitive to the perturbation flow field used to measure the perturbation magnitude. To investigate how different measures of perturbation magnitude influence nonmodal results, the perturbation magnitude at time t is defined as,

$$E(t) = \int_0^1 [A_1 \widehat{c}(z, t)^2 + A_2 \widehat{w}(z, t)^2 + A_3 \widehat{u}(z, t)^2] dz, \quad (2.10)$$

where A_1, A_2 and A_3 are constants to be defined shortly. The following measures of perturbation amplification, $\Phi(t)$, are studied,

$$\Phi_c(t) = \left[\frac{E(t)}{E(t_p)} \right]^{\frac{1}{2}}, \quad A_1 = 1, \quad A_2 = A_3 = 0, \quad (2.11a)$$

$$\Phi_w(t) = \left[\frac{E(t)}{E(t_p)} \right]^{\frac{1}{2}}, \quad A_2 = 1, \quad A_1 = A_3 = 0, \quad (2.11b)$$

$$\Phi_e(t) = \left[\frac{E(t)}{E(t_p)} \right]^{\frac{1}{2}}, \quad A_1 = A_2 = A_3 = 1. \quad (2.11c)$$

Most previous studies of transient boundary layers measure amplification with respect to the perturbation's concentration field, Φ_c (Caltagirone, 1980; Ennis-King *et al.*, 2003; Kim & Kim, 2005; Rapaka *et al.*, 2008; Tan & Homsy, 1986), or the vertical velocity field, Φ_w (Foster, 1965; Gresho & Sani, 1971; Kaviany, 1984; Tan & Homsy, 1986). In addition, Φ_e is introduced as a measure of perturbation energy that includes both the velocity and concentration fields. $\Phi(t_f)$ is optimized using an adjoint procedure described by Doumenc *et al.* (2010) in which $E(t_f)$ is maximized subject to the constraint that $E(t_p) = 1$. For this purpose, the Lagrangian is defined as,

$$\begin{aligned} \mathcal{L}(\widehat{c}, c^*, \widehat{w}, w^*, \widehat{u}, s) = & E(t_f) - s[E(t_p) - 1] - \int_{t_p}^{t_f} \int_0^1 w^* (\mathcal{D}\widehat{w} + k^2\widehat{c}) \, dz \, dt \\ & - \int_{t_p}^{t_f} \int_0^1 c^* \left(\frac{\partial \widehat{c}}{\partial t} - \frac{1}{Ra} \mathcal{D}\widehat{c} + \widehat{w} \frac{\partial c_b}{\partial z} \right) \, dz \, dt, \end{aligned} \quad (2.12)$$

where s is a scalar Lagrange multiplier and the adjoint variables $c^*(z, t)$ and $w^*(z, t)$ are Lagrange multipliers dependent on z and t . The double integrals on the right-hand-side of (2.12) assure satisfaction of the governing IVP (2.5)–(2.7). To obtain first-order optimality conditions, the variational of the Lagrangian, $\delta\mathcal{L}$, is set to

zero. Integrating by parts, $\delta\mathcal{L}$ can be written as,

$$\begin{aligned}
\delta\mathcal{L} = & \int_0^1 \left[2(A_1\widehat{c}\delta\widehat{c} + A_2\widehat{w}\delta\widehat{w} + A_3\widehat{u}\delta\widehat{u}) - c^*\delta\widehat{c} \right]_{t=t_f} dz \\
& - \int_0^1 \left[2s(A_1\widehat{c}\delta\widehat{c} + A_2\widehat{w}\delta\widehat{w} + A_3\widehat{u}\delta\widehat{u}) - c^*\delta\widehat{c} \right]_{t=t_p} dz \\
& - \int_{t_p}^{t_f} \int_0^1 \left[\delta\widehat{c} \left(-\frac{\partial c^*}{\partial t} - \frac{1}{Ra}\mathcal{D}c^* + k^2w^* \right) + \delta\widehat{w} \left(\mathcal{D}w^* + \frac{\partial c_b}{\partial z}c^* \right) \right] dz dt \\
& + \int_{t_p}^{t_f} \left[\frac{1}{Ra} \left(c^*\frac{\partial\delta\widehat{c}}{\partial z} - \delta\widehat{c}\frac{\partial c^*}{\partial z} \right) - w^*\frac{\partial\delta\widehat{w}}{\partial z} + \delta\widehat{w}\frac{\partial w^*}{\partial z} \right]_{z=0}^{z=1} dt = 0. \tag{2.13}
\end{aligned}$$

The optimality conditions are met when c^* and w^* satisfy the following adjoint problem,

$$-\frac{\partial c^*}{\partial t} - \frac{1}{Ra}\mathcal{D}c^* + k^2w^* = 0, \quad \mathcal{D}w^* = -\frac{\partial c_b}{\partial z}c^*, \tag{2.14}$$

$$c^*\Big|_{z=0} = 0, \quad \frac{\partial c^*}{\partial z}\Big|_{z=1} = 0, \quad w^*\Big|_{z=0} = w^*\Big|_{z=1} = 0, \tag{2.15}$$

along with the following coupling conditions between the adjoint and physical variables,

$$2(A_1\widehat{c}\delta\widehat{c} + A_2\widehat{w}\delta\widehat{w} + A_3\widehat{u}\delta\widehat{u})\Big|_{t=t_f} = c^*\delta\widehat{c}\Big|_{t=t_f}, \tag{2.16}$$

$$2s(A_1\widehat{c}\delta\widehat{c} + A_2\widehat{w}\delta\widehat{w} + A_3\widehat{u}\delta\widehat{u})\Big|_{t=t_p} = c^*\delta\widehat{c}\Big|_{t=t_p}. \tag{2.17}$$

The optimal initial perturbations are found using an iterative procedure. Given an initial guess for c_p and w_p , the IVP (2.5)–(2.7) is integrated forward in time to $t = t_f$. Then the condition (2.16) is used to obtain a final condition for the adjoint IVP (2.14)–(2.15). The adjoint IVP is then integrated backwards in time to $t = t_p$. Then using condition (2.17), one obtains improved initial profiles c_p and w_p . This procedure is repeated until satisfaction of the convergence criteria, $\|c_p^n - c_p^{n-1}\|_\infty / \|c_p^{n-1}\|_\infty \leq 10^{-4}$, where n is the iteration number. The iterative procedure is insensitive to the initial guess; however, the number of iterations is

reduced using $c_p^0 = \xi \exp(-\xi^2)$ where $\xi = z\sqrt{Ra/(4t)}$. The IVPs are solved using standard second-order finite-difference methods.

The application of the coupling conditions (2.16)–(2.17) depends on the definition of the perturbation amplification. When maximizing Φ_c , conditions (2.16)–(2.17) are satisfied for,

$$2\hat{c}\Big|_{t=t_f} = c^*\Big|_{t=t_f}, \quad 2s\hat{c}\Big|_{t=t_p} = c^*\Big|_{t=t_p}. \quad (2.18)$$

The derivation of (2.18) is described by Doumenc *et al.* (2010). When maximizing Φ_w or Φ_e , however, the application of the coupling conditions is less straightforward than in the case of Doumenc *et al.* (2010) because in the current study, the momentum equation lacks a temporal derivative. For those cases, the Neumann boundary conditions for \hat{c} and c^* at the lower wall are replaced with the following Dirichlet condition,

$$\hat{c}\Big|_{z=1} = c^*\Big|_{z=1} = 0. \quad (2.19)$$

Consequently, when maximizing Φ_w , coupling conditions (2.16)–(2.17) are satisfied for,

$$-2k^2\hat{w}\Big|_{t=t_f} = \mathcal{D}c^*\Big|_{t=t_f}, \quad -2k^2s\hat{w}\Big|_{t=t_p} = \mathcal{D}c^*\Big|_{t=t_p}. \quad (2.20)$$

When maximizing Φ_e , conditions (2.16)–(2.17) are satisfied for,

$$\left(k^2 \frac{\partial^2}{\partial z^2} - k^4 - \mathcal{D}^2\right) \hat{w}\Big|_{t=t_f} = \frac{k^2}{2} \mathcal{D}c^*\Big|_{t=t_f}, \quad (2.21)$$

$$s \left(k^2 \frac{\partial^2}{\partial z^2} - k^4 - \mathcal{D}^2\right) \hat{w}\Big|_{t=t_p} = \frac{k^2}{2} \mathcal{D}c^*\Big|_{t=t_p}. \quad (2.22)$$

For the parameter space (t_p, t_f, Ra, k) considered in the current study, the Dirichlet condition (2.19) is a valid approximation because the optimal perturbations

are concentrated near $z = 0$ and decay to zero outside the boundary layer such that they are not influenced by the lower wall (Rapaka *et al.*, 2008; Slim & Ramakrishnan, 2010). The results are validated by directly optimizing the IVP (2.5)–(2.7), subject to the standard boundary conditions (2.6), using MATLAB routines. The adjoint-based method shows excellent agreement with direct optimization but is an order-of-magnitude faster.

2.4 Results

Previously, Rapaka *et al.* (2008) reported optimal perturbations that maximize Φ_c for a fixed initial perturbation time, t_p . That work is extended in the following manner. First, this study explores how the amplification measure (2.11) affects the optimization results. Second, the role of the initial perturbation time is investigated. Third, this study examines the influence of the final time on the initial optimal profiles. Fourth, in this study, the optimal perturbations are compared with quasi-steady eigenmodes. Finally, in §2.3, the current study assesses the relevance of the optimal perturbations to physical experiments.

2.4.1 Effect of amplification measure

Figure 2.2 presents optimization results for $Ra = 500$ and $t_p = 0.01$ when maximizing Φ_c , Φ_w , and Φ_e . The Rayleigh number is set to a typical value for CO₂ sequestration (Ennis-King & Paterson, 2005). The initial perturbation time is chosen to be one order-of-magnitude smaller than the critical time for instability,

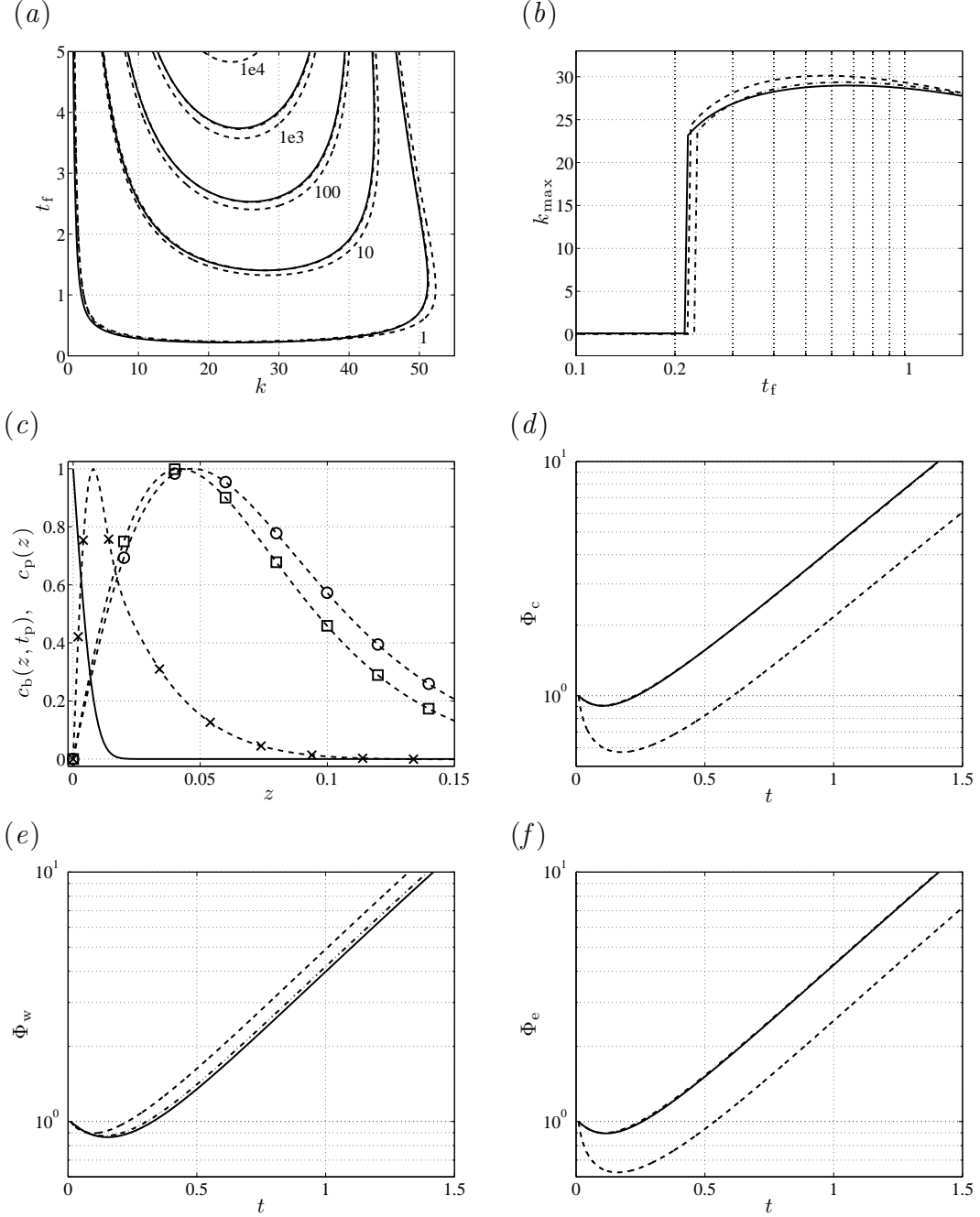


Figure 2.2: Optimization results for $Ra = 500$ and $t_p = 0.01$ when maximizing Φ_c , Φ_w and Φ_e , respectively. (a) Isocontours of Φ_c (solid line), Φ_w (dashed line), and Φ_e (dash-dotted line) in the (k, t_f) plane. (b) k_{\max} , vs. t_f , when maximizing Φ_c (solid line), Φ_w (dashed line), and Φ_e (dash-dotted line). (c) The optimal c_p profiles when maximizing Φ_c (circles), Φ_w (crosses), and Φ_e (squares) for $k = 30$ and $t_f = 5$. The base state $c_b(z, t_p)$ is shown as a solid line. (d)–(f) Amplifications Φ_c , Φ_w , and Φ_e vs. t when integrating the forward IVP (2.5)–(2.7) in time using the optimal initial c_p profiles shown in panel (c), that maximize Φ_c (solid line), Φ_w (dashed line), and Φ_e (dash-dotted line).

t_c , where the critical time is the time at which $d\Phi/dt = 0$, after which Φ begins to increase. The critical time depends on the initial condition and choice of the amplification measure; however, previous analyses find the minimum critical time is on the order of $t_c \sim O(0.1)$ for $Ra = 500$ (Riaz *et al.*, 2006; Selim & Rees, 2007a; Slim & Ramakrishnan, 2010). Panel (a) illustrates optimal isocontours of Φ_c (solid lines), Φ_w (dashed lines), and Φ_e (dash-dotted lines) in the (k, t_f) plane. The three amplification measures produce qualitatively similar behavior. The isocontours for Φ_c and Φ_e are visually indistinguishable. For much of the (k, t_f) plane, Φ_w is marginally larger than Φ_c or Φ_e .

The dominant wavenumber, k_{\max} , is defined as the wavenumber for which the amplification is maximized at t_f ,

$$\Phi_{\max}(t_f) = \sup_{0 \leq k < \infty} \Phi(t_f, k). \quad (2.23)$$

Figure 2.2(b) illustrates the dominant wavenumbers that maximize Φ_c (solid line), Φ_w (dashed line), and Φ_e (dash-dotted line) for the final times $0.1 \leq t_f \leq 2$. The dominant wavenumbers for the three amplification measures are qualitatively similar. When $t_f \leq 0.21$, the dominant wavenumbers are zero. When $t_f > 0.21$, the dominant wavenumbers jump discontinuously to values around $k_{\max} \approx 25$. The dominant zero-wavenumber perturbations were not reported by Rapaka *et al.* (2008) because they considered late values of t_f for which k_{\max} is non-zero. When comparing results of Rapaka *et al.* (2008) with the current study, one must note that Rapaka *et al.* (2008) nondimensionalized the problem with a diffusive time scale, while the current study uses an advective time scale. Consequently, the nondimensional times,

t , in this study are related to those of Rapaka *et al.* (2008), $t^{(R)}$, through the relation $t^{(R)} = t/Ra$.

Though maximizing different perturbation fields produces similar dominant wavenumbers, k_{\max} , the corresponding optimal initial profiles, c_p and w_p , are sensitive to the amplification measure. Figure 2.2(c) illustrates the optimal c_p profiles that maximize Φ_c (circles), Φ_w (crosses), and Φ_e (squares) at $t_f = 5$ for $k = 30$. For visualization, the profiles have been scaled so $\|c_p\|_{\infty} = 1$. The solid line shows the base-state at $t_p = 0.01$. Figure 2.2(c) shows results for $0 \leq z \leq 0.15$ because the profiles are concentrated near $z = 0$ and decay to zero before interacting with the lower wall $z = 1$. The profiles for Φ_e and Φ_c have maxima occurring around $z = 0.05$, while the profile for Φ_w has a maximum occurring around $z = 0.01$.

Figure 2.2(d) illustrates the temporal evolution of Φ_c when the forward IVP (2.5)–(2.7) is integrated from $t_p = 0.01$ to $t = 2$ using the three initial c_p profiles illustrated in figure 2.2(c). The c_p profiles that maximize Φ_c (solid line) and Φ_e (dash-dotted line) produce indistinguishable results in figure 2.2(d). The c_p profile that maximizes Φ_w (dashed line), however, produces much lower values of Φ_c . This suggests that maximization of Φ_w occurs at the expense of Φ_c . Figure 2.2(e) illustrates the corresponding results for the evolution of Φ_w . The c_p profiles that maximize Φ_c (solid line) and Φ_e (dash-dotted line) produce nearly indistinguishable results, while the profile that maximizes Φ_w (dashed line) produces marginally larger Φ_w . Finally, figure 2.2(f) illustrates the corresponding results for the evolution of Φ_e . The initial profiles that maximize Φ_c and Φ_e again produce indistinguishable results. This indicates that maximizing the perturbation’s concentration field nat-

urally maximizes Φ_e , while maximizing Φ_w does so at the expense of Φ_c and Φ_e . Because Φ_c naturally maximizes Φ_e , hereinafter this study focusses on maximizing Φ_c . Φ_c is preferred over Φ_e because the application of the coupling conditions (2.16)–(2.17) is much simpler for Φ_c .

2.4.2 Optimal perturbation structures

Figure 2.3(a) illustrates the optimal amplifications Φ_c versus t_f for $t_p = 0.01$, and $k = 0$ (circles), $k = 10$ (crosses), $k = 25$ (squares), and $k = 40$ (diamonds). For small final times, $t_f < 0.1$, all perturbations decay; however, the $k = 25$ perturbations are more damped than the $k = 0$ and $k = 10$ perturbations. Note that the $k = 0$ perturbations have a small constant damping rate. This occurs because the IVP (2.5)–(2.7) for $k = 0$ reduces to

$$\frac{\partial \hat{c}}{\partial t} - \frac{1}{Ra} \frac{\partial^2 \hat{c}}{\partial z^2} = 0, \quad \hat{w} = 0. \quad (2.24)$$

Equation (2.24) can be solved analytically to show that the optimal perturbation is given by $\hat{c} = \sin(\pi z/2) \exp(-\pi^2 Ra^{-1}t/4)$. In contrast to the $k = 0$ perturbations, finite wavenumber perturbations do not have constant growth rates. The $k = 25$ perturbations begin to grow around $t_f = 0.1$ and eventually overtake the $k = 10$ and $k = 0$ perturbations. This explains the discontinuous jump in the dominant wavenumbers from $k_{\max} = 0$ to $k_{\max} \approx 25$ illustrated in figure 2.2(b). The $k = 40$ perturbations experience greater damping, and consequently, never overtake the $k = 25$ perturbations.

Figure 2.3(b) illustrates the base state, $c_b(z, t_f)$ (solid line), and optimal pro-

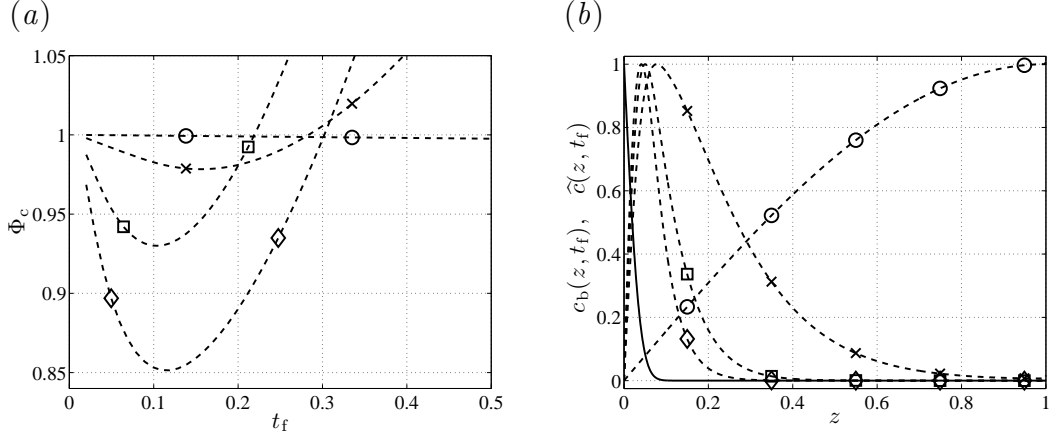


Figure 2.3: Dominant perturbations for $Ra = 500$ and $t_p = 0.01$. (a) Φ_c vs. t_f , for $k = 0$ (circles), $k = 10$ (crosses), $k = 25$ (squares), and $k = 40$ (diamonds). (b) $c_b(z, t_f)$ (solid line) and $\hat{c}(z, t_f)$ for $t_f = 0.21$, and $k = 0$ (circles), $k = 10$ (crosses), $k = 20$ (squares), and $k = 30$ (diamonds).

files, $\hat{c}(z, t_f)$, at $t_f = 0.21$ for $k = 0$ (circles), $k = 10$ (crosses), $k = 20$ (squares), and $k = 30$ (diamonds). The final time is chosen to be near to the discontinuous jump in k_{\max} illustrated in figure 2.2(b). The optimal profile for $k = 0$ has a maximum at the lower boundary at $z = 1$, while the profiles for $k = 10, 20$, and 30 have maxima near $z = 0$. With increasing k , the optimal profiles become increasingly concentrated within the boundary layer.

The results for Φ_c and c_p illustrated in figure 2.3 can be explained physically by examining the competing effects of the stabilizing diffusive term, $\mathcal{D}\hat{c}/Ra$, and the destabilizing convective term, $\hat{w}\partial c_b/\partial z$, in equation (2.5). At small times, $t \ll t_c$, the convective term $\hat{w}\partial c_b/\partial z$ has only a small effect because $\partial c_b/\partial z$ is nonzero only within the thin boundary layer where \hat{w} necessarily tends to zero due to the no-penetration condition at $z = 0$. This explains why the boundary layer is stable at small times. The dominant wavenumber is initially zero because finite wavenumber

perturbations have additional damping due to the transverse diffusive term $(k^2/Ra)\hat{c}$ in equation (2.5). At later times, the growing boundary layer increases the influence of the destabilizing term $\hat{w}\partial c_b/\partial z$ such that non-zero wavenumber perturbations become unstable. This explains why dominant perturbations at late times tend to be increasingly concentrated in the boundary layer.

2.4.3 Sensitivity to initial perturbation time

Due to the transient nature of the base-state, the optimal perturbations also depend on the time, t_p , at which the boundary layer is perturbed. Figure 2.4 explores the sensitivity of the optimal amplifications Φ_c to the initial perturbation time t_p for $Ra=500$. Panel (a) illustrates Φ_c versus t_f for $k = 30$ and $t_p = 0.001$ (solid line), $t_p = 0.1$ (dashed line), and $t_p = 0.5$ (dash-dotted line). Perturbations originating at $t_p = 0.001$ have a long initial damping period and consequently have smaller amplifications than perturbations originating at $t_p = 0.1$. Perturbations originating at the late time $t_p = 0.5$ experience no damping, but have smaller amplifications than perturbations originating at $t_p = 0.001$ and $t_p = 0.1$ because those perturbations begin growing much earlier. At later times, $t_f > 0.5$, the three curves have identical slopes, indicating that the perturbations have identical temporal growth rates. Figure 2.4(b) illustrates isocontours of Φ_c in the (k, t_f) parameter plane for $t_p = 0.001$ (solid line), $t_p = 0.1$ (dashed line), and $t_p = 0.5$ (dash-dotted line). As expected, perturbations originating at $t_p = 0.1$ produce larger amplifications. The horizontal dash-dotted line indicates that perturbations originating at $t_p = 0.5$ grow

immediately for $2 < k < 56$.

Figures 2.4(a) and 2.4(b) suggest that there exists an optimal initial perturbation time, t_p^o , that maximizes Φ_c . Perturbations originating prior to t_p^o cannot outgrow the optimal perturbation originating at t_p^o due to the initial damping period. From figure 2.4(a), t_p^o is expected to occur near the critical time, $t = t_c$, because this minimizes the damping period. Note that for $Ra = 500$, Slim & Ramakrishnan (2010) report that the minimum critical time is $t_c \approx 0.096$. The notion of an optimal initial perturbation time may appear counterintuitive because in physical systems the boundary layer is continuously perturbed beginning at $t_p = 0$. Within the framework of a linear stability analysis, however, the response to this continuous forcing can be expressed as the infinite sum of many impulse responses to forcing at discrete initial times, t_p . The optimal perturbation originating at t_p^o gives a theoretical upper bound for the amplification.

Figure 2.4(c) illustrates the normalized amplifications, $\Phi_c/||\Phi_c||_\infty$, versus t_p for $t_f = 1$, and $k = 10$ (solid line), $k = 30$ (dashed line), and $k = 50$ (dash-dotted line). The amplifications have been normalized with respect to their maximum values to facilitate comparison between the results for different wavenumbers. As $t_p \rightarrow 0$, the amplifications asymptote to constant values. With increasing t_p , the amplifications attain maxima near $t_p = t_c$ and then decrease. Stronger sensitivity of Φ_c to t_p occurs with increasing wavenumber. This behavior is similar to that observed in figure 2.3(a) for the sensitivity of Φ_c to the final time t_f . The increasing sensitivity of Φ_c to both t_p and t_f at higher wavenumbers is likely due to the increase in transverse diffusive damping as noted in the previous section. Figure 2.4(d)

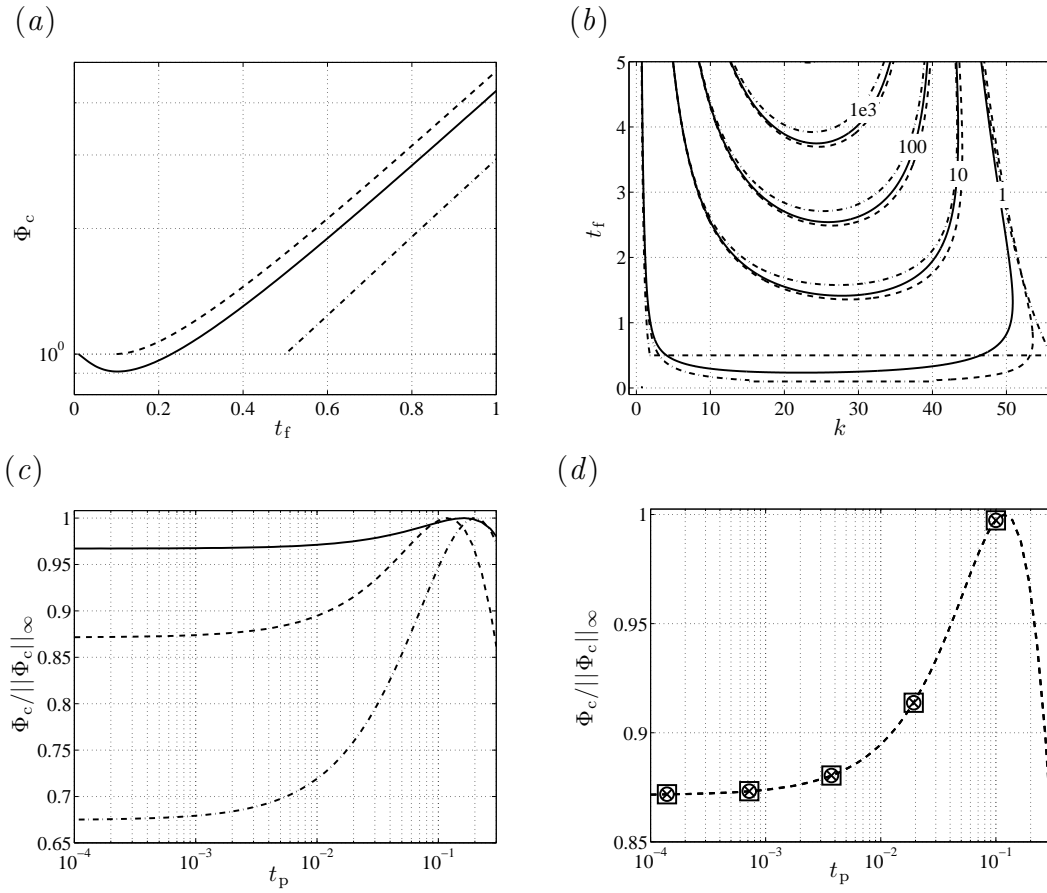


Figure 2.4: Effect of initial perturbation time for $Ra = 500$. (a) Φ_c vs. t_f for $k = 30$, and $t_p = 0.001$ (solid line), $t_p = 0.1$ (dashed line), and $t_p = 0.5$ (dash-dotted line). (b) Isocontours of Φ_c in the (k, t_f) plane for $t_p = 0.001$ (solid line), $t_p = 0.1$ (dashed line), and $t_p = 0.5$ (dash-dotted line). (c) $\Phi_c / \|\Phi_c\|_\infty$, vs. t_p for $t_f = 1$, and $k = 10$ (solid line), $k = 30$ (dashed line), $k = 50$ (dash-dotted line). (d) $\Phi_c / \|\Phi_c\|_\infty$ vs. t_p for $k = 30$ and $t_f = 1$ (circles), $t_f = 2$ (crosses), and $t_f = 3$ (squares).

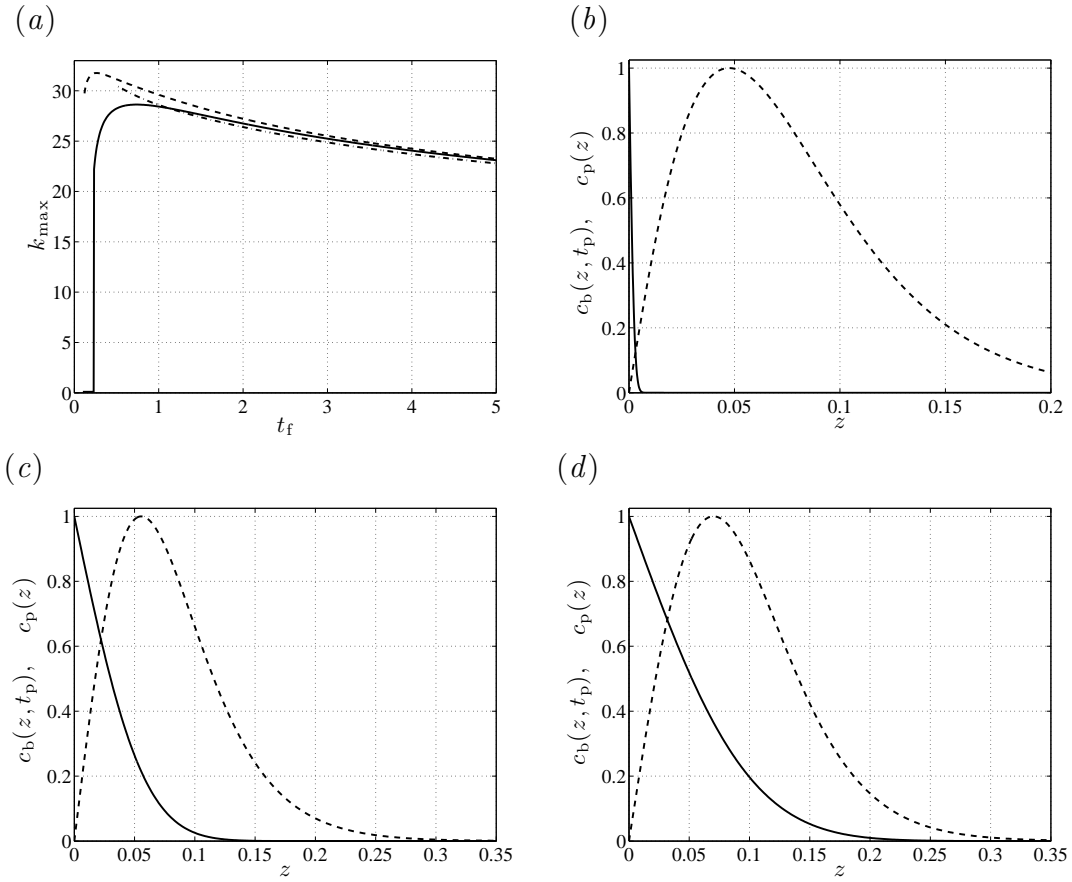


Figure 2.5: (a) Dominant wavenumbers, k_{\max} vs. t_f for $t_p = 0.001$ (solid line), $t_p = 0.1$ (dashed line), and $t_p = 0.5$ (dash-dotted line). (b) Base-state, c_b (solid line), and optimal c_p profiles (dashed line) for $t_p = 0.001$, $t_f = 5$, and $k = 30$. (c) Same as panel (b) for $t_p = 0.5$. (d) Same as panel (b) for $t_p = 1.5$. With increasing t_p , the c_p profiles become increasingly concentrated in the boundary layer.

illustrates $\Phi_c/||\Phi_c||_\infty$ versus t_p for $k = 30$ and $t_f = 1$ (circles), $t_f = 2$ (crosses), and $t_f = 3$ (squares). The results for different t_f are indistinguishable from each other. This occurs because, as demonstrated in figure 2.4(a), the perturbations have identical growth rates for $t_f > 1$.

Figure 2.5(a) illustrates the temporal evolution of the dominant wavenumbers, k_{\max} , when $t_p = 0.001$, (solid line), $t_p = 0.1$ (dashed line), and $t_p = 0.5$ (dash-dotted line). As expected from the discussion in §2.4.2, the dominant wavenumbers are initially zero when $t_p = 0.001$. When $t_p = 0.1$, however, the dominant wavenumber is initially $k_{\max} = 29.74$ for $t_f = 0.12$ and reaches a maximum at $t_f = 0.26$ after which it decays monotonically. When $t_p = 0.5$, k_{\max} decreases monotonically with t_f . Previously, Rapaka *et al.* (2008) only reported cases with a monotonic decay of k_{\max} with t_f . Figures 2.5(b)–2.5(d) illustrate the base state (solid lines) and optimal c_p profiles (dashed lines), for $t_p = 0.001$ (panel b), $t_p = 0.5$ (panel c), and $t_p = 1.5$ (panel d) for $Ra = 500$, $k = 30$, and $t_f = 5$. As expected from the discussion in §2.4.2, the optimal profiles become increasingly concentrated within the boundary layer with increasing t_p due to the destabilizing convective term.

To explore the optimal initial perturbation time, the optimization procedure is repeated for a wide range of wavenumbers, initial times, and final times. Figure 2.6(a) illustrates the optimal amplifications Φ_c for $t_f = 1$, $Ra = 500$, $10 \leq k \leq 50$, and $0.01 \leq t_p \leq 0.5$. The maximum amplification, i.e. the peak of the Φ_c surface in figure 2.6(a), is defined as

$$\Phi_c^\circ(t_f) = \sup_{\substack{0 \leq k < \infty \\ 0 < t_p < t_f}} \{\Phi_c(t_f, k, t_p)\}, \quad (2.25)$$

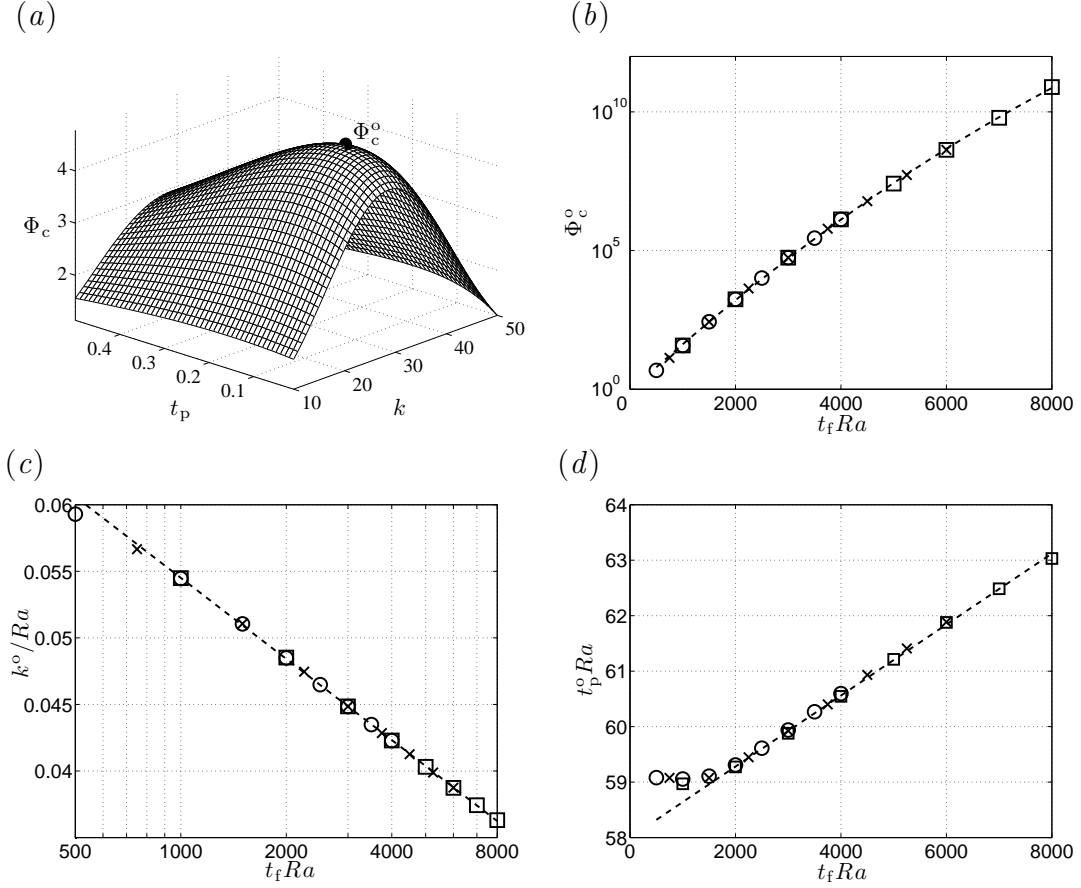


Figure 2.6: The optimal point (Φ_c^o, k^o, t_p^o) as a function of t_f and Ra . (a) Φ_c vs. t_p and k for $Ra = 500$ and $t_f = 1$. The solid dot marks (Φ_c^o, k^o, t_p^o) . (b) Φ_c vs. $t_f Ra$ for $Ra = 500$ (circles), $Ra = 750$ (crosses), and $Ra = 1000$ (squares). The dashed line shows relationship (2.26). (c) k^o/Ra vs. $t_f Ra$ for $Ra = 500$ (circles), $Ra = 750$ (crosses), and $Ra = 1000$ (squares). The dashed line shows relationship (2.27) (d) $t_p^o Ra$ vs. $t_f Ra$ for $Ra = 500$ (circles), $Ra = 750$ (crosses), and $Ra = 1000$ (squares). The dashed line shows relationship (2.28).

and the optimal point (k°, t_p°) as the location in the (k, t_p) plane where $\Phi = \Phi_c^\circ$.

To explore the dependence of the optimal point on t_f and Ra , $(\Phi_c^\circ, k^\circ, t_p^\circ)$ is calculated for $500 \leq Ra \leq 1000$ and $1 \leq t_f \leq 8$. Figure 2.6 demonstrates that the results collapse to three curves by plotting Φ_c° (panel *b*), k°/Ra (panel *c*), and $t_p^\circ Ra$ (panel *d*) as functions of $t_f Ra$. This collapse occurs because the optimal perturbations are concentrated near $z = 0$ and do not interact with the lower boundary at $z = 1$. Consequently, the Rayleigh number dependence may be scaled out of the governing equations (2.1)–(2.2) by approximating the vertical depth as infinite, $H \rightarrow \infty$, and nondimensionalizing the problem with respect to the characteristic length $L = \phi D/U$, and time, $T = \phi L/U$. From figure 2.6, obtain the following relationships,

$$\log \Phi_c^\circ = -4.458 \times 10^{-8} (t_f Ra)^2 + 0.001721 t_f Ra - 0.05739, \quad (2.26)$$

$$k^\circ = Ra [0.1152 - 0.02023 \log(t_f Ra)], \quad (2.27)$$

$$t_p^\circ = 6.364 \times 10^{-4} t_f + 58.00/Ra, \quad (2.28)$$

For convenience, relations (2.27) and (2.28) are presented in dimensional form,

$$k^* = \frac{U}{\phi D} \left[0.1152 - 0.02023 \log \left(\frac{t_f^* U^2}{\phi^2 D} \right) \right], \quad (2.29)$$

$$t_p^* = 6.364 \times 10^{-4} t_f^* + 58.00 \frac{\phi^2 D}{U^2}, \quad (2.30)$$

where k^* , t_p^* , and t_f^* are the optimal wavenumber, initial time, and final time in dimensional form. Recall from §2.2 that $U = K \Delta \rho g / \mu$. These relations demonstrate that the optimal wavenumber and initial time are independent of the aquifer depth

H. Note that when $t_f Ra < 1500$, relations (2.26) and (2.27) continue to provide accurate estimates, while relation (2.28) deviates significantly.

Ennis-King & Paterson (2005) report the following typical parameter values for CO₂ sequestration: $\mu = 5 \times 10^{-4}$ Pa s, $\phi = 0.2$, $\Delta\rho = 10$ kg m⁻³, $g = 9.81$ m s⁻², $D = 10^{-9}$ m² s⁻¹, and $10^{-14} \leq K \leq 10^{-12}$ m². Using these values, figure 2.6 predicts that the optimal wavelength and initial time for high permeability aquifers, $K = 10^{-12}$ m², vary in the range, $11 \text{ cm} \leq 2\pi/k^* \leq 18 \text{ cm}$ and $17 \text{ hours} \leq t_p^* \leq 18 \text{ hours}$ as the final time varies between, $6 \text{ days} \leq t_f^* \leq 96 \text{ days}$. For low permeability aquifers, $K = 10^{-14}$ m², these parameters vary between $11 \text{ m} \leq 2\pi/k^* \leq 18 \text{ m}$, $19 \text{ years} \leq t_p^* \leq 21 \text{ years}$, $165 \text{ years} \leq t_f^* \leq 2636 \text{ years}$. While these initial and final times for $K = 10^{-14}$ m² aquifers may appear late, the optimal initial times are consistent with previous estimates of the critical time reported by Ennis-King & Paterson (2005) and Riaz *et al.* (2006). Furthermore, in §2.6.2, the range of final times are found to be representative of actual onset times for nonlinear convection, t_o .

The dependence of the optimal point (k^o, t_p^o) on t_f indicates that the optimal initial perturbation depends on the initial perturbation amplitude and consequently cannot be determined through purely linear analysis. Consider, for example, that direct numerical simulations show that the onset time for convection, t_o , decreases with increasing initial perturbation amplitude (Rapaka *et al.*, 2008; Selim & Rees, 2007*b*). Consequently, figures 2.6(*c*) and 2.6(*d*) predict that large amplitude perturbations will have larger values of k^o and smaller values of t_p^o than small amplitude perturbations. Their exact values, however, would require *a priori* numerical or

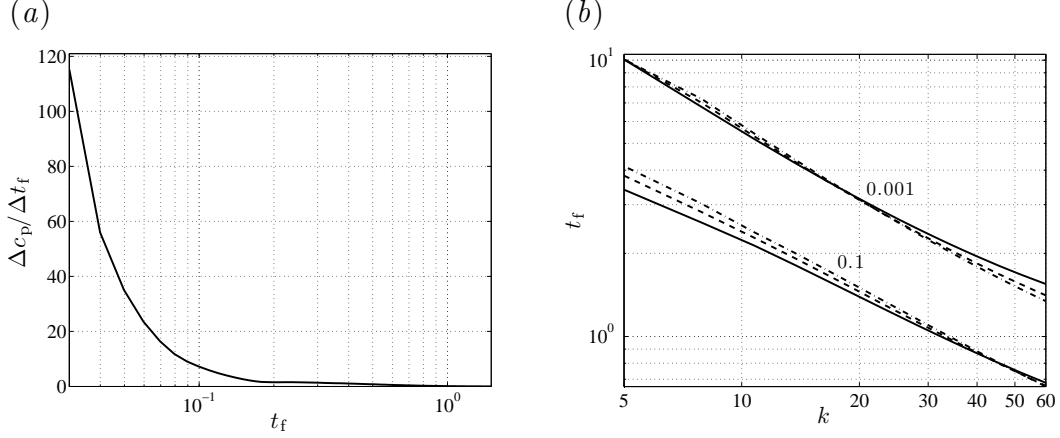


Figure 2.7: Convergence of the optimal c_p profiles for $t_p = 0.01$. (a) $\Delta c_p/\Delta t_f$ vs. t_f for $k = 30$ and $Ra = 500$ (b) Isocontours of $\Delta c_p/\Delta t_f$ in the (k, t_f) plane for $Ra = 500$ (solid line), $Ra = 750$ (dashed line), and $Ra = 1000$ (dash-dotted line).

experimental results for the onset time t_o .

2.4.4 Influence of final time on initial perturbation profiles

Beyond a certain final time, the initial profiles, c_p and w_p , are unaffected by further increases to t_f . To quantify the final time beyond which c_p and w_p do not depend on t_f , the rate of change of c_p is measured with respect to t_f as,

$$\frac{\Delta c_p}{\Delta t_f} = \frac{\|c_p(z; t_f + \Delta t_f) - c_p(z; t_f)\|_\infty}{\Delta t_f}, \quad (2.31)$$

where $\Delta t_f = 0.01$ and the c_p profiles are normalized with respect to their L^2 norms. Figure 2.7(a) illustrates $\Delta c_p/\Delta t_f$ versus t_f for $t_p = 0.01$, $k = 30$ and $Ra = 500$. $\Delta c_p/\Delta t_f$ is initially large but decreases rapidly to zero. Figure 2.7(b) illustrates isocontours of $\Delta c_p/\Delta t_f = 0.1$ and 0.001 in the (k, t_f) parameter plane for $t_p = 0.01$ and $Ra = 500$ (solid line), $Ra = 750$ (dashed line), and $Ra = 1000$ (dash-

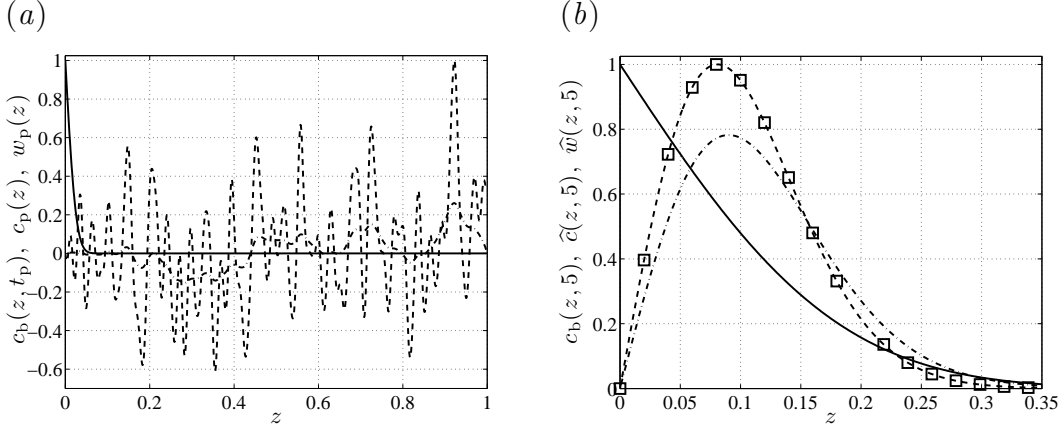


Figure 2.8: IVP results using random initial profiles, c_p and w_p , for $t_p = 0.01$, $k = 30$, and $Ra = 500$. (a) The base-state (solid line) and random initial profiles c_p (dashed line) and w_p (dash-dotted line) at $t_p = 0.01$. (b) Resulting perturbation profiles \hat{c} (dashed line) and \hat{w} (dash-dotted line) at $t = 5$. The squares show the corresponding optimal perturbation \hat{c} when $t_f = 5$.

dotted line). With increasing k , the final time after which c_p and w_p do not change decreases. There is only a small influence of the Rayleigh number on the $\Delta c_p / \Delta t_f$ isocontours.

The convergence of c_p and w_p beyond a certain t_f may be explained by noting that the forward IVP (2.5)–(2.7) always converges to the same dominant perturbations given sufficient time. To demonstrate this behavior, figure 2.8(a) illustrates random initial conditions for c_p (dashed line) and w_p (dash-dotted line) that span the entire vertical domain, $0 \leq z \leq 1$, at $t_p = 0.01$ for $k = 30$. Figure 2.8(b) illustrates the resulting perturbation profiles, $\hat{c}(z, 5)$ and $\hat{w}(z, 5)$, generated by integrating the forward IVP to $t = 5$. The final state of the forward IVP is identical to the corresponding optimal perturbation, shown using squares in figure 2.8(b).

2.4.5 Comparison with quasi-steady eigenvalue analysis

The convergence of the forward IVP and optimization procedure to identical dominant perturbations at late times may be explained by considering a quasi-steady modal analysis. The optimal perturbations are compared with the dominant QSSA modes by measuring,

$$\Delta\hat{c} = \int_0^1 \left| \frac{c_e(z; t_f)}{\|c_e(z; t_f)\|_\infty} - \frac{\hat{c}(z, t_f)}{\|\hat{c}(z, t_f)\|_\infty} \right| dz. \quad (2.32)$$

When $\Delta\hat{c} = 0$, the dominant QSSA mode and optimal perturbation are identical.

Figure 2.9 compares optimal perturbations with dominant QSSA modes for $t_p = 0.1$ and $Ra = 500$. Note that t_p is chosen to be close to the optimal initial time t_p^o . Figure 2.9(a) illustrates the variation of $\Delta\hat{c}$ for wavenumbers $5 \leq k \leq 60$ and final times $0.12 \leq t_f \leq 2$. Large values of $\Delta\hat{c}$ occur at small wavenumbers and final times. In the limit of $k \rightarrow 0$, however, $\Delta\hat{c}$ tends to zero because the optimal perturbation and dominant QSSA mode both tend to $\hat{c} = \sin(\pi z/2) \exp(-\pi^2 Ra^{-1}t/4)$. With increasing wavenumber and final time, $\Delta\hat{c}$ becomes small, indicating that the optimal perturbations essentially recover the dominant QSSA modes. This behavior is confirmed in figure 2.9(b) which illustrates the base-state (solid line), optimal perturbation (dashed line), and dominant QSSA eigenmode (dash-dotted line) at $t_f = 2$ and $k = 10$. Note that $\Delta\hat{c}$ remains small for the optimal perturbations with wavenumber, k_{\max} , illustrated in figure 2.2(b).

The amplification produced by temporal integration of the dominant QSSA

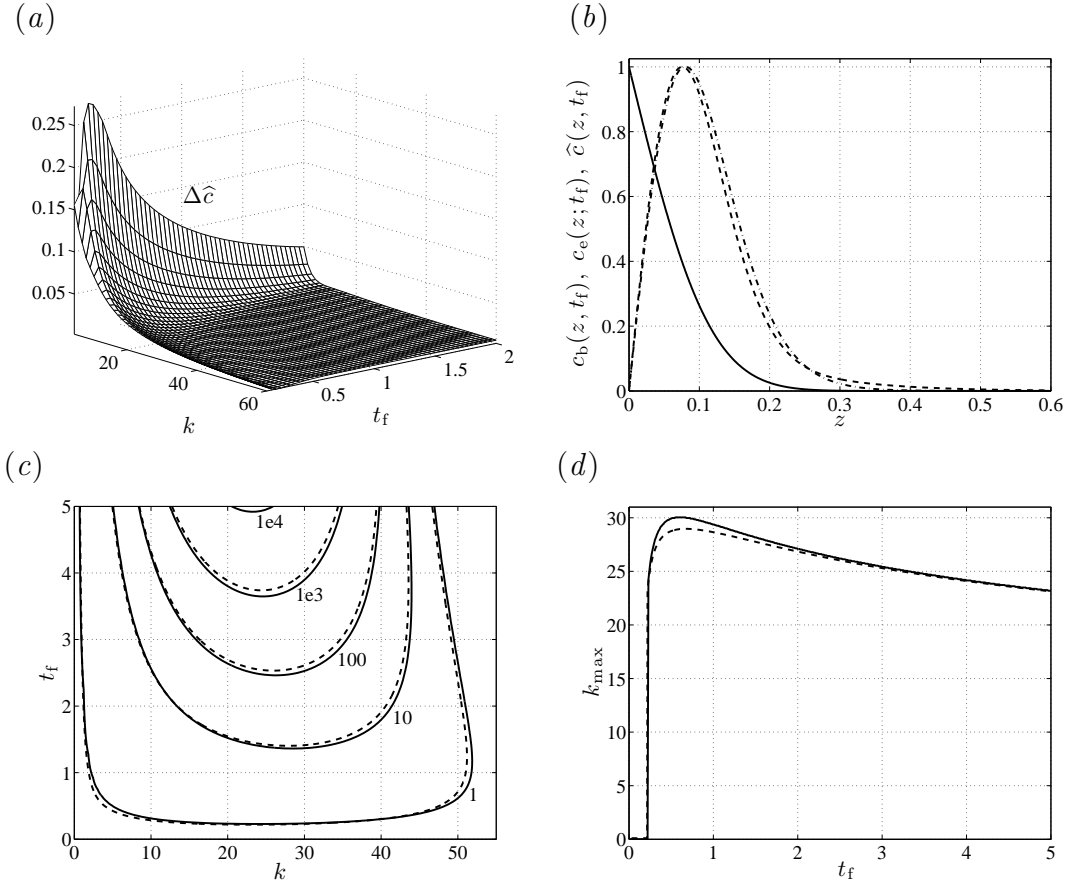


Figure 2.9: Comparison of optimal perturbations with the least stable QSSA mode for $Ra = 500$. (a) $\Delta \hat{c}$ in the (k, t_f) plane for $t_p = 0.1$. (b) illustrates base-state, $c_b(z, t_f)$ (solid line), optimal perturbation $\hat{c}(z, t_f)$ (dashed line) and least stable eigenmode, $c_e(z, t_f)$ (dash-dotted line) at t_f for $t_p = 0.1$, $k = 10$, and $t_f = 2$. (c) Isocontours of amplification in the (k, t_f) plane when $t_p = 0.01$ for QSSA (solid lines) and optimization (dashed lines). (d) The dominant wavenumbers k_{\max} vs. t_f when $t_p = 0.01$ for QSSA (solid lines) and optimization (dashed lines)

growth rate, σ , can be computed through the relation

$$\Phi_q(t) = e^{g(t)}, \quad g(t) = \int_{t_p}^t \sigma(t_f) dt_f. \quad (2.33)$$

Figure 2.9(c) compares isocontours of Φ_q (solid line) with optimal results for Φ_c (dashed line) in the (k, t_f) parameter plane for $Ra = 500$ and $t_p = 0.01$. The amplifications produced by optimal perturbations are in excellent agreement with the dominant QSSA eigenmodes. Counterintuitively, for much of the (k, t_f) plane, Φ_q is marginally greater than Φ_c . This occurs for the following reasons. At late times, the boundary layer grows slowly and the optimal perturbations tend to the dominant QSSA eigenmodes. At small times, however, the boundary layer varies rapidly and the optimal perturbations cannot continuously adhere to the quasi-steady eigenmodes. Consequently, temporal integration of the dominant QSSA growth rates produces marginally larger amplifications than Φ_c . This also helps explain why dominant perturbations tend to differ from the dominant eigenmode at small times.

Figure 2.9(d) illustrates the dominant wavenumbers, k_{\max} , that maximize Φ_q (solid line) and Φ_c (dashed line) for $0.03 \leq t_f \leq 5$. The optimization procedure is repeated for different t_p and observe similar agreement between the QSSA and optimization results. This suggests that optimal perturbations are primarily composed of the dominant QSSA mode. In contrast, nonmodal stability analyses of steady wall-bounded shear flows, such as channel flows and flat plate boundary layers, typically produce optimal perturbations that are qualitatively very different from the corresponding dominant eigenmodes. This suggests that for the current study, the deviation of the optimal perturbations from the dominant eigenmodes at small times

| $t_p = 0.01$ | | $t_p = 0.1$ | | $t_p = 1$ | |
|--------------|-------------------------------|-------------|-------------------------------|------------|-------------------------------|
| A_∞ | $c_{\text{net}}^{\text{min}}$ | A_∞ | $c_{\text{net}}^{\text{min}}$ | A_∞ | $c_{\text{net}}^{\text{min}}$ |
| 10^{-02} | -10^{-02} | 10^{-02} | -8.0×10^{-03} | 10^{-02} | -2.1×10^{-03} |
| 10^{-05} | -10^{-05} | 10^{-05} | -4.9×10^{-06} | 10^{-05} | -3.3×10^{-08} |
| 10^{-10} | -10^{-10} | 10^{-10} | -2.5×10^{-11} | 10^{-10} | -5.1×10^{-15} |

Table 2.1: Minimum net concentrations $c_{\text{net}}^{\text{min}}$ produced by the classical optimal c_p profiles when $k = 30$, $Ra = 500$, $t_f = 5$, $t_p = 0.01, 0.1, 1$, and $A_\infty = 10^{-2}, 10^{-5}$, and 10^{-10} . At $t_p = 0.01$, the negative concentration is of the same order as A_∞ . As t_p increases, the perturbation profiles become increasingly concentrated within the boundary layer and consequently the magnitude of the negative concentrations $c_{\text{net}}^{\text{min}}$ diminish.

is primarily due to the transient base-state, rather than the nonorthogonality of the quasi-steady eigenmodes.

2.5 Modified Optimization Procedure

Experimental studies observe that perturbations are initially localized within the boundary layer (Blair & Quinn, 1969; Elder, 1968; Green & Foster, 1975; Spangenberg & Rowland, 1961; Wooding *et al.*, 1997). To determine whether the optimal perturbations obtained in §4 reflect those observed experimentally, one considers the following argument. If the optimal perturbation is observed experimentally, the net concentration can be expressed as the sum of the base-state and perturbation

through the relation

$$c_{\text{net}}(x, z, t_p) = c_b(z, t_p) + A_\infty \cos(kx) \frac{c_p(z)}{\|c_p\|_\infty}, \quad (2.34)$$

where c_p is the optimal initial profile and A_∞ is the perturbation amplitude measured using the L^∞ norm. Table 2.1 lists the minimum net concentrations, c_{net}^{\min} , for various A_∞ and t_p when $t_f = 5$, $k = 30$, and $Ra = 500$. For $t_p = 0.01$, unphysical negative net concentrations are observed that are equal to A_∞ . This occurs because the maxima of the optimal c_p profiles are located outside the boundary layer, see figure 2.5(b). For $t_p = 0.1$ and 1, the magnitude of the negative concentrations become increasingly smaller because the optimal c_p profiles become increasingly concentrated within the boundary layer, see figures 2.5(c)–2.5(d).

Direct numerical simulations show that the onset time for convection decreases with increasing initial perturbation amplitude A_∞ (Rapaka *et al.*, 2008). Consequently, though the classical optimal perturbations are mathematically valid optimal solutions, onset of convection in physical systems may more likely be triggered by suboptimal perturbations concentrated within boundary layer. Those perturbations support finite initial amplitudes, and consequently require less time to grow sufficiently for onset of convection. To investigate this alternate path to onset of convection, this study proposes a modified optimization procedure that constrains the initial concentration fields of the perturbations to be within the boundary layer.

2.5.1 Methodology

The classical optimization procedure described in §3 is modified by replacing the constraint $E(t_p) = 1$ with the modified constraint $E_\Psi(t_p) = 1$, where

$$E_\Psi(t_p) = \int_0^1 \Psi(z) \widehat{c}(z, t_p)^2 dz, \quad (2.35)$$

where $\Psi(z)$ is a filter function that tends to infinity, $\Psi \rightarrow \infty$, outside the boundary layer. Then $\Phi_\Psi = \sqrt{E(t_f)/E_\Psi(t_p)}$ is maximized. The filter function assures that $E_\Psi(t_p) = \infty$, when c_p extends beyond the boundary layer. This forces Φ_Ψ to zero and effectively filters such perturbations from the optimization procedure. In practice, the infinite values of Ψ are approximated numerically using a large finite value.

Following an analogous procedure to that in §3, the Lagrangian is formulated,

$$\begin{aligned} \mathcal{L}(\widehat{c}, c^*, \widehat{w}, w^*, s) &= E(t_f) - s[E_\Psi(t_p) - 1] - \int_{t_p}^{t_f} \int_0^1 w^* (\mathcal{D}\widehat{w} + k^2\widehat{c}) dz dt \\ &\quad - \int_{t_p}^{t_f} \int_0^1 c^* \left(\frac{\partial \widehat{c}}{\partial t} - \frac{1}{Ra} \mathcal{D}\widehat{c} + \widehat{w} \frac{\partial c_b}{\partial z} \right) dz dt, \end{aligned} \quad (2.36)$$

and obtain the following coupling conditions between physical and adjoint variables,

$$2s\widehat{c}|_{t_p} = \Psi^{-1}c^*|_{t_p}, \quad 2\widehat{c}|_{t_f} = c^*|_{t_f}. \quad (2.37)$$

The adjoint IVP (2.14)–(2.15) remains unchanged. After convergence of the iterative procedure for the optimal profile that maximizes Φ_Ψ , the final amplification is computed using the traditional definition of $\Phi_c = \sqrt{E(t_f)/E(t_p)}$. This allows us to compare results of the modified optimization procedure with those of the classical procedure.

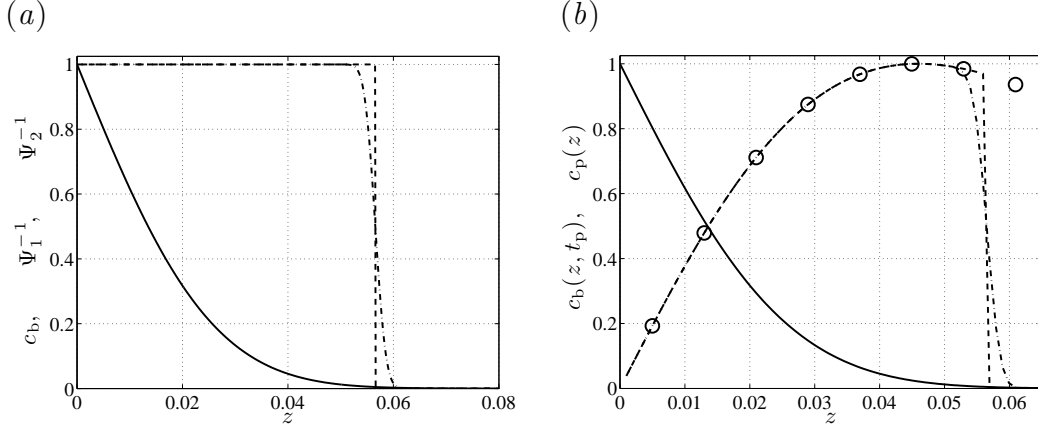


Figure 2.10: Optimization using Ψ_1 and Ψ_2 for $k = 30$, $Ra = 500$, $t_p = 0.1$, and $t_f = 3$. (a) Base-state (solid line), Ψ_1^{-1} (dashed line), and Ψ_2^{-1} (dash-dotted line). (b) Base-state (solid line), classical c_p (circles), and modified c_p profiles using Ψ_1 (dashed line) and Ψ_2 (dash-dotted line).

2.5.2 Filter Functions

First, a filter function is employed such that its inverse is a step function of the form,

$$\Psi_1^{-1}(z) = \begin{cases} 1 & \text{if } z \leq \delta, \\ 0 & \text{if } \delta < z \leq 1, \end{cases} \quad (2.38)$$

where δ is the boundary layer depth defined as $c_b(\delta, t_p) = 0.005$. Figure 2.10(a) illustrates Ψ_1^{-1} as a dashed line for $t_p = 0.1$ and $Ra = 500$. The base-state is shown as a solid line. Figure 2.10(b) illustrates the corresponding optimal c_p profile (dashed line) for $Ra = 500$, $k = 30$, $t_p = 0.1$, and $t_f = 3$. The base-state is shown as a solid line and the classical optimal c_p profile is shown using circles. Within the boundary layer, the modified profile follows the classical profile and then vanishes

discontinuously at $z = \delta$. Consequently, though concentrated within the boundary layer, the perturbations generated by Ψ_1 are unlikely to arise in nature.

To produce continuously differentiable perturbations, the following filter function is introduced such that it is equal to unity in most of the boundary layer, but varies smoothly to zero beyond the boundary layer depth,

$$\Psi_2^{-1}(z) = \frac{1}{2} \left[1 - \operatorname{erf} \left(\frac{25(z - \delta)}{\delta} \right) \right]. \quad (2.39)$$

Figure 2.10(a) illustrates Ψ_2^{-1} using a dash-dotted line. Figure 2.10(b) illustrates that the corresponding optimal modified c_p profile (dash-dotted line) decreases rapidly, but smoothly, to zero outside the boundary layer, but is otherwise similar to that produced by Ψ_1 . The modified profiles illustrated in figure 2.10(b) produce physical initial conditions, $c_{\text{net}}^{\min} = 0$, when $A_\infty < 10^{-3}$.

Though Ψ_2 produces physically realizable optimal perturbations, the perturbations have maxima near the boundary layer depth, $z = \delta$, where the base-state concentration is very small. This limits the maximum allowable initial amplitude of these perturbations. In contrast, perturbations with maxima near $z = 0$ can support larger initial amplitudes and may consequently trigger onset of convection sooner. Furthermore, one may expect that perturbations would naturally tend to have maxima near the upper boundary, $z = 0$, where the base-state has a maximum and there is consequently more solute to perturb. To investigate this possibility, note that the inverse filter functions may be first interpreted as weight functions. Because Ψ_1^{-1} and Ψ_2^{-1} are equal to unity in most of the boundary layer, they give equal weight to most of the boundary layer. Optimal perturbations with maxima

near $z = 0$ can be obtained using an inverse filter function that decreases with the base-state concentration. A natural candidate is $\Psi_3^{-1} = c_b$ because this naturally weighs regions of high base-state concentration over those with low base-state concentration.

Figure 2.11(a) illustrates the base-state (solid line) and c_p profile generated using Ψ_3 (dashed line) for $t_p = 0.1$, $t_f = 5$, $k = 30$, and $Ra = 500$. As expected, Ψ_3 produces a profile with a maximum closer to $z = 0$ than $z = \delta$. Consequently, the profile shown in figure 2.11(a) supports initial amplitudes as large as $A_\infty = 10^{-1}$ without producing negative values of c_{net} . Figure 2.11(b) illustrates optimal isocontours of Φ_c in the (k, t_f) parameter plane using Ψ_2 (solid lines) and Ψ_3 (dashed lines). As expected, though Ψ_3 supports larger initial amplitudes, Ψ_2 produces greater amplifications. This raises the possibility that there exists an optimal filter function, Ψ_{opt} , that balances the tradeoff between the initial amplitude and subsequent amplification in order to minimize the onset time for convection. This is beyond the scope of the current study, however, because it requires a nonlinear analysis. Therefore, for brevity, this study focusses on the perturbations produced by Ψ_3 because these support large initial amplitudes.

2.5.3 Comparison with classical optimization scheme

Hereinafter, this study refers to the classical optimization procedure as COP and the modified optimization procedure using Ψ_3 as MOP. Figure 2.12(a) illustrates the temporal evolution of the dominant wavenumbers, k_{max} , produced by

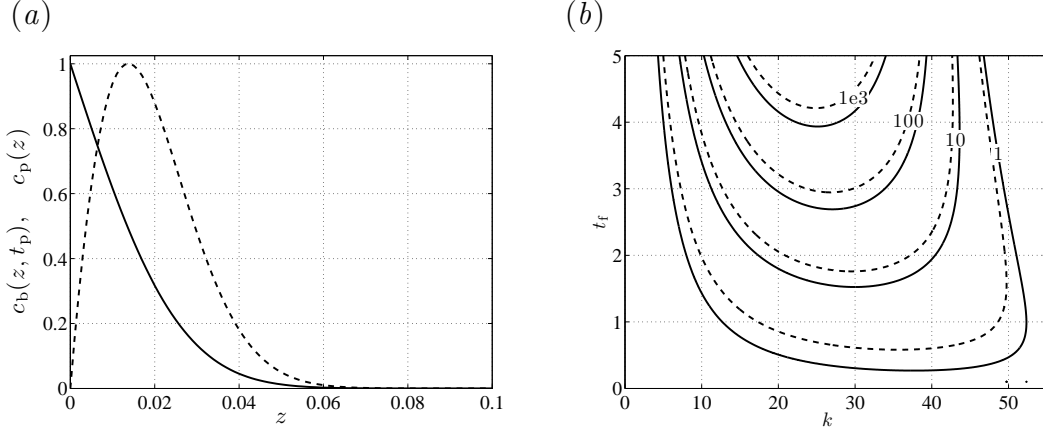


Figure 2.11: Optimization results for $t_p = 0.01$ and $Ra = 500$. (a) The base-state $c_b(z, t_p)$ (solid line) and optimal $c_p(z)$ profile using Ψ_3 (dashed line) for $t_f = 5$ and $k = 30$. Note that the initial $c_p(z)$ profile obtained using Ψ_2 is shown in figure 2.10(b). (b) Isocontours of Φ_c in (k, t_f) plane using Ψ_2 (solid line) and Ψ_3 (dashed line).

the COP (solid line) and MOP (dashed line) schemes for $t_p = 0.01$ and $Ra = 500$. For early final times, $t_f < 0.21$, the MOP scheme produces nonzero dominant wavenumbers, $k_{\max} \neq 0$, while the COP scheme predicts $k_{\max} = 0$. The large difference in dominant wavenumbers at small times occurs because the zero-wavenumber perturbations produced by the COP scheme span the entire vertical domain, $\hat{c} = \sin(\pi z/2) \exp(-\pi^2 Ra^{-1} t/4)$, as discussed in §2.4.2. Using the MOP scheme, these perturbations are filtered by Ψ_3 . At late t_f , the MOP dominant wavenumbers tend towards those predicted by the COP. Figure 2.12(b) illustrates the corresponding maximum amplifications, Φ_{\max} , see equation (2.23), produced by the COP (solid line) and MOP (dashed line) schemes. For final times, $t_f < 0.21$, the COP amplifications are close to unity because the zero-wavenumber perturbations have a small constant decay rate, see discussion in §2.4.2. The MOP amplifica-

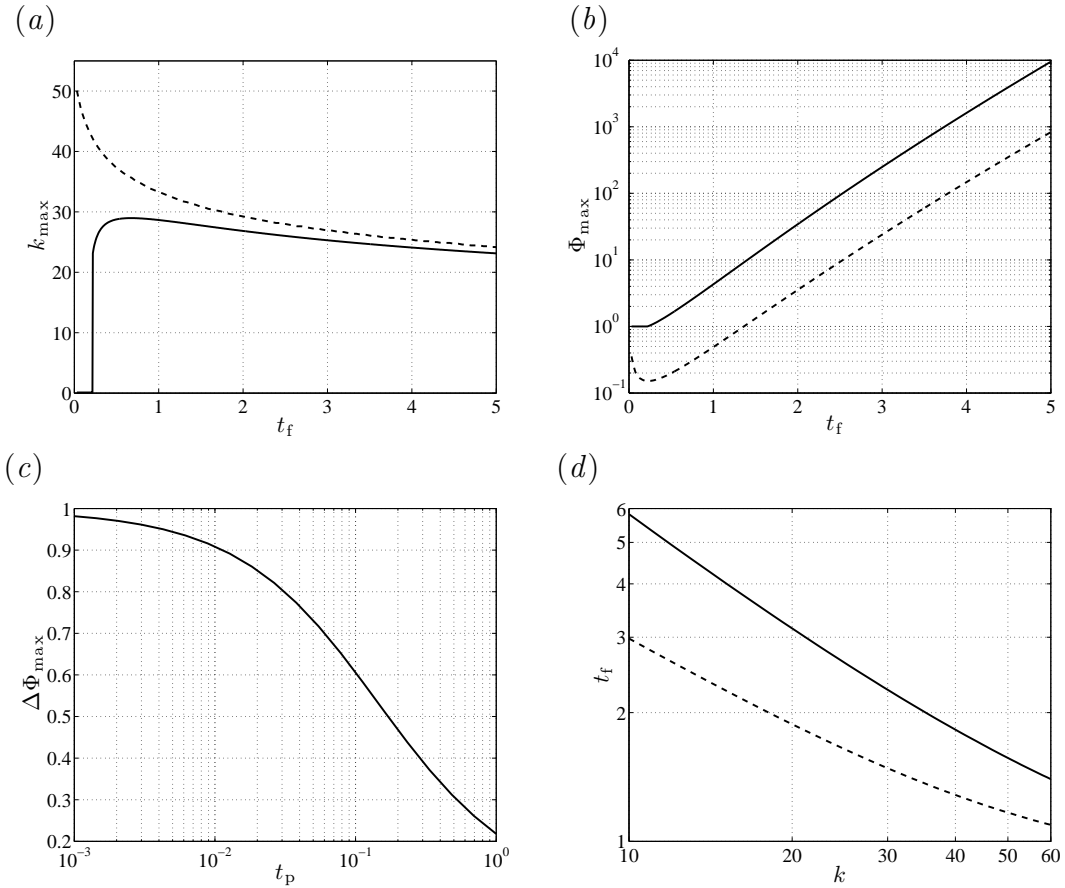


Figure 2.12: Comparison of the COP and MOP schemes for $Ra = 500$. (a) k_{\max} vs. t_f for $t_p = 0.01$ for COP (solid line) and MOP (dashed line). (b) Φ_{\max} vs. t_f for $t_p = 0.01$ for COP (solid line) and MOP (dashed line). (c) $\Delta\Phi_{\max}$ vs. t_p for $t_f = 4$. (d) Isocontours of $\Delta c_p / \Delta t_f = 0.001$ in the (k, t_f) plane for $t_p = 0.1$ for COP (solid line) and MOP (dashed line).

tions are an order-of-magnitude smaller because the perturbations are constrained to the boundary layer and undergo substantial damping up to the critical time for instability, t_c . For $t_f > 1$, the amplifications produced by COP and MOP in figure 2.12(b) have identical slopes. This occurs because of similar growth rates between the final states of the dominant wavenumber perturbations obtained using the COP and MOP schemes.

The difference between the COP and MOP amplifications depends on the initial time, t_p . To explore this, one can measure

$$\Delta\Phi_{\max} = \frac{\Phi_{\text{COP}} - \Phi_{\text{MOP}}}{\Phi_{\text{COP}}}, \quad (2.40)$$

where Φ_{COP} and Φ_{MOP} are the maximum amplifications, Φ_{\max} , obtained using COP and MOP, respectively. Figure 2.12(c) illustrates $\Delta\Phi_{\max}$ for $t_f = 4$ as the initial perturbation time varies from $t_p = 10^{-3}$ to $t_p = 1$. Note that the results are independent of final time t_f when $t_f > 1$. $\Delta\Phi_{\max}$ tends to a maximum as $t_p \rightarrow 0$ because $\Phi_{\text{MOP}} \rightarrow 0$, while Φ_{COP} converges to finite values, see figures 2.4(c)–2.4(d). With increasing t_p , $\Delta\Phi_{\max}$ decreases indicating better agreement between the COP and MOP amplifications. Note that the maxima of the optimal initial MOP profiles are always closer to the top boundary, $z = 0$, compared to the initial COP profiles.

Recall from §2.4.4, that beyond certain final times, the initial c_p profiles generated by the COP scheme are insensitive to further increases in t_f . To investigate this behavior for the MOP scheme, figure 2.12(d) illustrates the isocontours $\Delta c_p / \Delta t_f = 0.001$, see equation (2.31), in the (k, t_f) parameter plane generated using the COP (solid line) and MOP (dashed line) schemes for $t_p = 0.1$ and $Ra = 500$. The

final times beyond which the initial MOP profiles do not change shape are much smaller than the COP profiles. This suggests that initial perturbations confined within the boundary layer rapidly converge to a common shape.

As discussed in §2.4.3, due to the transient growth of the base-state, there exists an optimal combination of initial time and wavenumber, t_p^o and k^o , that produces the subsequent optimal amplification Φ_c^o . Figure 2.13(a) illustrates the MOP amplifications, Φ_c , for $10 \leq k \leq 50$, $0.1 \leq t_p \leq 0.5$, $t_f = 1$, and $Ra = 500$. The solid dot marks the peak of the surface, Φ_c^o . Figure 2.13 demonstrates Φ_c^o (panel b), k^o/Ra (panel c), and $t_p^o Ra$ (panel d) as functions of $t_f Ra$. The results for different Ra collapse as previously demonstrated for the COP scheme in figure 2.6. The following relationships for Φ_c^o and the dimensional forms of wavenumber, k^* , and the initial time, t_p^* are obtained,

$$\log \Phi_c^o = -5.550 \times 10^{-8} t_f^{*2} \left(\frac{U^2}{\phi^2 D} \right)^2 + 0.001785 t_f^* \frac{U^2}{\phi^2 D} - 0.3967, \quad (2.41)$$

$$k^* = \frac{U}{\phi D} \left[0.1234 - 0.02237 \log \left(\frac{t_f^* U^2}{\phi^2 D} \right) \right], \quad (2.42)$$

$$t_p^* = -5.107 \times 10^{-7} t_f^{*2} \frac{U^2}{\phi^2 D} + 0.01086 t_f^* + 120.1 \frac{\phi^2 D}{U^2}. \quad (2.43)$$

For high permeability aquifers, $K = 10^{-12} \text{ m}^2$ (see §2.4.3), figure 2.13 predicts that the optimal perturbation wavelength and initial perturbation time vary in the range, $10 \text{ cm} \leq 2\pi/k^* \leq 18 \text{ cm}$ and $36 \text{ hours} \leq t_p^* \leq 51 \text{ hours}$ as the final time varies between, $6 \text{ days} \leq t_f^* \leq 96 \text{ days}$. For low permeability aquifers, $K = 10^{-14} \text{ m}^2$, these parameters vary in the range $10 \text{ m} \leq 2\pi/k^* \leq 18 \text{ m}$, $41 \text{ years} \leq t_p^* \leq 58 \text{ years}$, $165 \text{ years} \leq t_f^* \leq 2636 \text{ years}$. The optimal amplifications, Φ_c^o , are approximately 50 % those produced by the COP scheme, see figure 2.6. k^o agrees closely with

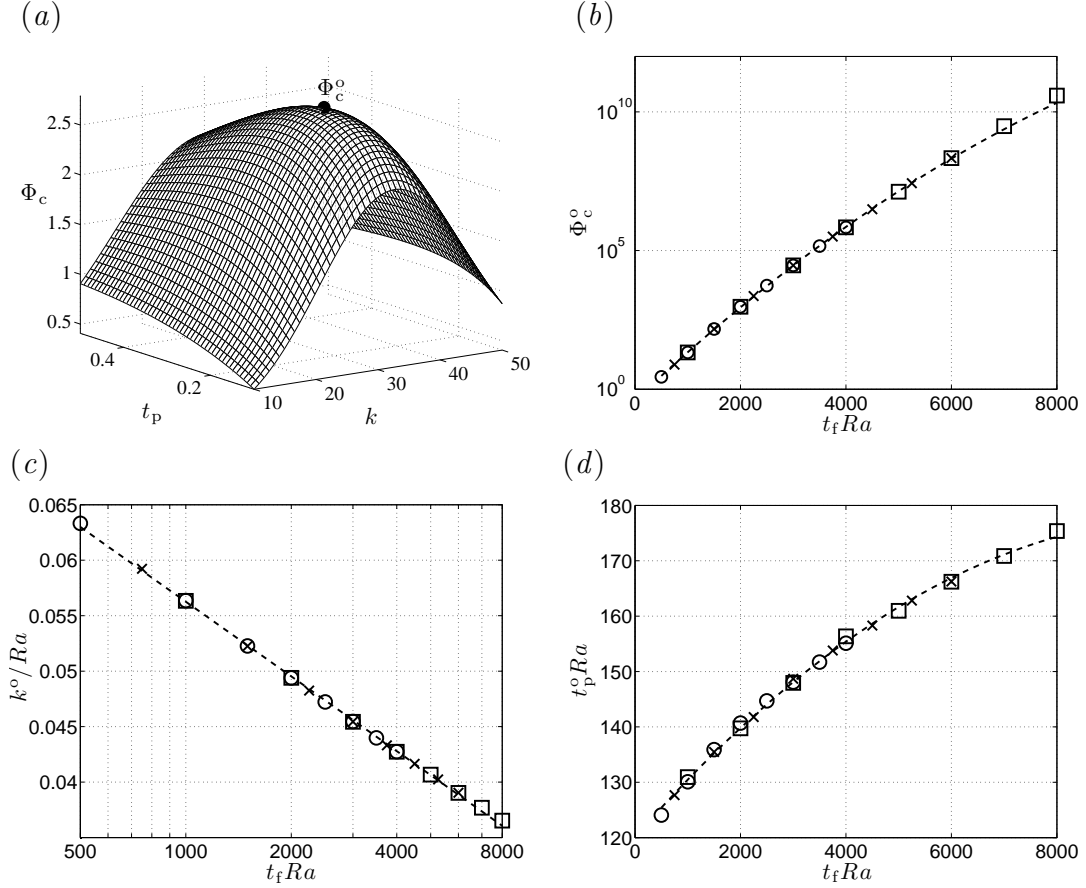


Figure 2.13: The optimal MOP point (Φ_c^o, k^o, t_p^o) as a function of t_f and Ra . (a) Φ_c vs. t_p and k for $Ra = 500$ and $t_f = 1$. The solid dot marks (Φ_c^o, k^o, t_p^o) . (b) Φ_c^o vs. $t_f Ra$ for $Ra = 500$ (circles), $Ra = 750$ (crosses), and $Ra = 1000$ (squares). The dashed line shows relationship (2.41). (c) k^o/Ra vs. $t_f Ra$ for $Ra = 500$ (circles), $Ra = 750$ (crosses), and $Ra = 1000$ (squares). The dashed line shows relationship (2.42). (d) $t_p^o Ra$ vs. $t_f Ra$ for $Ra = 500$ (circles), $Ra = 750$ (crosses), and $Ra = 1000$ (squares). The dashed line shows relationship (2.43).

those produced, using the COP scheme. The optimal initial perturbation times, t_p^o , however, are roughly twice as large as those for the COP scheme due to the large initial damping periods experienced by the MOP perturbations. The optimal initial time, t_p^o , is also more sensitive to t_f than the COP scheme. Recall from §2.4.3, that the optimal initial perturbation time would require *a priori* knowledge of the onset time of convection, i.e. $t_f = t_o$. Because of the increased sensitivity of t_p^o to t_f , the optimal MOP perturbations are expected to be more sensitive to initial perturbation amplitude, A_∞ , than the COP perturbations.

2.5.4 Comparison with eigenvalue and initial value problems

In this section, the modified optimization procedure is compared to previously published linear stability methods that ensure perturbations are localized within the boundary layer. The first approach approximates the vertical domain as semi-infinite. In this case there is a similarity solution for the base-state, $c_b = 1 - \text{erf}(\xi)$, where $\xi(z, t) = z\sqrt{Ra/(4t)}$ is the similarity variable. Riaz *et al.* (2006) demonstrated that a quasi-steady modal analysis with respect to the (ξ, t) space produces eigenmodes concentrated in the boundary layer. For convenience of notation, this eigenvalue problem is referred to as the QSSA $_\xi$ problem. The eigenvectors of the QSSA $_\xi$ problem are c^ξ and w^ξ . The second procedure considered is the solution of the forward IVP (2.5)–(2.7) using $c_p = c_{\text{dm}}$, where c_{dm} is the “dominant mode” of Riaz *et al.* (2006) given by,

$$c_{\text{dm}}(z) = \xi e^{-\xi^2}. \quad (2.44)$$

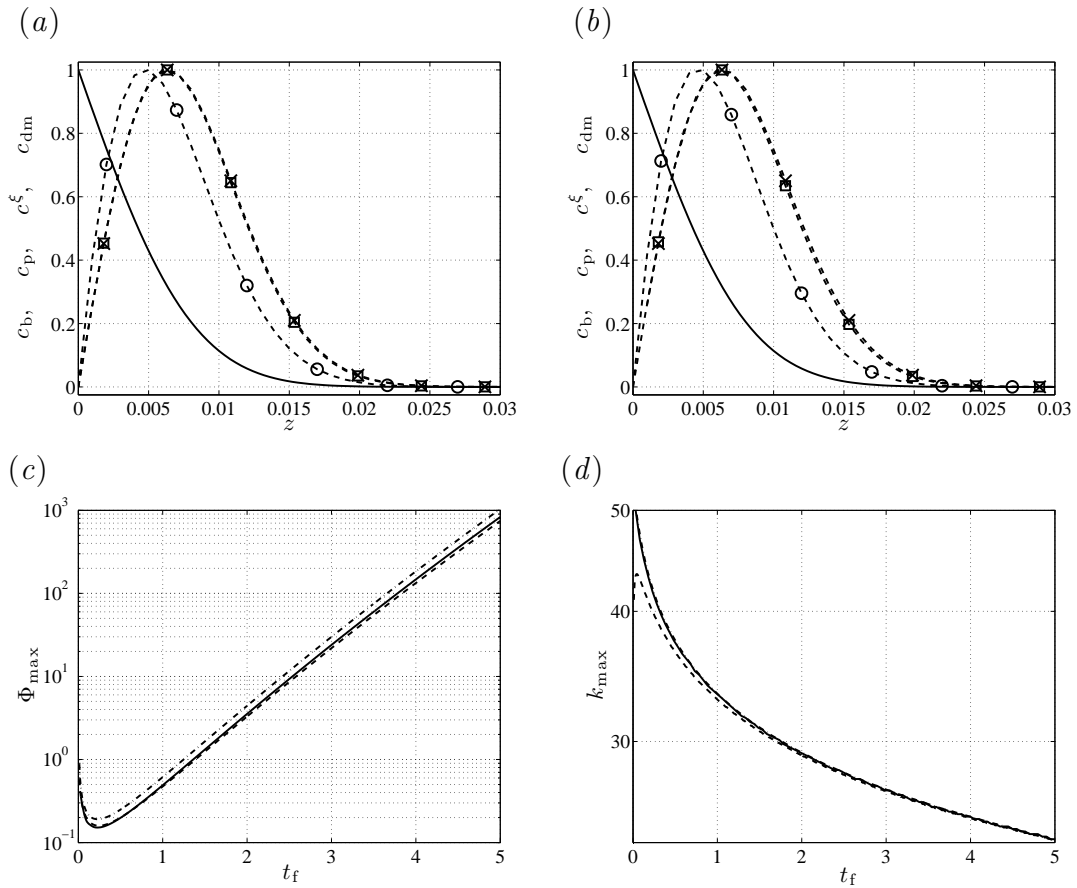


Figure 2.14: Comparison of modified optimization with QSSA in self-similar space and IVP with $c_p = c_{dm}$ for $Ra = 500$. (a) Base-state, c_b (solid line), initial MOP profile (circles), dominant QSSA $_{\xi}$ eigenmode, c^{ξ} (squares), and c_{dm} perturbation (2.44) (crosses) at $t_p = 0.01$ for $k = 10$. (b) Same as in panel (a) for $k = 50$. (c)–(d) Temporal evolution of Φ_{max} and k_{max} for $t_p = 0.01$ using MOP (solid line), QSSA $_{\xi}$ (dashed line), and initial condition (2.44) (dash-dotted line).

Initial condition (2.44) is the leading-order term of a Hermite polynomial expansion in the (ξ, t) space and has been used in numerous previous studies (Ben *et al.*, 2002; Elenius *et al.*, 2012; Kim & Choi, 2011, 2012; Pritchard, 2004; Riaz *et al.*, 2006; Selim & Rees, 2007*a*; Wessel-Berg, 2009).

Figure 2.14(*a*) illustrates the initial perturbation concentration profiles, $\widehat{c}(z, t_p)$, produced by the MOP (circles), dominant QSSA $_{\xi}$ eigenmode (squares), and initial condition (2.44) (crosses), for $t_p = 0.01$, $Ra = 500$, and $k = 10$. Figure 2.14(*b*) repeats figure 2.14(*a*) for the larger wavenumber, $k = 50$. In both figures, the base-state is shown as a solid line. For both wavenumbers, the three methodologies produce qualitatively similar profiles. The profiles produced by QSSA $_{\xi}$ and c_{dm} are indistinguishable, while the MOP profiles have maxima closer to $z = 0$. Note that the MOP profiles support slightly larger initial magnitudes, A_{∞} , than the QSSA $_{\xi}$ and c_{dm} profiles, without producing negative net concentrations, c_{net} .

Figure 2.14(*c*) illustrates results for Φ_{max} versus t_f obtained using the MOP (solid line), QSSA $_{\xi}$ (dashed line), and initial condition (2.44) for $t_p = 0.01$, $0.03 \leq t_f \leq 5$, and $Ra = 500$. The three procedures again produce similar results, though initial condition (2.44) produces marginally larger amplifications. Note that the QSSA $_{\xi}$ amplifications are obtained by first transforming the dominant QSSA $_{\xi}$ growth rates to the (z, t) coordinates using a L^2 norm, before integrating equation (2.33). Figure 2.14(*d*) illustrates the corresponding dominant wavenumbers, k_{max} , of the three procedures. The results produced by initial condition (2.44) and the MOP are indistinguishable.

2.6 Direct Numerical Simulations

Two-dimensional direct numerical simulations (DNS) of the nonlinear governing equations (2.1)–(2.2) are performed using a traditional pseudospectral method with spectral spatial accuracy (Peyret, 2002). The horizontal domain is truncated to $x \in [0, L]$ with periodic boundary conditions on $x = 0$ and $x = L$. Equations (2.1)–(2.2) are then discretized spatially using Chebyshev polynomials in the vertical z direction and a Fourier expansion in the horizontal x direction. The advection-diffusion equation is discretized temporally using a third-order, semi-implicit, backwards-difference scheme (Peyret, 2002). This temporal discretization is chosen for its favorable stability and allows us to investigate small initial times, $t_p \rightarrow 0$. The initial concentration field is prescribed at $t = t_p$ as

$$c_{\text{dns}}(z, x) = c_b(z) + A_\infty \frac{c_i(x, z)}{\|c_i\|_\infty}, \quad (2.45)$$

where A_∞ is the initial perturbation magnitude measured with respect to the infinity norm of the perturbation concentration field, c_i .

2.6.1 Simulations of physical systems

To emulate physical experiments, DNS is performed in which the boundary layer is simultaneously perturbed with all wavenumbers resolved numerically,

$$c_i(x, z) = \sum_{m=0}^{N/2-1} a_m \cos\left(\frac{2\pi m}{L}x\right) G(z)F(z), \quad (2.46)$$

where N is the number of collocation points in the x direction, and $-1 \leq F(z) \leq 1$ is a random function generated using Fortran's random number generator. The co-

| Case | ζ_c | σ | Symbol |
|------|-----------|----------|---------|
| 1 | 0.50 | 0.05 | Circle |
| 2 | 0.50 | 0.10 | Square |
| 3 | 0.50 | 0.15 | Cross |
| 4 | 0.25 | 0.10 | Diamond |
| 5 | 0.75 | 0.10 | Plus |

Table 2.2: The parameters used for the Gaussian, $G(z)$.

efficients a_m are computed to ensure that each horizontal Fourier mode is perturbed with equal energy. The following values, $L = 4\pi$ and $N = 1024$, are used in order to resolve wavenumbers, $k = 0, 0.5, 1, \dots, 255$. To ensure that c_1 satisfies the boundary condition at $z = 0$ and remains concentrated within the boundary layer, the Gaussian function is employed,

$$G(z) = \begin{cases} 0 & \text{if } z = 0, \\ \exp\left(-\frac{1}{2}\left(\frac{\zeta - \zeta_c}{\sigma}\right)^2\right) & \text{if } 0 < z \leq \delta, \\ 0 & \text{if } \delta < z \leq 1, \end{cases} \quad (2.47)$$

where $\zeta = z/\delta$, ζ_c is the mean and σ is the standard deviation. For example, when $\zeta_c = 0.5$, the peak of the Gaussian function is located midway between $z = 0$ and $z = \delta$. This study varies the peak location, ζ_c , and the width, σ , to recreate several experimental possibilities listed in table 2.2.

Figure 2.15(a) illustrates the temporal evolution of the dominant wavenum-

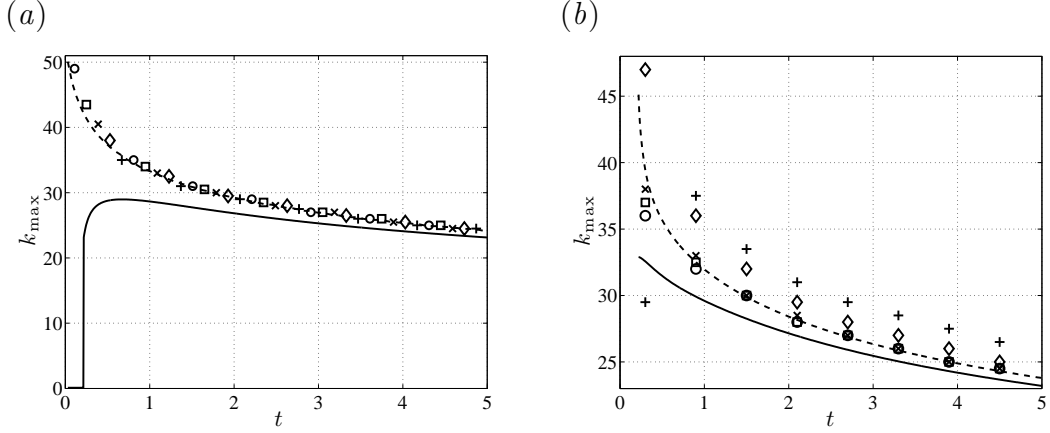


Figure 2.15: (a) Temporal evolution of dominant wavenumbers, k_{\max} , produced by DNS (symbols, see table 2.2), COP (solid line), and MOP (dashed line) for $Ra = 500$ and $t_p = 0.01$ (b) Same as in panel (a) for $t_p = 0.2$.

bers, k_{\max} , produced by COP (solid line), MOP (dashed line), and five DNS recreating the experimental conditions in table 2.2, for $Ra = 500$ and $t_p = 0.01$. All simulations are run using the initial amplitude $A_\infty = 10^{-4}$ to produce a long linear regime, $t_o > 5$, to facilitate comparison of the dominant wavenumbers predicted by COP, MOP and DNS. Excellent agreement between the dominant wavenumbers produced by the MOP and DNS are observed, while those predicted by the COP show poor agreement.

Figure 2.15(b) repeats figure 2.15(a) for the initial perturbation time $t_p = 0.2$, chosen to be near the optimal perturbation time, t_p^o . Note that the DNS results for k_{\max} have a much wider spread than those for $t_p = 0.01$. This likely occurs because the initial damping period is much shorter for $t_p = 0.2$. Overall, MOP shows much better agreement with DNS than COP. For cases 1, 2, and 3 (see table 2.2) the agreement between MOP and DNS is excellent. For cases 4 and 5, MOP

underpredicts k_{\max} , though it still outperforms COP. The improved agreement for cases 1, 2, and 3 may stem from the fact that the boundary layer was perturbed near $z = 0.5\delta$ in these cases. In cases 4 and 5, the layer was perturbed near $z = 0.25\delta$ and $z = 0.75\delta$, respectively.

2.6.2 Extent of linear regime and onset of convection

In the remaining section, it is shown that there exists a well-defined linear regime preceding onset of convection. The onset time t_o is measured for different values of A_∞ and t_p by specifying the following initial concentration field,

$$c_{\text{dns}}(x, z) = c_b(z) + A_\infty \cos(kx) \frac{c_p(z)}{\|c_p\|_\infty}, \quad (2.48)$$

where c_p are the optimal initial profiles determined by COP or MOP. Motivated by experiments (Blair & Quinn, 1969; Kaviany, 1984), the current study defines t_o as the time at which $dJ/dt = 0$, where J is the mean flux of CO_2 into the brine given by,

$$J(t) = -\frac{1}{L} \int_0^L \frac{1}{Ra} \frac{\partial c_{\text{dns}}}{\partial z} \Big|_{z=0} dx. \quad (2.49)$$

Note from (2.49) that perturbations oscillating sinusoidally in the horizontal direction have no net effect on J . Consequently, during the linear regime, the net flux is due to pure diffusion of the base-state, i.e. $J = J_b$. The deviation of the DNS results for J from J_b is due to the growth of a zero-wavenumber mode, $k = 0$, due to nonlinear interactions (Jhaveri & Homsy, 1982). To further quantify the duration of the linear regime, this study also measures the time, $t = t_l$, for which $J/J_b = 1.01$.

Figure 2.16(a) presents DNS results for J using the optimal c_p profile produced

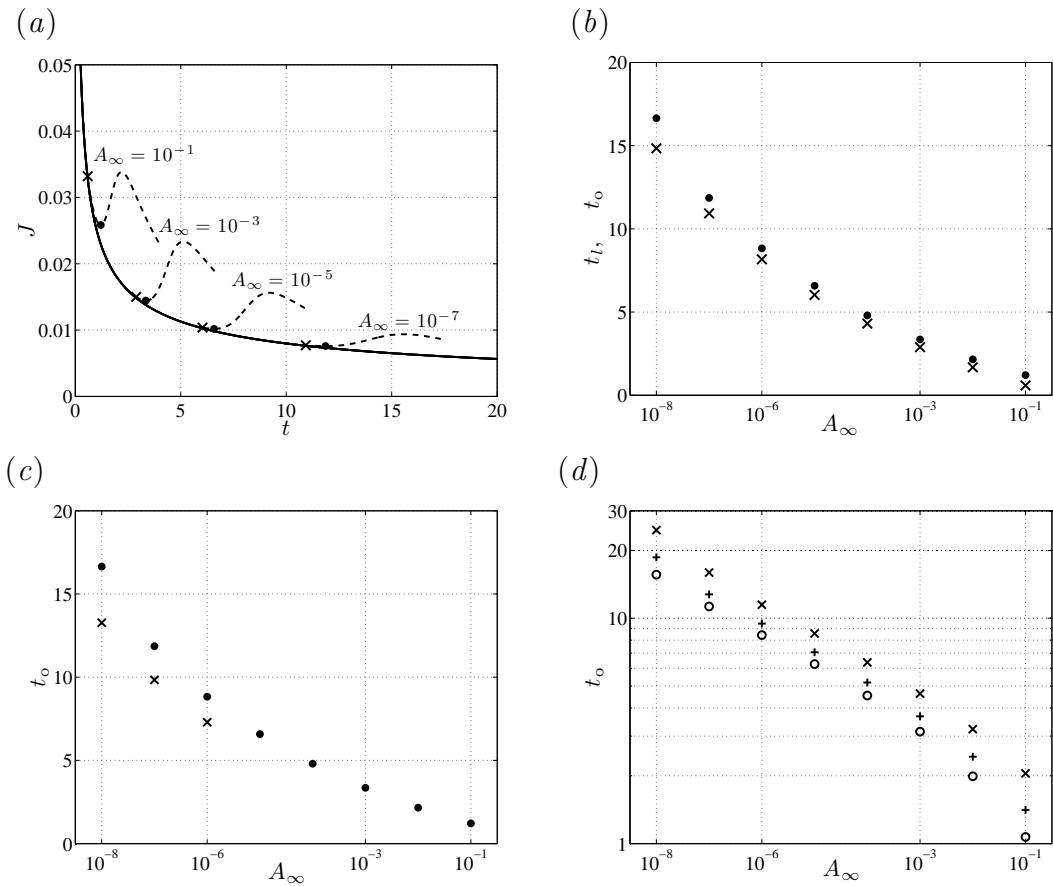


Figure 2.16: DNS results for $Ra = 500$ and $k = 30$ (a) the flux due to base-state, J_b (solid lines), and the flux from DNS, J , (dashed lines) using the MOP c_p profile at $t_p = 0.1$. The crosses denote t_l while the solid dots denote t_o . (b) t_l (crosses) and t_o (solid dots) vs. A_∞ using the MOP c_p profile at $t_p = 0.1$. (c) t_o vs. A_∞ using the COP (crosses) and MOP (solid dots) c_p profiles at $t_p = 0.1$. (d) t_o vs. A_∞ using the MOP c_p profiles at $t_p = 0.01$ (crosses), $t_p = 0.05$ (plus signs), and $t_p = 0.2$ (circles). Note that a log scale has been used for t_o .

by MOP for $t_p = 0.1$, $t_f = 5$, $k = 30$, and $Ra = 500$. Note that the MOP c_p profiles are insensitive to the final time when $t_f > 1$. The solid line shows the temporal evolution of the flux due to the base-state, J_b , while the dashed lines show DNS results for J when $A_\infty = 10^{-1}$, 10^{-3} , 10^{-5} , and 10^{-7} . The times, t_l and t_o , are marked with solid dots and crosses respectively. The flux J initially agrees with J_b and then deviates after $t = t_l$ due to nonlinear effects. The initial linear regime exists even in the case of large initial amplitude $A_\infty = 10^{-1}$. Figure 2.16(b) illustrates t_l (crosses) and t_o (solid dots) for various perturbation amplitudes A_∞ .

Figure 2.16(c) illustrates t_o versus A_∞ using the optimal profiles produced by COP (crosses) and MOP (solid dots) for $t_p = 0.1$, $t_f = 5$, $k = 30$, and $Ra = 500$. The COP scheme produces negative net concentration fields, c_{net} , for all finite perturbation amplitudes, see table 2.1. For illustration purposes, the maximum amplitude for COP to is arbitrarily set $A_\infty = 10^{-6}$ for which $c_{\text{net}}^{\text{min}} = -4.1 \times 10^{-7}$. In this case, COP produces onset times as low as $t_o = 7.29$ for $A_\infty = 10^{-6}$. Note, however, that the onset times predicted by COP cannot be realized in physical systems because of $c_{\text{net}}^{\text{min}} < 0$, and are shown for illustration purposes only. In comparison, the MOP supports finite initial amplitudes as large as $A_\infty = 10^{-1}$ for which $t_o = 1.21$. This study concludes that the perturbations produced by the MOP are more likely to trigger onset of convection in physical systems.

Figure 2.16(d) illustrates t_o versus A_∞ using the MOP c_p profiles at $t_p = 0.01$ (crosses), $t_p = 0.05$ (plus signs), and $t_p = 0.2$ (circles) for $t_f = 5$, $Ra = 500$, and $k = 30$. Onset of convection occurs later for smaller t_p due to the strong initial damping periods. Note that a log scale has also been used for t_o to highlight the

difference for larger A_∞ . For large amplitude perturbations, the onset of convection can occur around $t_o \approx 1$. For typical aquifer conditions (see §4.3), with permeability $K = 10^{-14} \text{ m}^2$ and height, $H = 51 \text{ m}$, this corresponds to a dimensional onset time of $t_o^* \approx 165$ years.

2.7 Conclusions and summary

This chapter investigated the linear stability of gravitationally unstable, transient, diffusive boundary layers in isotropic, homogeneous porous media. First, a classical optimization procedure (COP) was performed to determine optimal perturbations with maximum amplifications. Previously, Tan & Homsy (1986) and Doumenc *et al.* (2010) have observed that perturbation amplification is sensitive to the perturbation flow field used to measure perturbation magnitude. Because this sensitivity has not been addressed for applications to CO₂ sequestration, this study considered three different measures of perturbation amplitude that maximize either the perturbation concentration field, vertical velocity field, or the sum of the perturbation velocity and concentration fields, which is referred to as the total energy. It was determined that maximizing the perturbation concentration field naturally maximizes the total energy. Maximizing the perturbation velocity field, however, does so at the expense of the concentration field and total energy. Consequently, this dissertation focusses on perturbations that maximize the concentration field because these are expected to be the dominant trigger for onset of nonlinear convection.

As the final time, t_f , increases, the optimal initial perturbations eventually

converge to a fixed shape and cease to vary with increasing t_f . This occurs because the final perturbations at $t = t_f$ rapidly tend to the dominant quasi-steady eigenmode. In fact, for the current problem, the quasi-steady modal analysis is a good approximation to the COP. Both methods produce nearly identical amplifications and dominant wavenumbers. This suggests that the deviation of the optimal perturbations from the dominant eigenmodes at small times may be primarily due to the transient base-state, rather than the nonorthogonality of the quasi-steady eigenmodes. This is in stark contrast to wall-bounded shear flows for which non-orthogonal eigenmodes often play a dominant role.

To judge the relevance of optimal perturbations to physical systems, it is shown that every perturbation has a maximum allowable initial amplitude above which the sum of the base-state and perturbation produces unphysical negative concentrations. This study demonstrates that the optimal initial perturbations predicted by the COP produce unphysical negative concentrations for all finite initial amplitudes. Consequently, onset of convection in physical systems is more likely triggered by suboptimal perturbations that support finite amplitudes. To explore this alternate path to onset of convection, a modified optimization procedure (MOP) is developed that constrains the initial perturbations to be concentrated within the boundary layer.

An integral characteristic of the MOP is the concept of a filter function, $\Psi(z)$, that effectively filters out perturbations with concentration fields extending beyond the boundary layer, see equation (2.35). The choice of filter function is not unique, and determines both the maximum allowable initial perturbation amplitude as well

as the subsequent perturbation amplification. Filter functions that concentrate the initial perturbation close to $z = 0$ support large initial amplitudes, but produce small subsequent amplifications. Filter functions that concentrate the perturbations near the boundary layer depth support small initial amplitudes, but produce large subsequent amplifications. This raises the possibility that there exists an optimal filter function that balances the effects of the initial amplitude and subsequent amplification in order to minimize the onset time for convection. This is an avenue for future work. This study focussed on perturbations produced by $\Psi = c_b^{-1}$ because this naturally concentrates perturbations in regions of large base-state concentration, and because it shows good agreement with corresponding DNS of physical systems.

The alternate path to onset of convection taken by the MOP features smaller amplifications and larger dominant wavenumbers than the COP, especially at small initial perturbation times, $t_p \ll t_p^o$. This occurs because the dominant MOP perturbations are concentrated within the boundary layer, and consequently experience more initial damping than the COP perturbations. It is shown that the results produced by MOP agree well with the “dominant mode” approach of Riaz *et al.* (2006) as well as quasi-steady modal analyses performed in the similarity space of the base-state (Riaz *et al.*, 2006; Selim & Rees, 2007a; Wessel-Berg, 2009).

To emulate physical experiments, DNS is performed in which the boundary layer is simultaneously perturbed with all wavenumbers resolved by the simulations. The perturbations have a random structure but are concentrated within the boundary layer. The DNS results confirm that physical systems follow the alternate path to convection predicted by the MOP scheme and show poor agreement with COP.

Furthermore, the MOP perturbations support large initial amplitudes, $A_\infty \sim 10^{-1}$, and produce early onset times for nonlinear convection. In contrast, the COP perturbations support neither finite amplitudes nor finite onset times.

Chapter 3: Effect of viscosity contrast on gravity-driven instabilities in porous media

This chapter examines the effect of viscosity contrast on the linear stability of gravitationally unstable, transient, diffusive layers in porous media. The analysis presented in this chapter helps evaluate experimental observations of various boundary layer models that are commonly used to study the sequestration of CO₂ in brine aquifers. It is shown that models that allow the interface between CO₂ and brine to move, in an effort to capture the effect of dissolution, can be more unstable compared to conventional, fixed interface models. Also, diffusive layers are generally found to be more unstable when viscosity decreases with depth within the layer compared to when viscosity increases with depth. This behavior is in contrast to the classical understanding of gravitationally unstable diffusive layers subject to mean flow. For that case, greater instability is associated with the displacement of a more viscous fluid in the direction of gravity by a less viscous fluid. The new phenomenon can be explained as a special case of the classical displacement problem that depends on the relative magnitude of the displacement and buoyancy velocities. For such classical flows, there exists a critical viscosity ratio that determines whether the flow is buoyancy dominated or displacement dominated. The new behavior is explained in

terms of the interaction of vorticity components related to gravitational and viscous effects.

3.1 Overview

During CO₂ sequestration, free CO₂ is trapped as it dissolves into brine across a two-phase interface, see figure 3.1. Once dissolved, the trapped CO₂ diffuses downwards to form a solute boundary layer. These diffusive boundary layers have been studied with the help of various models. These models often assume that CO₂ dissolves into brine across the two-phase interface at constant pressure and temperature. The concentration of dissolved CO₂ at the interface across which CO₂ dissolves into brine is therefore taken to be constant. The interface motion resulting from dissolution is considered to be small by one popular model in comparison with other relevant time scales in the problem. The interface location is therefore considered to be fixed. This model is referred to as in this chapter as the fixed interface model (Ennis-King *et al.*, 2003; Riaz *et al.*, 2006; Slim & Ramakrishnan, 2010). This model is a popularly used in many theoretical and computational studies and also in previous chapter of this study. An alternative model of the diffusive boundary layer attempts to incorporate the motion of the interface by considering a diffused layer that separates two initially quiescent, miscible fluids. For this model, a non-monotonic density-concentration relationship is used to produce both stable and unstable regions within the boundary layer (Backhaus *et al.*, 2011; Ehyaei & Kiger, 2014; MacMinn *et al.*, 2012; Neufeld *et al.*, 2010). The overall result is the

apparent motion of the diffusive layer after the onset of nonlinear convection. This setup as the moving interface model. Because of the relative ease of laboratory setup, the moving interface model has gained more popularity with experimental studies compared with the fixed interface model. The moving interface model however has not been well explored and a fundamental insight regarding the physical behavior is lacking. Consequently, it is unclear how the stability characteristics of the two models compare with each other.

From a practical stand point, differences in the viscosities of CO₂-brine solution and CO₂-free brine are small (Bando *et al.*, 2004; Kumagai & Yokoyama, 1999). However, because of physical constraints, the fluids employed by experimental studies lead to very different viscosity contrasts than what is expected in practice. In some cases, the viscosity of the experimental fluid representing CO₂-brine solution is about 20 times larger than that of the fluid representing CO₂-free brine solution Backhaus *et al.* (2011). Since the fixed and moving interface models are frequently used as analogs for physical systems, the effect of viscosity contrast on stability behavior needs to be understood to properly interpret corresponding experimental observations. In order to facilitate such an understanding, this study draws comparison with the closely related problem of the gravitationally unstable diffusive layer subject to mean flow. The moving interface model is a special case (with zero mean flow) of this displaced interface problem. For this classical problem the viscosity contrast, density difference and mean flow, all interact to affect stability behavior (Manickam & Homsy, 1995). Evaluation of such interactions is expected to facilitate a deeper understanding of relevant physical mechanisms for the moving

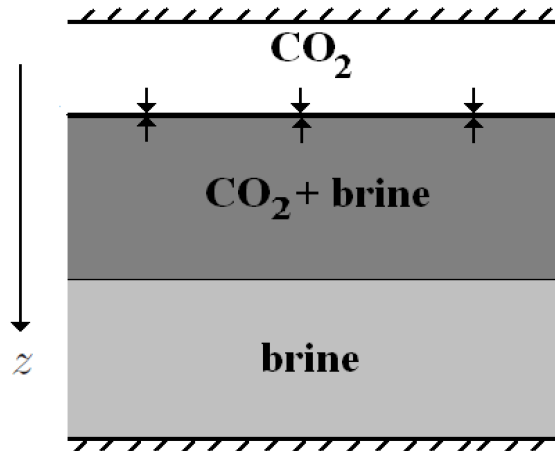


Figure 3.1: Sketch of CO_2 sequestration. Dissolution of CO_2 into brine occurs across the two-phase interface, indicated by pairs of counter-pointing arrows. The gravitationally unstable CO_2 layer within brine plays a vital role in determining the interfacial dissolution rate.

interface problem, and also by extension for the fixed interface problem.

The main highlights of this chapter are; (i) investigation for the effect of the viscosity contrast for the fixed and moving interface models and (ii) exploration of the interaction of mean flow, buoyancy velocity and viscosity contrast for understanding the transition from displacement dominated to buoyancy dominated behavior. These two features are explored by means of a quasi-steady-state eigenvalue approach in self-similar space of the diffusive boundary layer. The suitability of this approach is confirmed by our findings in Chapter 2. The work is divided as follow. The geometries and governing equations are explained in §3.2. The results are discussed in §3.3 along with conclusions in §3.4.

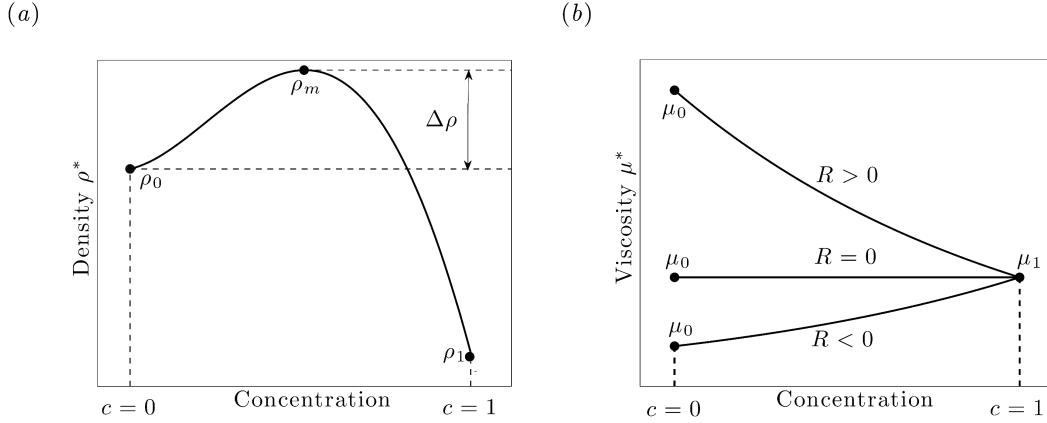


Figure 3.2: (a) Non-monotonic density-concentration profile employed in a MI model (b) Monotonic viscosity-concentration profiles for various log mobility ratios, $R = \ln(\mu_0/\mu_1)$.

3.2 Governing equations

In order to evaluate experimental setups based on the moving interface (MI) model of the diffusive boundary layer, this study uses a non-monotonic density profile, ρ^* , of the form illustrated in figure 3.2(a). This density profile can be represented as,

$$\rho^* = \rho_0 + \Delta\rho F(c), \quad (3.1)$$

where the function $F(c) = \sum_{n=1}^4 a_n c^n$, determines how density varies with concentration c . The end point densities related to $c = 0$ and $c = 1$ are ρ_0 and ρ_1 , respectively, and ρ_m is the maximum density. Note that the fluid with $c = 1$ lies above the fluid with $c = 0$. The quantity, $\Delta\rho = \rho_m - \rho_0$, indicates the strength of unstable density stratification. The function $F(c)$ is normalized to the maximum

value of one. The density profile is linear when $a_1 = 1$ and $a_n = 0$ for $n = 2, 3, 4$. Following previous works, this study employs a monotonic viscosity profile illustrated in figure 3.2(b),

$$\mu^* = \mu_1 \exp(R(1 - c)), \quad (3.2)$$

where $R = \ln(\mu_0/\mu_1)$ is the log mobility ratio, μ_1 is the viscosity of the fluid with $c = 1$, and μ_0 is the viscosity of the fluid with $c = 0$.

For the experimental study of Backhaus *et al.* (2011) based on the moving interface model, water and propylene glycol were used as the lighter and heavier fluids, respectively. For that system, the location of the density peak occurs at a concentration of $c \approx 0.38$. A log mobility ratio, $R \approx -3$, fits the viscosity-concentration relationship at a temperature of 120 °F. Neufeld *et al.* (2010), MacMinn *et al.* (2012) and Ehyaei & Kiger (2014) also employ a moving interface model, using methanol/ethylene glycol (MEG) mixtures and water as the lighter and heavier fluids respectively. The location of the density peak and the viscosity differences depend on the composition of the MEG mixture. Typical values of the peak density vary in the range, $0.2 < c < 0.55$ (Huppert *et al.*, 1986), while the log mobility ratios vary approximately in the range, $-1.5 < R < 1$ MacMinn *et al.* (2012). Another experimental study by Slim *et al.* (2013) employs a setup that is closer to the fixed interface model. The authors employed potassium permanganate (KMnO_4) in water as an analogous model for CO_2 in brine. The KMnO_4 -water mixture approximately satisfies a linear density profile and a log mobility ratio of $R \approx 0.04$ fits the viscosity-concentration relationship at 77 °F (Jones & Fornwalt, 1936).

The porous aquifer is modeled as isotropic, homogeneous, and of infinite horizontal extent and finite depth H . The vertical coordinate, z , is positive in the direction of gravity, g . The porous medium is characterized by permeability, K , dispersivity, D , and porosity, ϕ . The characteristic values are H for length, μ_1 for viscosity, $K\Delta\rho g/\mu_1$ for velocity, $\mu_1 H/K\Delta\rho g\phi$ for time and $\Delta\rho gH$ for pressure. Using these characteristics values, one obtains the following non-dimensional governing equations,

$$\mu(c)\mathbf{v} + \nabla p - F(c)\mathbf{e}_z = 0, \quad \nabla \cdot \mathbf{v} = 0, \quad \frac{\partial c}{\partial t} + \mathbf{v} \cdot \nabla c - \frac{1}{Ra} \nabla^2 c = 0. \quad (3.3)$$

The Rayleigh number is defined as $Ra = K\Delta\rho gH/\phi D\mu_1$. The symbol $\mathbf{v} = [u, v, w]$ is the nondimensional velocity vector, and p is the nondimensional pressure obtained from the dimensional pressure \hat{p} through the relation $p = (\hat{p} - \rho_o g z)/\Delta\rho gH$. The symbol \mathbf{e}_z is the unit vector in the z -direction.

The boundary conditions for (3.3) depend on the model. For the fixed interface (FI) model, the boundary conditions for (3.3) are,

$$c|_{z=0} = 1, \quad \frac{\partial c}{\partial z}\Big|_{z=1} = 0, \quad w|_{z=0} = w|_{z=1} = 0. \quad (3.4)$$

Equations (3.3) and (3.4) admit the concentration base state, $c_b^F(z, t) = \operatorname{erfc}(z\sqrt{Ra/4t})$, see figure 3.3(a) for illustration. The velocity base-state is $\mathbf{v}_b = 0$.

For the MI model, the study uses boundary conditions that allow diffusion in two opposite directions,

$$\frac{\partial c}{\partial z}\Big|_{z=-1} = \frac{\partial c}{\partial z}\Big|_{z=1} = 0, \quad w|_{z=-1} = w|_{z=1} = 0. \quad (3.5)$$

Equations (3.3) and (3.5) admit the base-states, $c_b^M(z, t) = \operatorname{erfc}(z\sqrt{Ra/4t})/2$, see

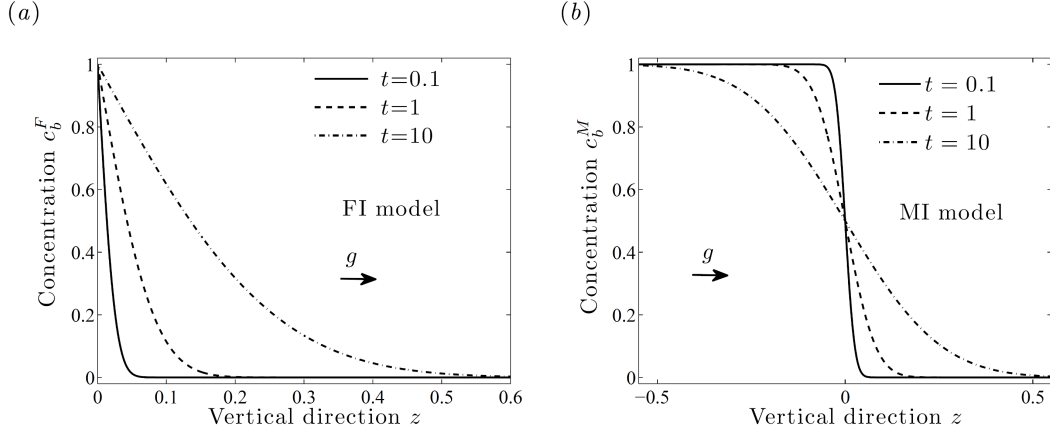


Figure 3.3: Concentration base-states for Rayleigh number, $Ra = 500$, at various instants of time t . (a) Base-state for FI model, $c_b^F = \text{erfc}(z\sqrt{Ra/4t})$. (b) Base-state for MI model, $c_b^M = 0.5 \text{erfc}(z\sqrt{Ra/4t})$.

figure 3.3(b), and $\mathbf{v}_b = 0$. These expressions of the base-states, c_b^F and c_b^M , are valid as long as the boundary layer remains far away from the boundaries at $z=1$ for the FI model and $z = \pm 1$ for the MI model respectively. This holds true when $\sqrt{Ra/4t} > 3$. (Riaz *et al.*, 2006)

The linear stability of various diffusive boundary layer models is studied with respect to small wavelike perturbations of the form,

$$\tilde{c} = \hat{c}(z, t)e^{i(\alpha x + \beta y)}, \quad \tilde{\mathbf{v}} = \hat{\mathbf{v}}(z, t)e^{i(\alpha x + \beta y)}, \quad (3.6)$$

where $i = \sqrt{-1}$, α and β are wavenumbers in the x - and y -directions respectively, and $\hat{c}(z, t)$ and $\hat{\mathbf{v}}(z, t)$ are time-dependent perturbation profiles in the z -direction. Substituting $c = c_b + \tilde{c}$ and $\mathbf{v} = \mathbf{v}_b + \tilde{\mathbf{v}}$ into equation (3.3) and linearizing about base-states, one obtains the following initial value problem for \hat{c} and \hat{w} ,

$$\left(\frac{\partial}{\partial t} - \frac{1}{Ra} \frac{\partial^2}{\partial z^2} - k^2 \right) \hat{c} + \frac{\partial c_b}{\partial z} \hat{w} = 0, \quad (3.7)$$

$$\left(\frac{\partial^2}{\partial z^2} - R \frac{\partial c_b}{\partial z} \frac{\partial}{\partial z} - k^2 \right) \hat{w} + Gk^2 \hat{c} = 0, \quad (3.8)$$

where $k = \sqrt{\alpha^2 + \beta^2}$, $G = 1/\mu(c_b) \partial F(c_b)/\partial c_b + UR$ and c_b refers to either of the FI or MI base states defined above. Homogeneous Dirichlet boundary conditions for perturbation variables are specified at $z = 1$ and $z = \pm 1$ for the FI and MI models, respectively.

The symbol, $U = U^* \mu_1 / K \Delta \rho g$, refers to the fluid displacement velocity, U^* , scaled with the buoyancy velocity, $K \Delta \rho g / \mu_1$. It indicates the relative strength of the mean flow with respect to buoyancy velocity and is effective only when viscosity varies in the boundary layer, $R \neq 0$. When $U = 0$, equations (3.7)–(3.8) represent either the FI or MI models. When $U \neq 0$, the equations represent the displaced interface model. The coordinate system for the displaced interface model is such that it moves with velocity, $U e_z$. The associated linear stability equations were obtained by first performing coordinate transformations to equations (3.3) and (3.5) before carrying out an expansion using normal modes. Note that due to coordinate transformation, the boundary conditions and resulting base-state for displaced interface model are same as that of the MI model. (Manickam & Homsy, 1995)

Equations (3.7)–(3.8) are analyzed using a quasi-steady-state (QSSA) eigenvalue formulation in the self-similar (ξ, t) space, where $\xi = az$ and $a = \sqrt{Ra/4t}$. (Riaz *et al.*, 2006) The resulting eigenvalue problem may be expressed as

$$\sigma c_e = \frac{\xi}{2} \frac{\partial c_e}{\partial \xi} + \frac{1}{Ra} \left(a^2 \frac{\partial^2}{\partial \xi^2} - k^2 \right) c_e - a \frac{\partial c_b}{\partial \xi} w_e, \quad (3.9)$$

$$\left(a^2 \frac{\partial^2}{\partial \xi^2} - a^2 R \frac{\partial c_b}{\partial \xi} \frac{\partial}{\partial \xi} - k^2 \right) w_e = -Gk^2 c_e, \quad (3.10)$$

with homogeneous Dirichlet boundary conditions for the eigenmodes, c_e and w_e ,

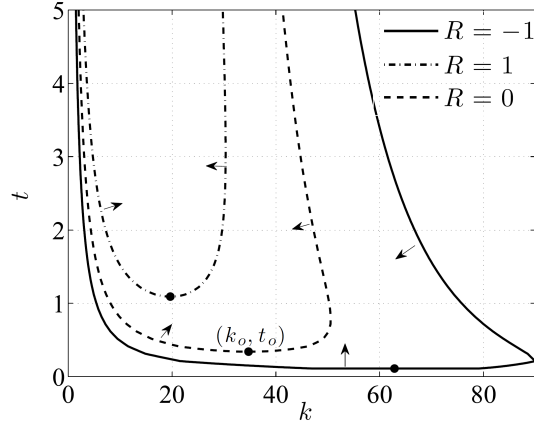


Figure 3.4: Isocontours of $\sigma = 0$ produced by an FI model. Arrows point toward the unstable region, $\sigma > 0$. Solid dots mark the critical points, (k_c, t_c) .

and the eigenvalue, σ , represents the growth rate. The least stable perturbation is defined as the eigenmode with the maximum real value for σ . The growth rates obtained in the self-similar space (ξ, t) are equivalent to the growth rates calculated in the regular space (z, t) when perturbation amplitudes are based on the L_∞ norm. (Tilton *et al.*, 2013) The equations (3.9)–(3.10) are discretized using standard second-order finite difference schemes. For given parameters of k , t and Ra , the generalized eigenvalue problem is solved using function ‘eig’ in MATLAB. The onset time for linear instability, $t = t_c$, is defined as the time at which the growth rate of a perturbation eigenmode first becomes positive. The corresponding wavenumber is called the critical wavenumber, $k = k_o$.

3.3 Results and discussion

This section examines the effect of viscosity contrast on the onset of instability in a gravitationally unstable, transient, diffusive boundary layer. The moving interface model is compared extensively with the fixed interface model and is further explored by considering various types of non-monotonic density-concentration distributions. This section also explores how mean flow and viscosity contrast determines the shift in stability features from that of displacement dominated to those of buoyancy dominated behavior. For the remainder of the study, the Rayleigh number is fixed at $Ra = 500$. Linear stability behavior at other value of $Ra > 50$ can be obtained by a simple rescaling.(Riaz *et al.*, 2006; Tilton *et al.*, 2013)

3.3.1 The fixed interface model

The diffusive boundary layer in the fixed interface (FI) model adopts a linear density-concentration relationship such that $F(c) = c$. Figure 3.4 illustrates the isocontours of growth rates, $\sigma = 0$, in the (k, t) parameter plane for log mobility ratios, $R = -1$ (solid line), $R = 0$ (dashed line), and $R = 1$ (dash-dotted line). The lowest point of the $\sigma = 0$ isocontour corresponds to the critical parameters (k_c, t_c) . For $R = -1$, the critical point is at $k = 66.8$ and $t = 0.1$ respectively. The arrows point towards the unstable zone where the growth rates are greater than zero, $\sigma > 0$. For small times, all perturbation wavenumbers are stable, after which a band of wavenumbers become unstable. When $R = 0$, one recovers the constant viscosity case(Riaz *et al.*, 2006) with the critical point at $(34.7, 0.3)$. The $R = 0$ case

has a smaller band of unstable wavenumbers compared to $R = -1$. The unstable region shrinks further when the viscosity ratio is increased to $R = 1$, resulting in smaller k_c and larger t_c . A similar effect of R on transient diffusive boundary layers has also been observed by Meulenbroek *et al.* (2013).

The dominant wavenumber, k_{max} , is defined as the wavenumber at a given time t for which the largest growth rate is observed,

$$\sigma_{max}(t) = \sup_{0 \leq k < \infty} \sigma(t, k). \quad (3.11)$$

Figure 3.5(a) illustrates the temporal evolution of σ_{max} for $R = -1$ (solid line), $R = 0$ (dashed line), and $R = 1$ (dash-dotted line). The $R = -1$ perturbations have larger σ_{max} compared to $R = 0$ and $R = 1$ perturbations. When $t < 1$, the $R = -1$ perturbations attain growth rates as large as $\sigma_{max} \approx 6$. In contrast, the $R = 1$ perturbations are stable for the same period with $\sigma_{max} < 0$. Figure 3.5(b) illustrates the dominant wavenumbers, k_{max} , for $R = -1$ (solid line), $R = 0$ (dashed line), and $R = 1$ (dash-dotted line). The dominant wavenumbers, k_{max} , monotonically decrease with increasing time. The $R = -1$ perturbations have larger values of k_{max} compared to the $R = 1$ perturbations.

It is found that the increasing strength of the instabilities for decreasing R directly correlates to the perturbation's instantaneous vorticity field,

$$\Omega_e = \frac{k}{\mu(c_b)} c_e - \frac{R}{k} \frac{\partial c_b}{\partial z} \frac{\partial w_e}{\partial z}. \quad (3.12)$$

The individual contributions to vorticity are examined using,

$$I = \int \Omega_e dz = I_1 + I_2, \quad (3.13)$$

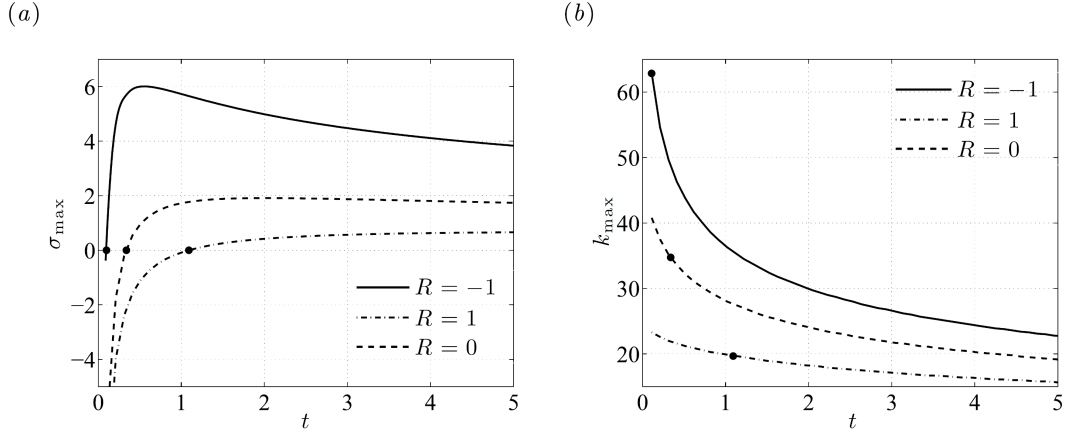


Figure 3.5: Results produced by FI model. (a) Maximum growthrates, σ_{\max} , vs. t . (b) Dominant wavenumbers, k_{\max} , vs. t . The solid points represent the critical point of instability, (k_c, t_c) .

where

$$I_1 = k \int \exp[-R(1 - c_b)] c_e \, dz, \quad I_2 = -\frac{R}{k} \int \frac{\partial c_b}{\partial z} \frac{\partial w_e}{\partial z} \, dz. \quad (3.14)$$

The first integral, I_1 , measures the contribution to vorticity arising from the buoyant forces. When density gradients are unstable, I_1 is positive. The second integral I_2 depends both on the base-state and the velocity perturbation.

Table 3.1 illustrates the values of the integral quantities, I_1 and I_2 , and the growth rate σ for values of R ranging from -3 to 3. The eigenmodes are normalized such that maximum value of c_e is one. The values of I_2 are consistently smaller than I_1 . When $R = 3$, one observes the smallest values for I_1 . This indicates that the buoyancy velocities produced due to the unstable density gradients are small, and consequently, tend to have weak destabilizing effects. With decreasing R , values of I_1 increases till a maximum value is reached at $R = -3$. Larger values

| R | I_1 | I_2 | $I_1 + I_2$ | σ |
|-----|-------|-------|-------------|----------|
| -3 | 12.67 | -5.40 | 7.27 | 23.39 |
| -2 | 5.37 | -1.75 | 3.63 | 8.99 |
| -1 | 2.49 | -0.45 | 2.04 | 1.70 |
| 0 | 1.26 | 0.00 | 1.26 | -2.23 |
| 1 | 0.68 | 0.13 | 0.80 | -4.41 |
| 2 | 0.38 | 0.13 | 0.51 | -5.59 |
| 3 | 0.23 | 0.09 | 0.32 | -6.21 |

Table 3.1: Vorticity values and growth rate produced by the FI model for $k = 30$ and $t = 0.2$

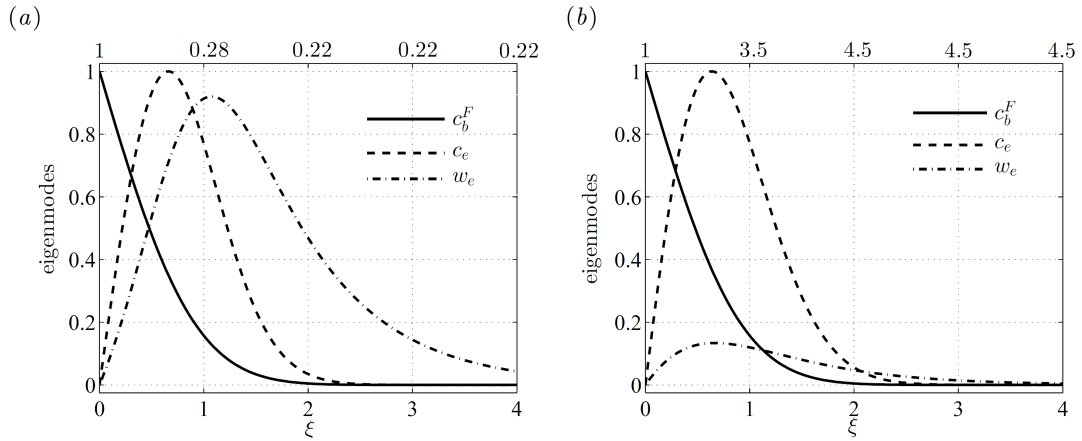


Figure 3.6: Base-state and least stable eigenmodes produced by the FI model as a function of self-similar coordinate, ξ , for $k = 30$, and $t = 0.2$. Viscosity values are presented at the top axis. (a) $R = -1.5$. (b) $R = 1.5$

of the vorticity integral, I , produce higher growth rates, and consequently, produce stronger perturbation fields that promote the formation of instabilities.

Figure 3.6 illustrates the base-state, c_b^F (solid line), concentration eigenmode, c_e (dashed line), and vertical velocity eigenmode, w_e (dash-dotted line) for $R = -1.5$ (panel *a*) and $R = 1.5$ (panel *b*) respectively. The numbers along top axis represent fluid viscosity obtained using $\mu = \exp(R(1 - c_b^F))$. When $R = -1.5$, one observes a large vertical velocity perturbation field, w_e , that is nearly of the same magnitude as the concentration perturbation field c_e . The ratio of the maximum value of w_e and the maximum value of c_e is 0.92. For large value of the log mobility ratio, $R = 1.5$, weaker vertical velocity fields are observed. The ratio of the maximum values drops to 0.13. The drop in magnitudes is because w_e fields associated with $R = 1.5$ are formed in regions of higher viscosity (more resistance to fluid flow) compared to $R = -1.5$. The viscosity variation within the boundary layer also explains why perturbations are concentrated away from $z = 0$ for $R = -1.5$ compared to $R = 1.5$. When $R > 0$, viscosity increases with depth and perturbation peaks are closer to $z = 0$, compared to $R < 0$ where viscosity decreases with depth and perturbation peaks are concentrated in regions away from $z = 0$. Note that the classical behavior of greater instability associated with higher R is due to a source of perturbations arising from the background mean flow, as explained in more detail in section 3.3.4.

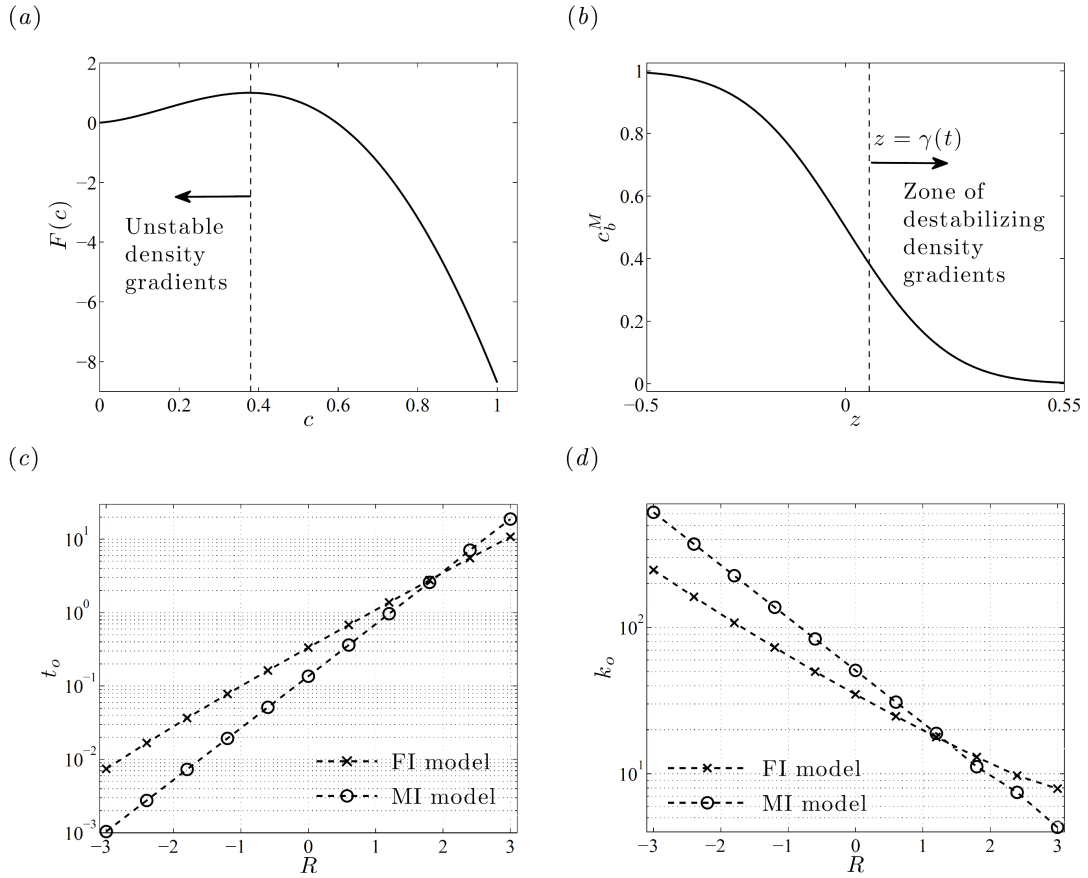


Figure 3.7: Comparison between MI and FI models. (a) Nonmonotonic function F as a function of concentration c , see equation (3.1). The coefficients of $F(c)$ are: $a_1 = 1.06$, $a_2 = 17.31$, $a_3 = -39.35$, $a_4 = 12.28$. (b) c_b^M vs. z for $t = 10$. The density gradients are destabilizing only when $z > \gamma$ (arrow). (c) t_c vs. R . (d) k_c vs. R .

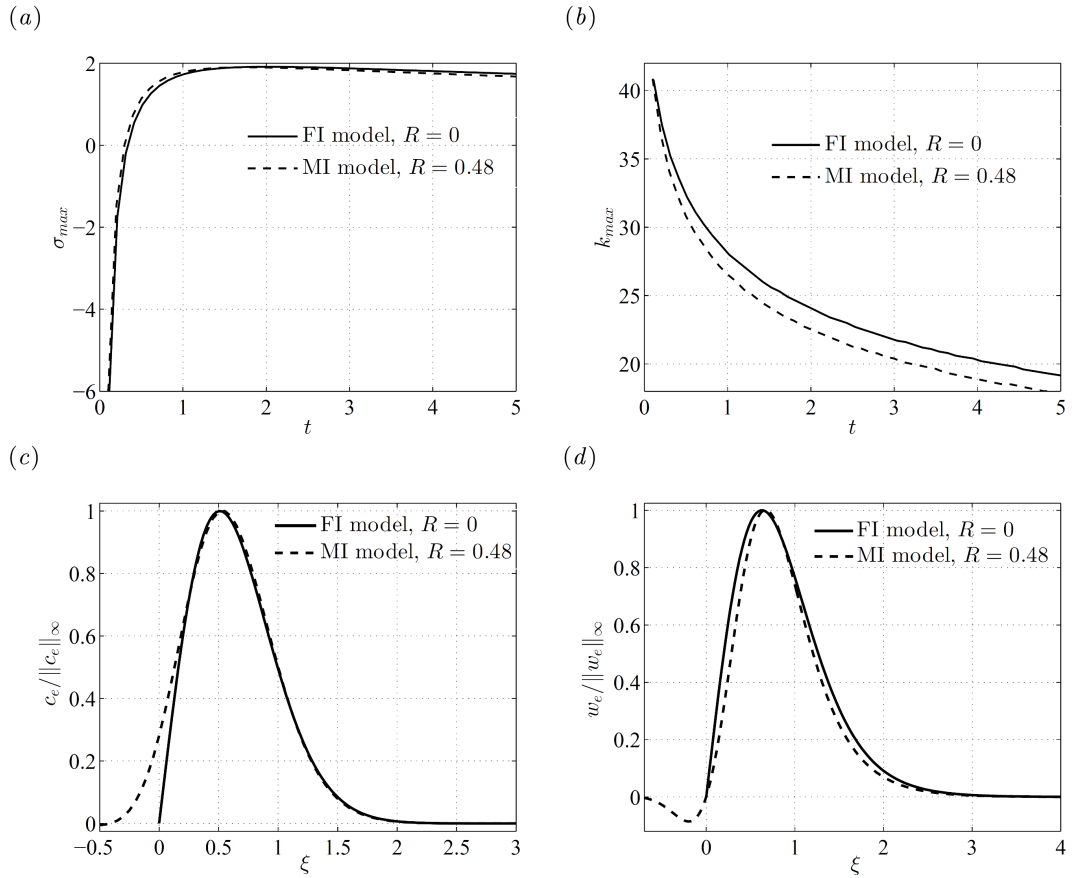


Figure 3.8: Linear stability results for FI with $R = 0$ (solid line) and MI with $R = 0.48$ (dashed line). (a) σ_{max} vs. t . (b) k_{max} vs. t . (c) $c_e / \|c_e\|_\infty$ vs. ξ for $k = 30$ and $t = 1$. (d) $w_e / \|w_e\|_\infty$ vs. ξ for $k = 30$ and $t = 1$.

3.3.2 The moving interface model

This section explores the effect of viscosity contrast on the moving interface (MI) model. A non-monotonic density profile is employed such that the function $F(c)$, see equation (3.1), corresponds to aqueous propylene glycol mixtures, with $c = 0$ and $c = 1$ representing concentrations of pure propylene glycol and water respectively. Figure 3.7(a) illustrates the function $F(c)$. The positive density gradients when $c < 0.38$ promote the formation of instabilities. Figure 3.7(b) illustrates the location of the zone of unstable density gradients within the diffusive layer. Unlike an FI model, where the entire boundary layer is unstable, the unstable density gradients in an MI model exist only when $z > \gamma(t)$ (or $\xi > 0.21$), where $\gamma(t) = 0.21\sqrt{4t/Ra}$.

Figure 3.7(c) illustrates the onset times, t_c , versus the log mobility ratio, R , for the MI (circles) and FI (crosses) models. As expected, the onset times produced by the two models increase with increasing R . A large difference in the onset times occurs especially for small values of R . When $R = -2$, the FI model has onset times, t_c , that are approximately 500% larger than those produced by the MI model. With increasing R , the onset times produced by the two models agree better. For $R \approx 1.8$, the FI and MI models have nearly identical onset times. Figure 3.7(d) illustrates the critical wavenumbers, k_c , versus R for the MI (circles) and FI (crosses) models. As expected, k_c decreases with increasing R . For $R < 1.36$, the MI model has larger k_c compared to the FI model.

The linear stability behavior of the FI and MI models can be made to coincide

when different viscosity contrasts are used with each model. For example, when $R = 0$ for the FI model and $R = 0.48$ for the MI model, the onset times, t_c , predicted by the two models agree with each other. For these parameters, good agreement is obtained even for time, $t > O(t_c)$. This is depicted in figures 3.8(a)–3.8(b) where the temporal evolution of the dominant growth rates, σ_{max} , (panel a) and dominant wavenumbers, k_{max} , (panel b) are plotted for FI model with $R = 0$ (solid line) and MI model with $R = 0.48$ (dashed line). Figure 3.8(c) illustrates $c_e/\|c_e\|_\infty$ versus ξ for $k = 30$ and $t = 1$. The c_e profile produced by the MI model (dashed line) for $R = 0.48$ is identical to that of the FI model (solid line) for $R = 0$ except for a small narrow region across $z = 0$. Figure 3.8(d) illustrates the corresponding normalized w_e for $k = 30$ and $t = 1$. The w_e profiles are similar for $\xi > 0$. The FI domain (solid line) does not exist when $\xi < 0$. When $w_e < 0$ as for the MI model (dashed line), the region associated with it becomes stabilizing, see term $w_e \partial c_b / \partial z$ in equations (3.9)–(3.10). This region does not contribute to perturbation growth.

To further illustrate the above argument, figure 3.9(a) shows the base-state, c_b^M (solid line), least stable c_e (dashed line), and w_e (dash-dotted line), for $k = k_c$, $t = t_c$ when $R = 0$ in the MI model. The vertical line represents the location of the peak density, $\xi = 0.21$ or $z = \gamma$. The perturbations, c_e and w_e , are concentrated in the destabilizing zone where $w_e > 0$. Due to momentum transport, the point (solid dot) where velocity changes sign from a negative to a positive value does not coincide with the location of zero gradient of density, $\xi = 0.21$. Figure 3.9(b) depicts the normalized w_e profiles for $k = 15$, $t = 1$ and log mobility ratios, $R = 0$ (solid line), $R = 1$ (dashed line), and $R = 2$ (dash-dotted line). With increasing R ,

there is less momentum transport across the location of peak density at $\xi = 0.21$. Consequently, the solid dots move to the right, indicating a decrease in the width of the boundary layer corresponding with lesser instability, as shown in figure 3.7(c).

The following explains why the MI model is more unstable at small R and less unstable at large R , as seen in figure 3.7(c). Unlike the FI model, it is found that for the MI model, momentum transports across the region linking the zones of stable and unstable density gradients at $z = \gamma$ or $\xi = 0.21$. FI model offers no such mechanism. The magnitude of momentum transport in the MI model is proportional to the strength of the w_e fields within the boundary layer. Consequently, the width of the unstable portion of the boundary layer depend on R . The MI model is more unstable than the FI model when the width of the unstable region is large enough to produce stronger instabilities than an FI model. With increasing R , the width of the destabilizing zone becomes narrower, producing weaker instabilities compared to the FI model.

3.3.3 Effect of non-monotonic density profiles

The features of the non-monotonic density profile are varied in order to investigate its effect on the results produced by the MI model. The density profile used in §3.3.2 is referred to as ρ_A . To investigate how varying the location of the maximum density may affect the onset times, this study uses two additional profiles, ρ_B and ρ_C , by modifying the function $F(c)$, see equation (3.1). Figure 3.10(a) illustrates the function $F(c)$ for density profiles, ρ_A (circles), ρ_B (crosses), and ρ_C (squares).

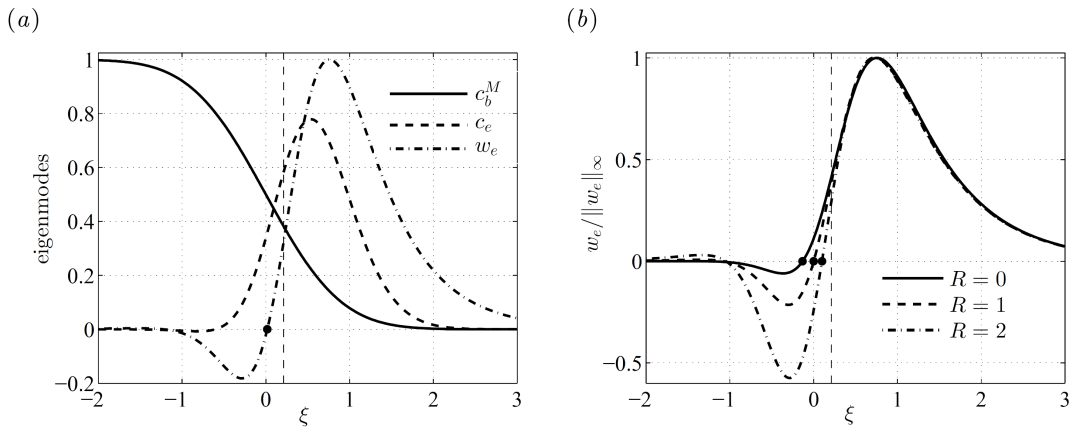


Figure 3.9: Eigenmodes associated with the MI model (a) Base-state, c_b^M (solid line), least stable c_e (dashed line), and w_e (dash-dotted line) at critical point (k_c, t_c) when $R = 0$. The vertical line is drawn at the location of maximum (turning point) in the density profile. (b) Normalized w_e profiles at $k = 15$ and $t = 1$ for log mobility ratios, $R = 0$ (solid line), $R = 1$ (dashed line), and $R = 2$ (dash-dotted line). The dots emphasise the points where $w_e = 0$.

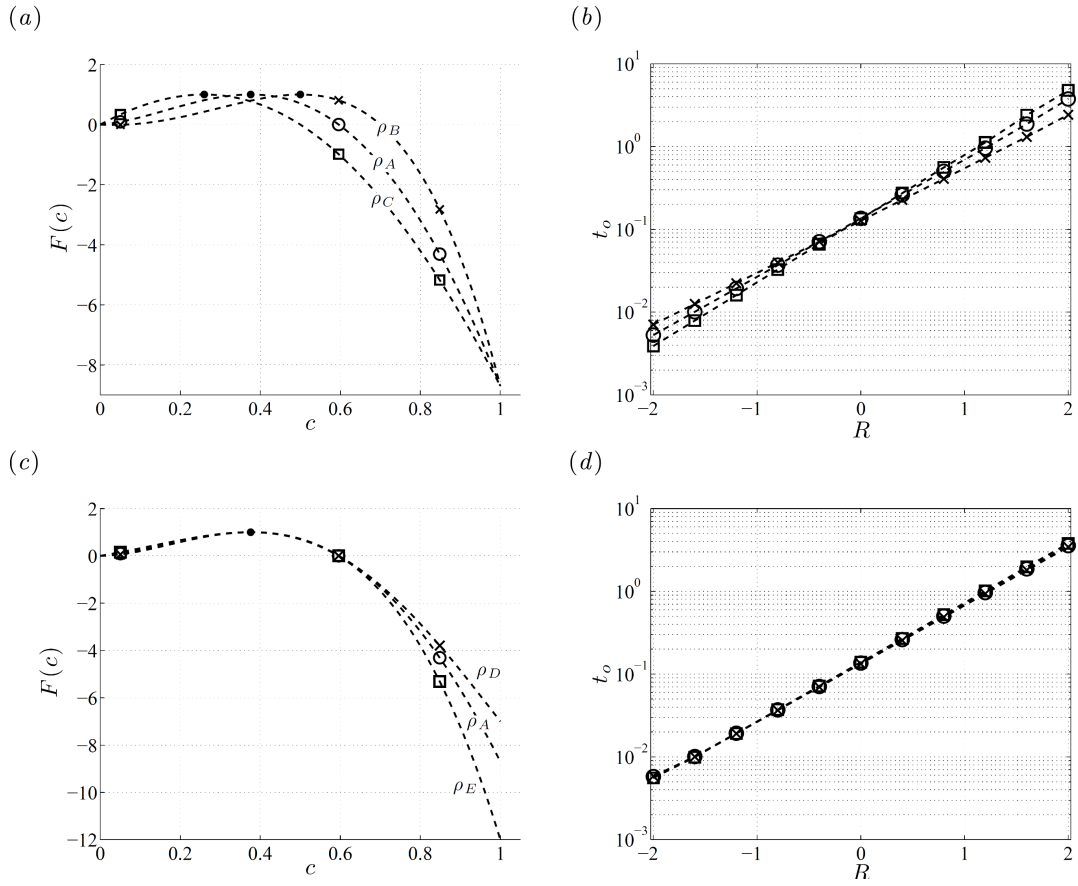


Figure 3.10: Five different non-monotonic density profiles in the MI model. (a)–(b) Effect of changing the location of the maximum value of density. (c)–(d) Effect of changing the density values of the saturated fluid, $c = 1$.

The maximum value of density for the ρ_A profile occurs at $c = 0.38$, while it is at $c = 0.5$ for ρ_B and at $c = 0.25$ for ρ_C . As peak value of density moves closer to $c = 1$, the width of the zone of unstable density gradients increases but the magnitude of positive density gradients decreases.

Figure 3.10(b) illustrates the onset time, t_c , versus log mobility ratio, R , obtained using the MI model with density profiles, ρ_A (circles), ρ_B (crosses), and ρ_C (squares). The onset times produced by the three density profiles increase with increasing R . When $R = -2$, the onset time, t_c , produced by ρ_B is 1.8 times greater than those produced by ρ_C . This suggests that the onset times obtained using ρ_B are closer to those predicted by FI model compared to other density profiles. For $R \approx -0.2$, three density profiles produce nearly equal t_c . With increasing R , the ρ_C profile tends to produce the largest onset times, t_c .

Figure 3.10(c) illustrates $F(c)$ for peak density location at $c = 0.375$ (solid dot) and for different values of density at $c = 1$. Modifying the density values of the saturated fluid changes the slope of the negative density gradients. The density profile, ρ_E (squares), has larger gradients compared to ρ_A (circles) and ρ_D (crosses). Figure 3.10(d) illustrates the corresponding onset times as function of R . The onset times for the different profiles are identical.

The stability characteristics observed in figures 3.10(b) and 3.10(d) can be explained by examining the relative location of the velocity eigenmode, w_e , and the fluid viscosity. Figure 3.11(a) illustrates w_e versus ξ for $R = 0$, $k = 30$, $t = 1$, and density profiles, ρ_A (solid line), ρ_B (dashed line), ρ_C (dash-dotted line). The viscosity values are mentioned along the top axes in figure 3.11. The crosses

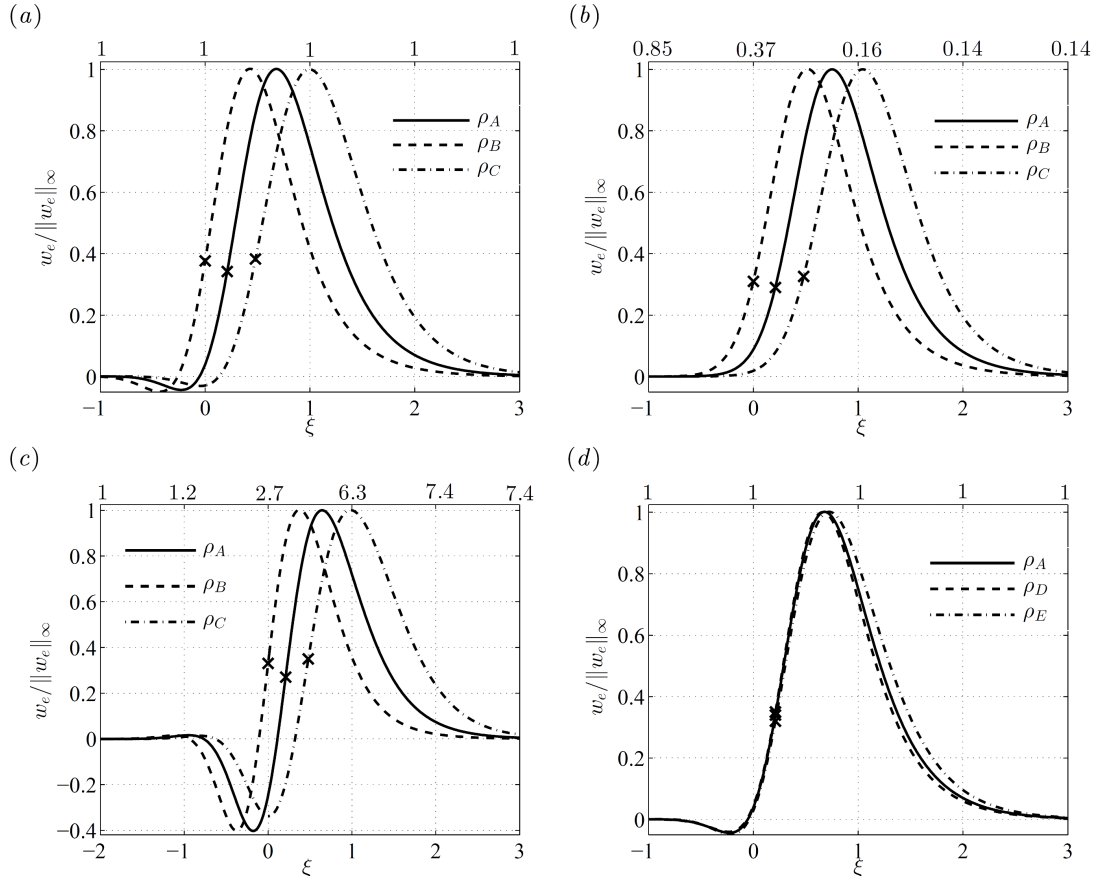


Figure 3.11: Effect of density profiles on velocity eigenmode w_e . The top axis represents viscosity at corresponding depthwise coordinate ξ . The location of the maximum density associated with each profile is marked with a cross. (a) $w_e/\|w_e\|_\infty$ vs. ξ for $R = 0$, $k = 30$, $t = 1$, and ρ_A (solid line), ρ_B (dashed line), ρ_C (dash-dotted line). (b) Same as in panel (a) for $R = -2$. (c) Same as in panel (a) for $R = 2$. (d) Same as in panel (a) for ρ_A (solid line), ρ_D (dashed line), ρ_E (dash-dotted line).

denote the location of maximum value of density. Perturbations are predominantly concentrated in regions to the right of the crosses where unstable density gradients exist. When maximum density occurs at $c = 0.5$ as in ρ_B , one observes that the peak of w_e shifts to the right in comparison to w_e related to ρ_A for which maximum density is at $c = 0.38$. When maximum density is at $c = 0.25$ as for ρ_C , the peak of w_e shifts to the left. The change in perturbation structures occurs due to the shifting of unstable regions within the boundary layer. Though the perturbations produced by ρ_A , ρ_B , and ρ_C peak at three different locations, the corresponding onset times for $R = 0$, shown in figure 3.10(b), are similar.

Let us now consider the effect of the spatial variation of viscosity within the boundary layer. Figure 3.11(a) is repeated for $R = -2$ in figure 3.11(b) and for $R = 2$ in figure 3.11(c) respectively. For $R = -2$, one finds that w_e fields remain shifted with respect to each other. Because viscosity decreases with depth when $R < 0$, the perturbations produced by ρ_C profiles are now located in lower viscous regions compared to perturbations produced by ρ_A or ρ_B . Consequently, perturbations produced by ρ_C have much earlier onset times compared to other profiles when $R < 0$, see figure 3.10(b). For $R = 2$, the perturbations produced by ρ_B profiles are located in lower viscosity regions, and therefore, have earlier onset times. Density profiles ρ_D and ρ_E have insignificant effects on perturbation structures, see w_e profiles in figure 3.11(d). The momentum transport across peak density locations has increased slightly when decreasing the magnitude of the negative density gradients. This is reflected in the upward movement of the crosses. However, these changes were small and did not affect the onset times for instability shown previously in

figure 3.10(*d*).

3.3.4 Effect of uniform flow

In previous sections, it is observed that gravitationally unstable boundary layers are less unstable for larger values of R . This behavior contrasts with classical displacement problems where instability increases with R . To explain this difference in behavior, this study considers a displaced interface model, which is an extension of the MI model where the lighter fluid is displaced by the heavier fluid with a uniform velocity, U , along the direction of gravity. For $U = 1$, the dimensional displacement velocity is equal to the buoyancy velocity of $K\Delta\rho g/\mu_1$, see §3.2 for details. To facilitate comparison with previous studies on displacement based instabilities (Manickam & Homsy, 1995), a linear density profile is first considered in addition to non-monotonic density profiles illustrated in figure 3.10(*a*).

Figure 3.12(*a*) illustrates onset times, t_c , versus log mobility ratio, R , for displacement velocities, $U = 0$ (circles), $U = 0.5$ (squares), and $U = 1$ (crosses), using a linear density profile. As expected, when $U = 0$, one observes that t_c increases with increasing R . For $U = 0.5$, t_c increases with R until it attains a maximum value at $R \approx 0$. Beyond this R , t_c decreases with R . When $U = 1$, similar behavior is observed with the maximum value of t_c occurring at $R = -1$. Figure 3.12(*b*) illustrates corresponding critical wavenumbers, k_c , versus R for $U = 0$ (circles), $U = 0.5$ (squares), and $U = 1$ (crosses). For $U = 0$, k_c monotonically decreases with R . For $U = 0.5$, k_c decreases with increasing R until it reaches a

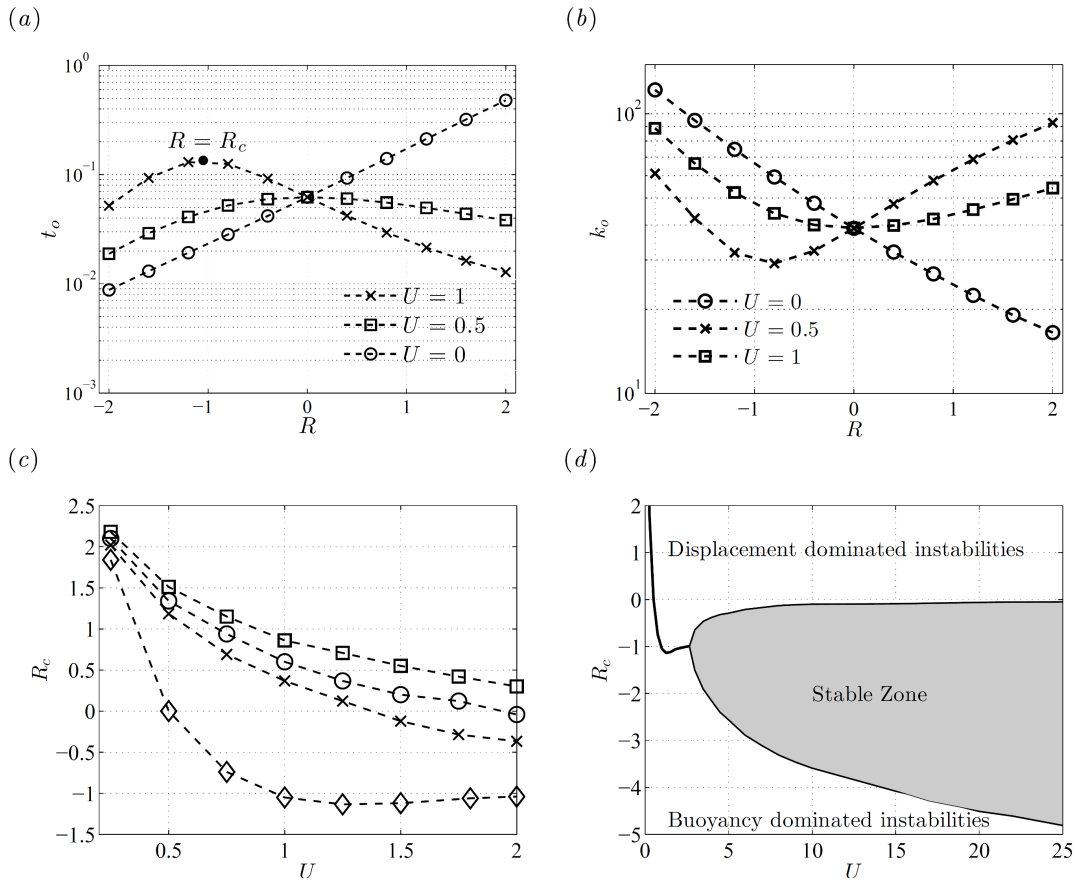


Figure 3.12: Effect of viscosity contrast on the displaced interface model. (a) Onset (critical) time t_c vs. log mobility ratio R , for $U = 0$ (circles), $U = 0.5$ (squares), and $U = 1$ (crosses). Solid dot marks R_c when $U = 1$. (b) Critical wavenumber k_c vs. R , for $U = 0$ (circles), $U = 0.5$ (squares), and $U = 1$ (crosses). (c) Critical viscosity ratio, R_c , vs. U for linear density profile (diamond), ρ_A (circles), ρ_B (crosses), ρ_C (squares). (d) R_c vs U for a linear density profile. The shaded region represents the space of R_c and U for which no instabilities are formed.

minimum at $R = 0$ and increases afterwards. For $U = 1$, the minimum point is located at a lower value of R . Similar qualitative trends were also observed for t_c and k_c produced by non-monotonic density profiles.

Figures 3.12(a) and 3.12(b) depict the existence of qualitatively different stability behaviors for the critical parameters, t_c and k_c . The value of R at which the instability characteristics of t_c changes is referred to as the critical viscosity ratio, R_c . When $R < R_c$, t_c increases with increase in R . This feature is in sharp contrast with classical displacement behavior and is more in accordance with buoyancy instabilities demonstrated in previous sections. When $R > R_c$, t_c decreases with increase in R , depicting the dominance of displacement-related instabilities. It is also observed that the point of maximum t_c and minimum k_c do not coincide but are close to each other. This may be because of sensitivity issues regarding measurement of perturbation quantities during small times, $t < O(t_c)$. Tilton *et al.* (2013)

Figure 3.12(c) illustrates R_c versus U for density profiles, ρ_A (circles), ρ_B (crosses), ρ_C (squares), and a linear density profile (diamonds), for mean flow in the range, $0 < U < 2$. For any given density profile, when displacement velocity tends to zero, $U \rightarrow 0$, the critical log mobility ratio, R_c , approaches infinity, $R_c \rightarrow \infty$. With increasing U , R_c decreases. The rate at which R_c decreases is larger for a linear density profile followed by the density profiles, ρ_B , ρ_A and ρ_C respectively. This suggests that the decay rate is proportional to the width of the zone of positive density gradients within the boundary layer, see section 3.3.3. By increasing the displacement velocity beyond $U = 2$, R_c splits into two branches. This is depicted in figure 3.12(d) for a linear density profile. The split at $U \approx 2.7$ is due to the

| R | I_1 | I_2 | I_3 | $I_1 + I_2 + I_3$ | σ |
|-----|-------|-------|-------|-------------------|----------|
| -3 | 15.90 | -3.29 | -4.89 | 7.71 | 19.79 |
| -2 | 7.16 | -0.76 | -3.55 | 2.85 | 4.88 |
| -1 | 3.48 | -0.11 | -1.92 | 1.44 | 0.85 |
| 0 | 1.90 | 0.00 | 0.00 | 1.90 | 3.00 |
| 1 | 1.19 | -0.07 | 1.86 | 2.97 | 7.36 |
| 2 | 0.82 | -0.31 | 3.66 | 4.18 | 12.17 |
| 3 | 0.62 | -0.74 | 5.43 | 5.31 | 16.59 |

Table 3.2: Vorticity integral values and growth rates for $U = 1$, $k = 30$, $t = 0.2$ and $Ra = 500$.

formation of a stable region when U is larger than a certain critical value.

To gain a deeper insight into relevant physical mechanisms, the instantaneous perturbation vorticity field is defined as,

$$\Omega_e = \frac{k}{\mu(c_b)} c_e - \frac{R}{k} \frac{\partial c_b}{\partial z} \frac{\partial w_e}{\partial z} + kRU c_e. \quad (3.15)$$

Equation (3.15) is integrated to obtain a measure of the vorticity field given by,

$$I = \int \Omega_e dz = I_1 + I_2 + I_3, \quad (3.16)$$

where

$$I_1 = k \int \exp(-R(1 - c_b)) c_e dz, \quad I_2 = -\frac{R}{k} \int \frac{\partial c_b}{\partial z} \frac{\partial w_e}{\partial z} dz, \quad I_3 = kRU \int c_e dz. \quad (3.17)$$

Compared to equation (3.13) in §3.3, there is an extra component to the vorticity field, I_3 , that depends on the uniform flow, U . For $R > 0$, I_3 is positive and destabilizing, and vice-versa for $R < 0$. Uniform flow plays an insignificant role on the stability of the diffusive front when R tends to zero, $R \rightarrow 0$.

Table 3.2 illustrates the values of the vorticity integrals, I_1 , I_2 , and I_3 , and the growth rate, σ , using a linear density profile for $U = 1$, $k = 30$, and $t = 0.2$. The eigenmodes are normalized such that the maximum value of c_e is one. The smallest values of I and σ are observed when the log mobility ratio is close to its critical value, $R = -1$ ($R \approx R_c$). With increasing or decreasing R , the magnitude of I increases, and consequently, the growth rate σ . For smaller values of R , the major contribution to the vorticity comes from the buoyancy term I_1 . Though the uniform flow contribution, I_3 is stabilizing, it is not strong enough to overcome the density mechanisms. For larger values when $R > 0$, the term I_1 has small magnitudes, and therefore the major contribution to the vorticity comes from the flow term I_3 .

The vorticity integrals also explain the presence of the stable zone in figure 3.12(d). Within the stable zone where $R < 0$ and $U > 0$, the stabilizing effects of I_3 are stronger than destabilizing effects of buoyant term, I_1 . The stabilizing effect of U when $R < 0$ has also been previously reported by Manickam and Homsy.(Manickam & Homsy, 1995) Note that when fluids move against the direction of gravity, $U < 0$, the perturbation characteristics are similar to those of buoyancy dominated instabilities. This is because when $U < 0$, both I_1 and I_3 becomes increasingly destabilizing with decreasing R .

For non-monotonic density profiles, the strength of displacement dominated

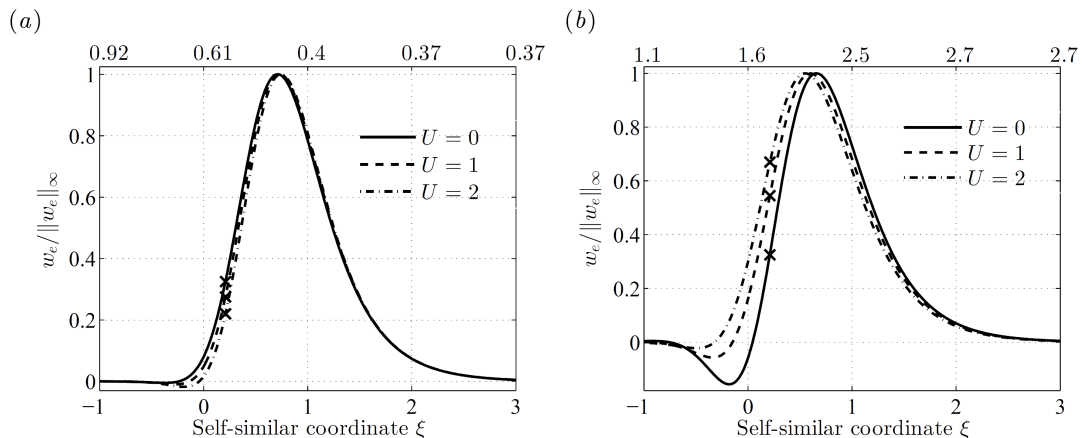


Figure 3.13: Effect of displacement velocity on the velocity eigenmode w_e . Viscosity values are mentioned at the top. The crosses denote the location of the maximum in the density profile, ρ_A . (a) $w_e/\|w_e\|_\infty$ vs. ξ for $R = -1$, $k = 30$, and $t = 1$. (b) Same as in panel (a) for $R = 1$.

instabilities would affect the momentum transport across the interface of zero density gradient. Figure 3.13(a) illustrates the normalized vertical velocity profiles, $w_e/\|w_e\|_\infty$, for $U = 0$ (solid line), $U = 1$ (dashed line), and $U = 2$ (dashed-dotted line) when $R = -1$, $k = 30$, and $t = 1$. The crosses correspond to the peak density location at $\xi = 0.21$ for ρ_A profile. With increasing values of U , the strength of the w_e fields associated with $R = -1$ decreases due to stabilizing effects of the uniform flow. Therefore, the momentum transport across $\xi = 0.21$ also decreases. On the other hand, $R > 0$ results in greater momentum transport. This is illustrated in figure 3.13(b) for $R = 1$. In this case the velocity perturbations increase in strength due to increased destabilizing effects of the uniform flow.

The critical R_c is also an excellent indicator of long term linear viscous characteristics for time, $t \gg t_c$, even though R_c was defined with respect to the onset

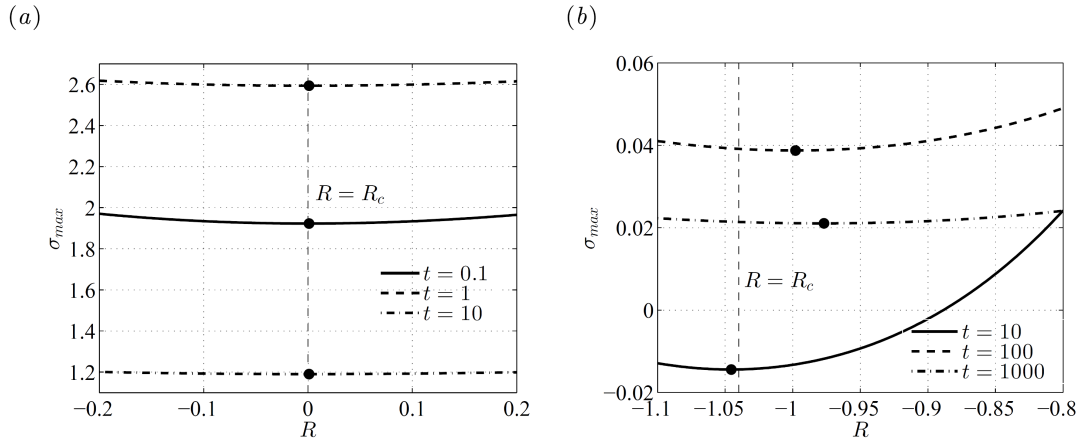


Figure 3.14: Long term linear stability characteristics, σ_{max} vs. R , using a linear density profile for (a) $U = 0.5$ (b) $U = 2$.

time of linear instability, t_c . To demonstrate this, figure 3.14(a) illustrates σ_{max} vs R for $U = 0.5$ using a linear density profile. The vertical dashed line represents $R = R_c$. The solid dots denote the points at which $\partial\sigma_{max}/\partial R = 0$. Across this minima, there is a reversal of instability characteristics associated with σ_{max} . At $t = 0.1$, σ_{max} has a nonmonotonic behavior with R with the local minima at $R = 0$. At $t = 1$ and $t = 10$, the local minima is still at $R = 0$. The viscosity ratio at which local minima occurs for late times are in excellent agreement with R_c . Figure 3.14(b) repeats figure 3.14(b) for $U = 2$. Large values of t were used because of smaller perturbation growth rates. The locations of local minima (solid dots) are within 10 percent of R_c even for late times, $t < 1000$.

3.4 Conclusions

This chapter examines the effect of viscosity contrast on the linear stability of gravitationally unstable, transient boundary layers. To interpret experimental observations, the current work considered two physical models that are characterized by the specific depth-wise concentration profiles and density-concentration relationships. If laboratory studies are carried out with fluids for which $R \approx 0$, our study indicates that the onset times of instability determined by the MI and FI models can differ by a factor of 3. For $R < 0$, the MI model becomes even more unstable and gives rise to much earlier onset times compared to the FI model. By adopting fluids with $R \approx 0.5$ for the MI model and $R = 0$ for the FI model, the MI and FI models produce similar linear stability characteristics. The exact value of R for MI model that provides the agreement would also depend on the specific profiles of density-concentration relationship. Previous works (Ennis-King *et al.*, 2003; Riaz *et al.*, 2006) demonstrate that the onset times scale proportionately to the Rayleigh number. Therefore, the ratio of the onset times for the fixed and moving interface models is not a function of the Rayleigh number.

Diffusive layers are more unstable in general when viscosity decreases with depth within the layer compared to when viscosity increases with depth. This behavior is in contrast to the classical understanding of gravitationally unstable, transient diffusive layers. For that case, greater instability is associated with the displacement of a more viscous fluid in the direction of gravity by a less viscous fluid. To place this behavior in context, it is shown how instability mechanisms

depend on the critical value of the log mobility ratio, R_c . When $R < R_c$, density gradients govern instability. When $R > R_c$, perturbations derive energy from the background flow. When the magnitude of displacement velocity that is scaled with buoyancy velocity exceeds a certain threshold value, R_c splits into two branches due to the formation of an intermediate stable zone. The mechanisms are explained in terms of the interaction of vorticity components related to gravitational and viscous effects.

Available data on the viscosity-concentration relationship for the CO₂-water system indicates some uncertainty with regards to whether the viscosity of the mixture would increase or decrease upon dissolution of CO₂. Different studies report both positive and negative values of R (Bando *et al.*, 2004; Kumagai & Yokoyama, 1998, 1999), though all studies report viscosity differences to be small, $|R| \approx O(0.1)$. Therefore it is determined that viscosity contrast would not substantially alter the stability results based on the $R = 0$ case for practical problems. However, the viscosity contrast between the solution and the solvent for the fluids employed by experimental studies is large. For example, the experimental study of Backhaus *et al.* (2011) was based on the moving interface model where the viscosity contrast was about $R \approx -3$. This implies a much greater level of instability compared with the case of $R \approx 0$. For the experimental study of Slim *et al.* (2013) based on the fixed interface model, on the other hand, $R \approx 0.04$, which is closer to what is expected in practice. However, it is uncertain whether the model employed in that study exactly corresponds to either the fixed or the moving interface models. This is because the authors observed bubbles at the top boundary for certain experimental

runs. This may suggest that the presence of small velocity perturbations at the top boundary. Such FI models usually have much smaller onset time of instabilities compared to standard FI models (Elenius *et al.*, 2012). In general, modeling and theoretical studies based on the assumption of $R = 0$ cannot be used directly to interpret results from experimental observations of systems with a large viscosity contrast. Stability analysis for such systems need to account for these differences.

Most experimental studies report the time for the onset of nonlinear convection. Fully resolved nonlinear simulations (Farajzadeh *et al.*, 2013; Rapaka *et al.*, 2008; Tilton & Riaz, 2014) demonstrate that the time for the onset of nonlinear effects depends on amplitude of initial perturbations and Ra , and is usually much greater than t_o . Our conclusions with regards to differences in the level of instability depending on the viscosity contrast and different models are expected to have a proportionate effect on the onset of convection.

Chapter 4: Natural convection in horizontally layered porous media

4.1 Overview

This chapter explores the onset of natural convection in horizontally layered aquifers where permeability varies in the direction of gravity. Natural convection associated with CO₂ sequestration in deep saline aquifers occurs due to the unstable density stratification of diffusive boundary layers. The density-driven instability plays a key role in the rapid dissolution of CO₂ into brine (Orr, 2009). The primary objective of this chapter is to develop a basic understanding of the instability mechanisms that govern the interaction of perturbations with permeability heterogeneity. Permeability is assumed to vary periodically across the thickness of the aquifer. Such a variation of permeability is relevant for saline aquifers (Bickle *et al.*, 2007; Chadwick *et al.*, 2005; Green & Ennis-King, 2010; Neufeld & Huppert, 2009) and is used to identify the general mechanisms of instability in heterogeneous porous media. The periodic variation of permeability may also facilitate comparison with the classical Rayleigh-Bénard convection in layered and periodic permeability porous media (Gjerde & Tyvand, 1984; Hewitt *et al.*, 2014; McKibbin & O’Sullivan, 1980, 1981; Nield & Bejan, 2006).

Previous studies of miscible flows in heterogeneous porous media highlight the

importance of the interactions between fluid flow and permeability heterogeneity. These studies relate to displacement processes for oil recovery (Christie *et al.*, 1993; Tchelepi *et al.*, 1993; Zhang *et al.*, 1997), the flow of a contaminant jet into an aquifer (Schincariol, 1998; Schincariol *et al.*, 1997) and the problem of natural convection due to a gravitationally unstable boundary layer (Prasad & Simmons, 2003; Rapaka *et al.*, 2009; Simmons *et al.*, 2001). The presence of correlated variability of permeability leads to complex regimes. As the variance level and the correlation length of heterogeneity increase, the details of the permeability field dictate the flow paths. (Camhi *et al.*, 2000; Chen & Meiburg, 1998; Tan & Homsy, 1992; Tchelepi & Orr, 1994). A resonant amplification of instability was reported by DeWit & Homsy (1997) and Riaz & Meiburg (2004) when the length scale of the viscous instability is close to the correlation scale of the permeability variation.

The onset of natural convection depends on the growth rate of perturbation amplitude within the linear regime. For the problem of CO₂ sequestration, the transient nature of the diffusive boundary layer imparts an evolutionary character to the amplitude that depends on the instantaneous coupling between perturbations and the boundary layer. In the presence of heterogeneity, the coupling involves additional terms related to the permeability field, the effect of which has not been investigated for the onset of convection in the past. This study examines such effects using a combination of linear stability analysis and direct numerical simulations.

The chapter is organized as follows. The governing equations and the permeability model are described in §4.2. The critical times for the onset of instability and the physical justification are presented in §4.3. The onset of nonlinear convection is

explained in §4.4. Finally, a summary of our findings are presented in §4.5.

4.2 Governing equations

The mathematical model governing the flow of dissolved CO₂ in a porous saline aquifer can be expressed in dimensionless form as

$$\nabla \cdot \mathbf{u} = 0, \quad c_t = -\mathbf{u} \cdot \nabla c + \frac{1}{Ra} \nabla^2 c, \quad \mathbf{u} = -k(\nabla p - c\hat{\mathbf{z}}), \quad (4.1)$$

where, $\mathbf{u}(\mathbf{x}, t)$ is the Darcy velocity, $c(\mathbf{x}, t)$ is the concentration, $p(\mathbf{x}, t)$ the pressure. In equation (4.1), Ra and $k(z)$ are dimensionless quantities corresponding to the Rayleigh number and permeability field. The unit vector, $\hat{\mathbf{z}}$, acts in the direction of gravity. The initial condition is the quiescent state, $\mathbf{u} = 0$. Periodic boundary conditions are imposed on the vertical boundaries. The boundary conditions on the horizontal boundaries are,

$$c|_{z=0} = 1, \quad c_z|_{z=1} = 0, \quad w|_{z=0} = w|_{z=1} = 0. \quad (4.2)$$

Equation (4.1) was non-dimensionalized as in Riaz *et al.* (2006) with the following characteristic values for length, time, velocity, and pressure,

$$L = H, \quad T = \frac{\phi\mu H}{\bar{k}\Delta\rho g}, \quad U = \frac{\bar{k}\Delta\rho g}{\mu}, \quad P = \frac{\mu U H}{\bar{k}}, \quad (4.3)$$

where \bar{k} is a characteristic value of permeability, ϕ is the porosity, D is the diffusion coefficient, and H the thickness of the aquifer. Concentration is scaled with respect to its maximum value found at $z = 0$. The Rayleigh number is defined as $Ra = UH/(\phi D)$. The driving mechanism of density difference is represented by, $\Delta\rho =$

$\rho_1 - \rho_o$, where ρ_o and ρ_1 refer, respectively, to the density of pure brine and CO₂ saturated brine. The difference in density compared with the density of brine is small, $\Delta\rho/\rho_o \sim \Delta\rho/\rho_1 \ll 1$. This justifies the use of the Boussinesq approximation and a linear density profile, $\rho = \rho_o + \Delta\rho c$, for obtaining (4.1). Viscosity, μ , is assumed to be a constant (Bando *et al.*, 2004; Fleury & Deschamps, 2008). The dimensionless permeability field is assumed to vary periodically in the vertical direction according to

$$k(z) = \exp \left[\sqrt{2\sigma^2} \cos(mz + \gamma) \right] . \quad (4.4)$$

The term, $\sqrt{2\sigma^2}$, indicates the amplitude of the spatial permeability oscillation, where σ^2 is the variance of $\ln(k)$. The wavelength of permeability oscillation is m , and γ indicates the phase with respect to $z = 0$. The cosine permeability variation allows the spatial distribution to be smooth with a constant wavelength, $2\pi/m$. When $k(z)$ is normalized according to $\int_0^1 k(z) dz = 1$, as in this work, \bar{k} corresponds to the average of the permeability field. The permeability model given by (4.4) includes the essential features of the spatial correlation of the permeability field and its variance (Delhomme, 1979; Freeze, 1975). The variance associated with the spatial distribution of the natural logarithm of the permeability field has been reported to be within the range, 0.5 to 5 (Clifton & Neuman, 1982), while the spatial correlation scales are often observed to be large horizontally and much smaller vertically (Dagan, 1984), indicating a layered permeability structure. Porosity variation is not considered in this study because it is generally much less than the permeability variation (Hoeksema & Kitanidis, 1985).

A linear stability analysis is used to identify the structure and growth of finite amplitude perturbations that lead to the onset of nonlinear effects. To perform a linear stability analysis, perturbations are imposed in the form of vertical shape functions that vary periodically in the x and y directions,

$$(\mathbf{u}, p, c)(\mathbf{x}, t) = c^o(z, t) + (\tilde{\mathbf{u}}, \tilde{p}, \tilde{c})(z, t) \exp [i(\ell_x x + \ell_y y)] , \quad (4.5)$$

where c^o is the concentration base state and $\tilde{\mathbf{u}}, \tilde{p}$ and \tilde{c} denote the perturbation profiles in the z -direction. Perturbation wavenumbers in the x - and y -direction are denoted by ℓ_x and ℓ_y , respectively, and $i = \sqrt{-1}$.

The base state, $c^o(z, t)$, is the solution of the diffusion equation, $c_t = c_{zz}/Ra$, that follows from the initial condition, $\mathbf{u} = 0$, and the concentration boundary conditions, (4.2). This time varying base state represents a diffusive boundary layer that originates at $z = 0$ and diffuses downwards. By substituting (4.5) into (4.1), eliminating pressure and collecting linear terms, the following system for perturbations, \tilde{c} and \tilde{w} , are obtained,

$$\tilde{c}_t - \frac{1}{Ra} (\tilde{c}_{zz} - \ell^2 \tilde{c}) = -c_z^o \tilde{w} , \quad (4.6)$$

$$\tilde{w}_{zz} - (\ln k)_z \tilde{w}_z - \ell^2 \tilde{w} = -k \ell^2 \tilde{c} , \quad (4.7)$$

where, $\ell = \sqrt{\ell_x^2 + \ell_y^2}$. The boundary conditions are

$$\tilde{c}|_{z=0} = \tilde{c}_z|_{z=1} = \tilde{w}|_{z=0} = \tilde{w}|_{z=1} = 0 . \quad (4.8)$$

The above set of equations represents a linear initial value problem (IVP) with respect to the perturbations, \tilde{c} and \tilde{w} . The IVP can be expressed more compactly

as

$$\frac{\partial \tilde{c}}{\partial t} = \mathcal{A}(t; \ell) \tilde{c} \quad , \quad \tilde{c}(z, t_o) = \tilde{c}_o(z) \quad ; \quad z \in \{0, 1\} \quad , \quad (4.9)$$

where t_o is the time at which perturbations are introduced and $\mathcal{A}(t; \ell)$ is the linear operator that results from the elimination of \tilde{w} between (4.6) and (4.7). The IVP can be marched in time to determine the evolution of the initial condition, $\tilde{c}_o(z)$.

As in chapter 3, the IVP (4.9) is studied by spectrally transforming the underlying operator \mathcal{A} . Using the transformation, $\xi = z\alpha$ and $\hat{t} = t$, where $\alpha = \sqrt{Ra/4t}$ and $\xi \in \{0, \infty\}$, equations (4.6) and (4.7) are expressed in (ξ, t) -space which gives the new IVP

$$\frac{\partial \tilde{c}}{\partial t} = \mathcal{B}(t; \ell) \tilde{c} \quad , \quad \tilde{c}(\xi, t_o) = \tilde{c}_o(\xi) \quad ; \quad \xi \in \{0, \infty\} \quad . \quad (4.10)$$

The base state in (ξ, t) -space is self-similar, $c^o = \text{erfc}(\xi)$, where erfc is the complementary error function. Homogeneous Dirichlet boundary conditions are employed for both \tilde{c} and \tilde{w} . The IVP in (ξ, t) -space, (4.10), is equivalent to the IVP in (z, t) -space, (4.9), provided $\alpha > 3$. When $\alpha > 3$, the two initial value problems, (4.9) and (4.10), produce identical results.

4.3 Linear perturbation growth

This section explores the effect of permeability on the onset of linear instability. The onset of instability is defined as the time at which the perturbation growth rate first becomes positive, $\omega > 0$. The critical time for the onset of instability is defined as the minimum onset time of instability over all perturbation wavenumbers. A

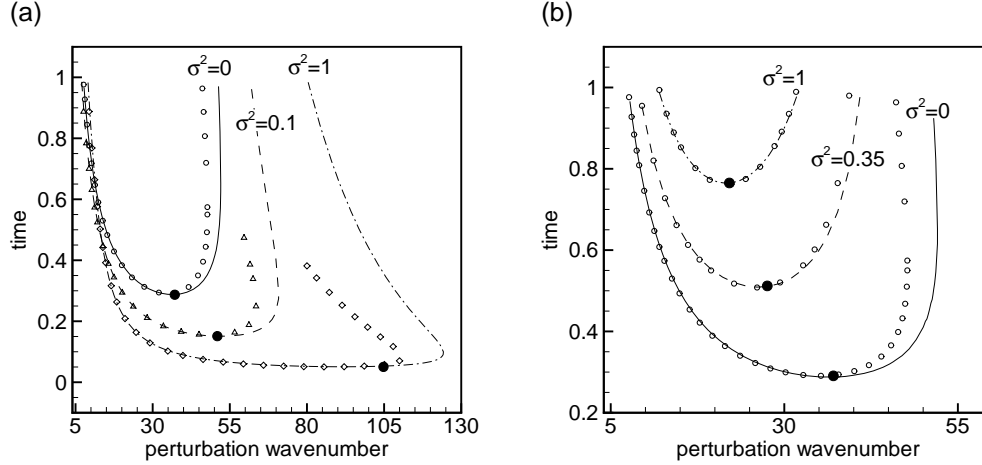


Figure 4.1: Marginal stability curves for $Ra = 500$ and $m = 6\pi$, based on ω_∞ (lines) and ω_{DMA} (open symbols). (a) $\gamma = 0$ and (b) $\gamma = \pi$. Critical conditions for the onset of instability, (t_c, ℓ_c) , are indicated by solid dots. Increasing the variance for $\gamma = 0$ results in greater instability, shifting the onset of instability to earlier times and larger wavenumbers. For the case of $\gamma = \pi$, an increase in variance has the opposite effect.

marginal state of stability corresponds to $\omega = 0$. The parameters of interest are the permeability variance, σ^2 , phase, γ , the permeability wavenumber, m , in addition to the perturbation wavenumber, ℓ , and time, t . The analysis is conducted for a constant $Ra = 500$. Results for different Ra are related through simple scaling relationships.

4.3.1 Influence of permeability variance and phase

The effect of permeability variance and phase on the marginal stability curve is shown in figure 4.1 for $Ra = 500$ and $m = 6\pi$. Two different values of the phase, $\gamma = 0$ and $\gamma = \pi$, are shown in plots (a) and (b), respectively. The marginal stability curve, for which $\omega = 0$, maps the boundaries of the stable (negative growth rate)

and unstable (positive growth rate) regions in the t - ℓ plane. The lowest point on the curve, highlighted with a dot, indicates the critical conditions, (t_c, ℓ_c) , for the onset of instability, i.e., the earliest time, t_c , at which the critical wavenumber, ℓ_c , becomes unstable. The critical time is greater than zero because perturbations are initially damped. The marginal stability curves also show the longwave cutoff, indicating that wavenumbers smaller than a critical value are damped.

The marginal stability curves based on the growth rate, ω_∞ , the maximum eigenvalue of \mathcal{B} , are indicated with lines in figure 4.1. Symbols represent the growth rate, ω_{DMA} , obtained with the dominant mode analysis (DMA) of Riaz et al. (2006), namely,

$$\omega_{\text{DMA}} = -\frac{1}{4t} (4 + \beta^2) + \frac{1}{a(t)\sqrt{\pi t}} \int_0^\infty \exp(-\xi^2) \tilde{w} d\xi, \quad (4.11)$$

where, $\beta = \ell/\alpha$, $\alpha = \sqrt{Ra/4t}$ and $a(t)$ is the coefficient in the expansion, $\tilde{c}(\xi, t) = a(t)\xi e^{-\xi^2}$. For problems with homogeneous permeability, when $\sigma^2 = 0$, an analytical solution for \tilde{w} can be used to obtain the following relation,

$$\omega_{\text{DMA}} = -\frac{1}{4t} (4 + \beta^2) + \frac{1}{16} \sqrt{\frac{\pi}{t}} \beta^2 e^{\beta^2/2} \left[1 - \operatorname{erf} \left(\frac{\beta}{2} \right) \right]^2. \quad (4.12)$$

For heterogeneous cases, where $\sigma^2 > 0$, \tilde{w} can only be determined numerically. The integration in (4.11) is then carried out numerically to determine ω_{DMA} . The results based on ω_{DMA} are plotted to demonstrate the validity of DMA for the heterogeneous case. Figure 4.1(a) shows that the marginal stability curves based on ω_{DMA} and ω_∞ agree very well for wavenumbers up to the critical wavenumber. Note that the time required for calculating critical conditions using DMA is at least an order of magnitude smaller than other methods.

Figure 4.1(a) shows that when $\gamma = 0$, larger values of permeability variance, σ^2 , lead to greater instability, i.e., smaller critical times, t_c , larger critical wavenumbers, ℓ_c , and a larger spectrum of unstable wavenumbers. Figure 4.1(b) indicates that the effect of variance is reversed when $\gamma = \pi$. The critical time, t_c , shifts to larger values with increasing variance while the critical wavenumber, k_c , decreases. The entire spectrum of unstable wavenumbers also shrinks.

4.3.2 Stability mechanisms

A physical understanding of the effect of heterogeneity can be gained by considering the vorticity, $\nabla \times \mathbf{u}$, which is obtained from (4.1) as

$$\nabla \times \mathbf{u} = k\nabla c \times \hat{\mathbf{z}} + \nabla \ln k \times \mathbf{u} . \quad (4.13)$$

The two terms on the right hand side of (4.13) indicate that vorticity is produced or diminished by the interaction of two effects. The first term is related to the misalignment of the concentration gradient with the direction of the gravity vector, $\hat{\mathbf{z}}$. The second term is associated with the misalignment of the velocity field with the gradient of $\ln k$. For the homogeneous case, $\sigma^2 = 0$, only the first term is active. For $\sigma^2 > 0$, both terms contribute to either amplify or diminish vorticity. Note that the vorticity production due to variable viscosity is given by $R\nabla c \times \mathbf{u}$, where R is the log mobility ratio (see Chapter 3). Although this term is similar to vorticity production by permeability gradients (equation 4.13), the physical effect should be different because of the transient nature of the concentration field as opposed to the fixed spatial variation of permeability.

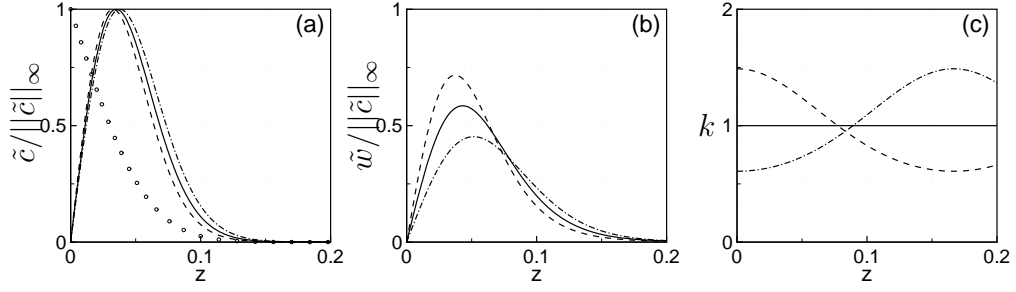


Figure 4.2: Perturbation and permeability profiles for $\ell = 40$, $m = 6\pi$ and $t = 0.5$. Lines represent, $\sigma^2 = 0$ (solid), $\sigma^2 = 0.1, \gamma = 0$ (dashed) and $\sigma^2 = 0.1, \gamma = \pi$ (dash-dot). The base state, c^o , is plotted in (a) with symbols. It indicates that perturbations rapidly decay to zero outside the boundary layer.

To interpret vorticity in the linear regime for a 2-D disturbance field, this study considers the y -component of vorticity, $\eta(x, z, t) = i\tilde{\eta}(z, t) \exp(i\ell x)$, which can be expressed as

$$\tilde{\eta} = \ell k \tilde{c} - \frac{1}{\ell} (\ln k)' \tilde{w}_z . \quad (4.14)$$

The vorticity, $\tilde{\eta}$, reflects the net effect of the coupling between perturbation and permeability profiles. The amplitude of perturbations, \tilde{c} and \tilde{w} , is governed by the history of perturbation growth. In order to focus on the effect of the instantaneous coupling between perturbation and permeability profiles, the concentration perturbation, \tilde{c} , in (4.14) will be scaled with $\|\tilde{c}\|_\infty$. The velocity perturbation, \tilde{w} , then also scales with $\|\tilde{c}\|_\infty$ because the governing equations (4.6) and (4.7) are linear and do not contain the time derivative of \tilde{w} . Note that the resulting instantaneous value of $\tilde{\eta}/\|\tilde{c}\|_\infty$ is useful for comparing the effect of different permeability profiles for a fixed value of ℓ . Note that this approach is independent of the specific scale, $\|\tilde{c}\|_p$,

for \tilde{c} and \tilde{w} . Our interpretation and conclusions do not change when perturbations are scaled with either $\|\tilde{c}\|_1$ or $\|\tilde{c}\|_2$.

The spatial profiles for $\tilde{c}/\|\tilde{c}\|_\infty$, $\tilde{w}/\|\tilde{c}\|_\infty$ and k for $Ra = 500$, are plotted in figure 4.2 for $\ell = 40$, $m = 6\pi$ and $t = 0.5$. Perturbation profiles shown are based on the initial condition (2.44). The base state, c^o , is also plotted in figure 4.2(a) to indicate that \tilde{c} and \tilde{w} decay rapidly to zero outside the boundary layer. Figure 4.2(a) shows that the profiles for $\tilde{c}/\|\tilde{c}\|_\infty$ do not change appreciably when heterogeneity is introduced. Therefore, the differences in the corresponding velocity perturbations, $\tilde{w}/\|\tilde{c}\|_\infty$, plotted in figure 4.2(b), are mainly due to the differences in the corresponding permeability profiles, shown in figures 4.2(c). Figure 4.2(b) shows that compared with the homogeneous case, the amplitude of $\tilde{w}/\|\tilde{c}\|_\infty$ increases for $\gamma = 0$ but decreases when $\gamma = \pi$. This behavior can be explained with the help of (4.7) where k appears as a source term and sets the amplitude of \tilde{w} .

The perturbation-permeability interactions are shown in figure 4.3 with the help of,

$$\hat{\eta}_c = \ell k \tilde{c} / \|\tilde{c}\|_\infty, \quad \hat{\eta}_w = \tilde{w}_z (\ln k)' / \ell \|\tilde{c}\|_\infty, \quad \text{and} \quad \hat{\eta} = \hat{\eta}_c - \hat{\eta}_w, \quad (4.15)$$

for $Ra = 500$, $\ell = 40$, $m = 6\pi$ and $t = 0.5$. Figure 4.3(a) shows that $\hat{\eta}_c$ increases with an increase in the variance for $\gamma = 0$. This is because larger values of k coincide with the peak of $\tilde{c}/\|\tilde{c}\|_\infty$ when σ^2 is increased, as shown in figures 4.2(a,c). Conversely, $\hat{\eta}_c$ decreases with an increase in σ^2 when $\gamma = \pi$, as shown in figure 4.3(d). This is because smaller values of k coincide with the peak of $\tilde{c}/\|\tilde{c}\|_\infty$ with an increase in σ^2 , as shown in figures 4.2(a,c). The profiles of $\hat{\eta}_w$, shown in figures 4.3(b,d), are much

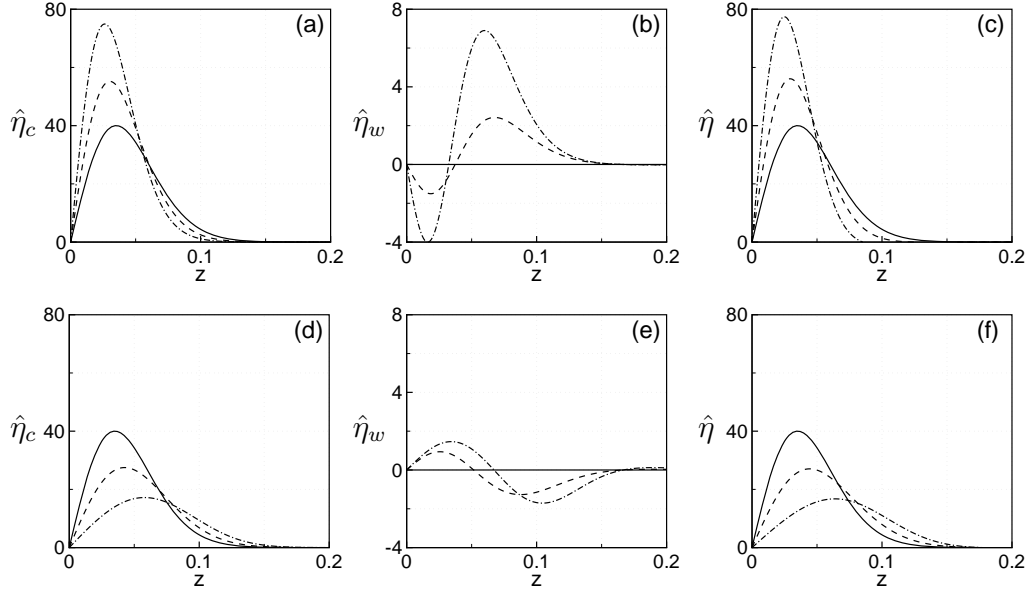


Figure 4.3: Spatial variation of vorticity contributions and net vorticity, $\hat{\eta}_c$, $\hat{\eta}_w$ and $\hat{\eta}$, defined in (4.15), for $\ell = 40$, $m = 6\pi$ and $t = 0.5$. Lines represent, $\sigma^2 = 0$ (solid), $\sigma^2 = 0.1$ (dashed) and $\sigma^2 = 0.5$ (dash-dot). The two cases, $\gamma = 0$ and $\gamma = \pi$ are shown, respectively, in plots (a,b,c) and (d,e,f).

smaller in magnitude compared with $\hat{\eta}_c$. The primary contribution to $\hat{\eta}$ therefore comes from $\hat{\eta}_c$.

To sum up the spatial variation of vorticity production, the net vorticity is defined as

$$\int_0^1 \hat{\eta} dz = \ell \int_0^1 k \tilde{c} / \|\tilde{c}\|_\infty dz - \frac{1}{\ell} \int_0^1 \tilde{w}_z (\ln k)' / \|\tilde{c}\|_\infty dz . \quad (4.16)$$

The first term on the right hand side of (4.16), \mathcal{I}_c , is positive because \tilde{c} and k are both positive, as shown in figures 4.2(a,c). The second term on the right hand side of (4.16), \mathcal{I}_w , shown in figures 4.3(b,e), depends in a more complicated manner on the coupling between the spatial variations of $(\ln k)'$ and \tilde{w}_z . The values of \mathcal{I}_c , \mathcal{I}_w

| $\gamma = 0$ | | | | | $\gamma = \pi$ | | | | |
|--------------|-----------------|-----------------|---------------|-----------------|----------------|-----------------|-----------------|---------------|-----------------|
| σ^2 | \mathcal{I}_c | \mathcal{I}_w | \mathcal{I} | ω_∞ | σ^2 | \mathcal{I}_c | \mathcal{I}_w | \mathcal{I} | ω_∞ |
| 0 | 2.397 | 0.000 | 2.396 | 1.052 | 0 | 2.397 | 0.000 | 2.396 | 1.052 |
| 0.1 | 2.876 | 0.095 | 2.778 | 2.838 | 0.1 | 1.933 | -0.042 | 1.975 | -0.705 |
| 0.5 | 3.393 | 0.263 | 3.129 | 4.571 | 0.5 | 1.451 | -0.026 | 1.477 | -2.509 |
| 1.0 | 3.692 | 0.402 | 3.290 | 5.427 | 1.0 | 1.166 | 0.013 | 1.152 | -3.460 |

Table 4.1: Net vorticity contributions, \mathcal{I}_c , \mathcal{I}_w and \mathcal{I} , as a function of σ^2 for $\ell = 40$, $m = 6\pi$ and $t = 0.5$. The corresponding growth rates, ω_∞ , indicate that larger positive values of \mathcal{I} are associated with greater instability. Net vorticity, \mathcal{I} , is determined primarily by \mathcal{I}_c for this parameter set because $\mathcal{I}_c/|\mathcal{I}_w| \gg 1$.

and \mathcal{I} (the left hand side of equation 4.16) can be found in Table 4.1 for $Ra = 500$, $\ell = 40$, $m = 6\pi$ and $t = 0.5$. Table 4.1 indicates that \mathcal{I} increases with an increase in the variance when $\gamma = 0$ and decreases with an increase in the variance when $\gamma = \pi$. Corresponding values of the growth rate listed in Table 4.1 indicate that larger values of \mathcal{I} are associated with greater instability and smaller values with less instability. Table 4.1 further indicates that \mathcal{I}_c is an order of magnitude greater than $|\mathcal{I}_w|$ and therefore sets the magnitude of \mathcal{I} . Hence, with an increase in σ^2 the increase in \mathcal{I} for $\gamma = 0$ and the decrease in \mathcal{I} for $\gamma = \pi$ is related, respectively, to larger and smaller values of k in the boundary layer, as shown in figure 4.2(c). Permeability gradients play a relatively minor role for the parameter set considered in figure 4.1.

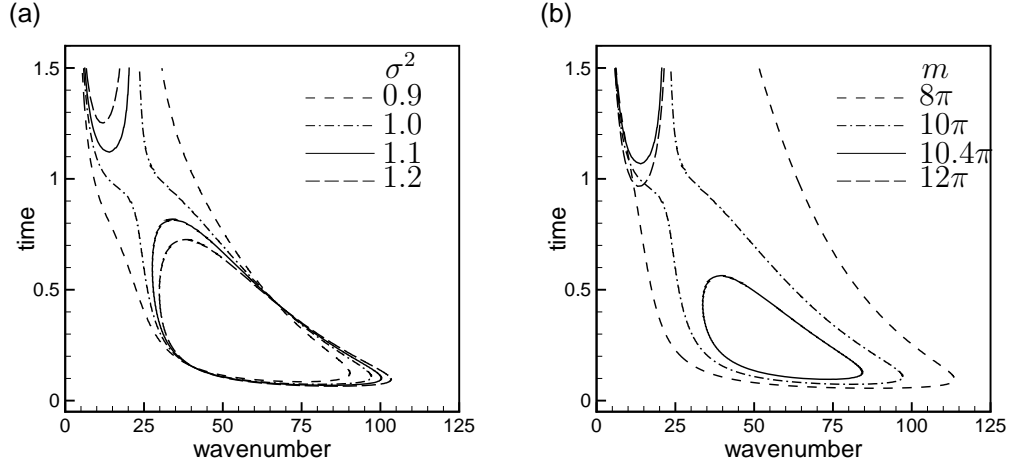


Figure 4.4: Marginal stability contours for $\gamma = 0$. (a) Influence of σ^2 for $m = 10\pi$. (b) Influence of m for $\sigma^2 = 1$.

4.3.3 Effect of correlation length

For larger values of m , the contribution of \mathcal{I}_w to net vorticity is expected to increase because of larger gradients of permeability within the boundary layer. To investigate this effect, figure 4.4(a) plots the marginal stability curves for $Ra = 500$, $\gamma = 0$, $m = 10\pi$ and different value of σ^2 . The overall stability behavior, as a function of σ^2 , is quantitatively different compared with the case of $m = 6\pi$ considered in figure 4.1(a). In the case of $m = 10\pi$ considered in figure 4.4(a), instability is found to decrease with an increase in σ^2 . This effect is more obvious at times greater than about $t > 0.4$, which indicates that the influence of the two modes of vorticity production changes in time due to the change in the thickness of the boundary layer. For $\sigma^2 = 1.1$, the marginal stability curve splits into two separate unstable regions that continue to diminish with a further increase in the

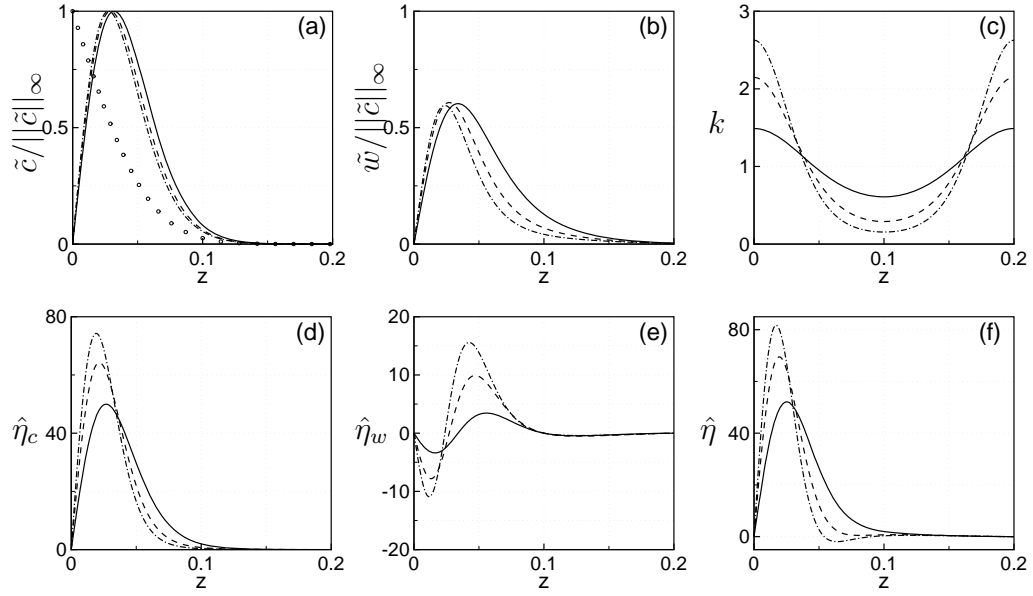


Figure 4.5: Spatial variation of perturbation and vorticity contributions for $\ell = 40$, $m = 10\pi$ and $t = 0.5$. Lines represent, $\sigma^2 = 0$ (solid), $\sigma^2 = 0.1$ (dashed) and $\sigma^2 = 0.5$ (dash-dot).

variance. figure 4.4(b) plots the effect of m for $\sigma^2 = 1$. As m is increased from 8π to 10π the marginal stability curve shrinks substantially. With a further increase in m to 10.4π , the marginal stability curve again splits up, similar to the case for $m = 10\pi$ and $\sigma^2 = 1.1$ shown in figure 4.4(a). The lower branch disappears entirely with a further increase in m to 12π .

The physical basis for reduced instability at larger values of m and σ^2 , indicated in figure 4.4, is explained with the help of figure 4.5. The profiles for scaled concentration perturbations observed in figure 4.5(a) are not sensitive to σ^2 . The corresponding peak velocity perturbations are similarly not sensitive to σ^2 , but the profiles move slightly inwards into the boundary layer when σ^2 is increased, as

shown in figure 4.5(b). Permeability profiles plotted in figure 4.5(c) indicate that k undergoes a relatively smaller increase in the neighborhood of the peak of $\tilde{c}/\|\tilde{c}\|_\infty$ with an increase in σ^2 compared with the case for $m = 6\pi$ shown in figure 4.2(c). Consequently, the increase in the corresponding vorticity contribution, $\hat{\eta}_c$, is relatively smaller for $m = 10\pi$ as shown in figure 4.5(d) compared with the case for $m = 6\pi$ shown in figure 4.3(a). The permeability gradients on the other hand are now much larger and lead to significantly larger values of $\hat{\eta}_w$ with an increase in σ^2 , as shown in figure 4.5(e). The effect on $\hat{\eta}$, plotted in figure 4.5(f), shows that vorticity is now confined to a narrower region of the boundary layer. This results in a decrease in the net vorticity, $\mathcal{I} = (2.40, 2.32, 2.23)$, with an increase in variance, $\sigma^2 = (0.1, 0.5, 1.0)$, which coincides with a corresponding decrease in the growth rate, $\omega_\infty = (1.43, 1.22, 0.70)$.

The overall effect of the interaction of the two mechanisms of vorticity production described above is summarized in figure 4.6, which plots contours of t_c in the plane of σ^2 and m . These results are obtained with the DMA, given by (4.11). Figure 4.6 indicates that t_c decreases with an increase in σ^2 for small values of m and increases with an increase in m for larger values of m . A transition from one type of behavior to the other is observed to occur at intermediate values of m . A sharp jump in the critical time, t_c , occurs for large values of σ^2 because the lower of the two stability branches, shown in figure 4.4, vanishes, and t_c jumps to the larger value on the upper branch. For smaller values of σ^2 the transition is gradual. Such transitions are associated with the relative strength of the vorticity production mechanisms, see equation (4.14), related to the magnitude and the gradient of

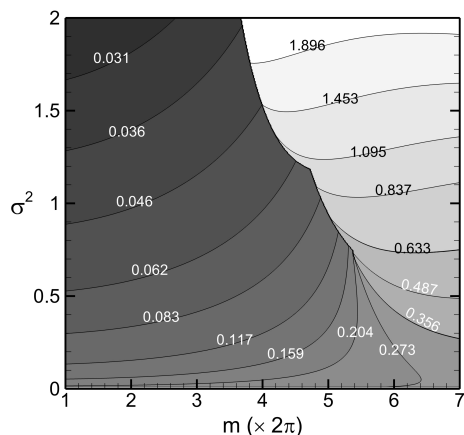


Figure 4.6: Effect of σ^2 and m , on the critical time for the onset of instability, t_c , determined by the DMA, (4.11). Numbers indicate the magnitude of t_c . Gray scale emphasizes the direction of increasing and decreasing values of t_c , with lighter (darker) color indicating higher (lower) values.

permeability. The mode of instability switches from being dominated by the magnitude of permeability for smaller values of m to being dominated by the gradients of permeability for large values of m . Note that the effect of *mode switching* is most prominent when high permeability regions are located closer to the top boundary, $z = 0$, for $-3\pi/4 < \gamma < 3\pi/8$. In this range, the effects of mode switching observed in figures 4.4 and 4.6 extend to the onset of nonlinear convection, as described next in §4.4.

4.4 Onset of natural convection

The onset of natural convection that marks the beginning of a period of enhanced dissolution, occurs in response to perturbation amplification within the linear

regime. At the time of the onset of convection, the flux of CO₂ into brine transitions from a diffusive to a convective regime. The critical time for the onset of convection is defined as the minimum onset time for the onset of convection over all perturbation wavenumbers. The onset of convection is associated with the onset of nonlinear effects that are triggered when the perturbation amplitude becomes sufficiently large. With the help of 2-D numerical simulation, this study explores the dependence of the onset time of nonlinear convection on the amplification of perturbations that are predicted using linear theory. It is shown that due to the dependence, the mode switching behaviors in the linear regime are also observed in the onset of convection.

A direct numerical simulation (DNS) based on the vorticity streamfunction formulation is used to solve equations (4.1) (Riaz *et al.*, 2006). The numerical method uses a spectral discretization in the x -direction, compact finite differences in the z -direction and a 3rd order Runge-Kutta, explicit time integration. Periodic boundary conditions are used in the x -direction. Initial conditions for the DNS are set as, $u = w = 0$ and

$$c(x, z, t_o) = c^o(z, t_o) + \varepsilon \cos(\ell x) \tilde{c}_o(z) , \quad (4.17)$$

where t_o is the time at which the system is perturbed, $c^o(z, t_o) = \operatorname{erfc}(z\sqrt{Ra/4t_o})$ is the base state for the linear stability analysis, ε is the initial perturbation amplitude, ℓ is the perturbation wavenumber and $\tilde{c}_o(z)$ is the initial perturbation defined in (2.44). The minimum amplitude is $\varepsilon = 0$, which cannot lead to instability because of the quiescent initial state, $u = w = 0$. As in Chapter 2, the maximum value

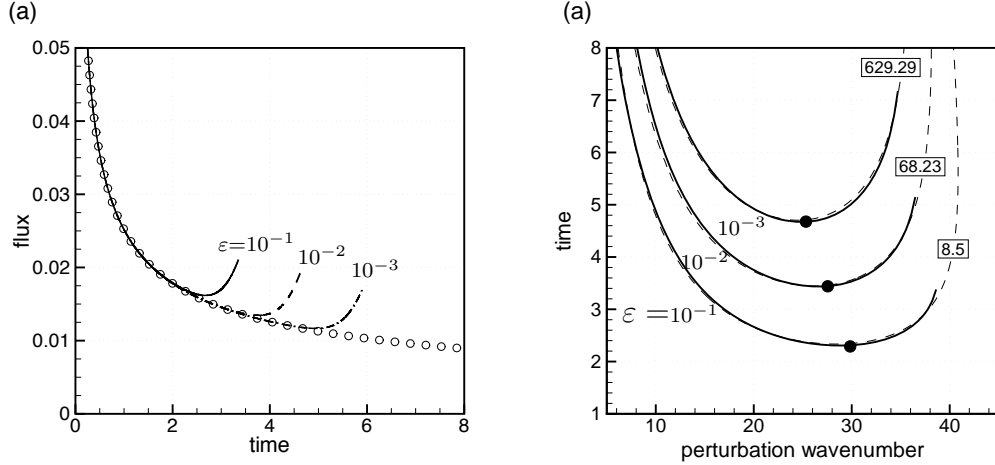


Figure 4.7: (a) Flux, $J(t)$, for $Ra = 500$, $\ell = 20$, $\sigma^2 = 0$, $a_r = 2\pi/\ell$ and $t_o = 0.01$ for various values of the perturbation amplitude. Symbols represent the flux associated with the diffusive boundary layer (b). Time for convection onset, t_n , as a function of ℓ obtained from DNS (solid lines). Amplification, Φ , at t_n is only a function of ε . The critical onset time, t_{nc} , (symbols) occurs on the path of maximum amplification, $\Phi^*(t)$, (dashed line) in the linear regime.

of ε is constrained by the requirement, $c(x, z, t_o) > 0; \forall(x, z)$, to ensure that no unphysical negative values of concentration occur at $t = t_o$ and beyond. Tilton *et al.* (2013) derived an asymptotic scaling that showed how the onset time of convection approaches infinity as the amplitude goes to zero.

4.4.1 Critical time of convection onset

The time at which convection initiates for the first time is typically associated with the point of deviation of the flux from the diffusive behavior. The flux of CO_2 into brine is obtained by integrating the normal concentration gradient across the

boundary at $z = 0$ from $x = 0$ to the domain width, $x = a_r$,

$$J(t) = -\frac{1}{a_r Ra} \int_0^{a_r} \frac{\partial c}{\partial z} \Big|_{z=0} dx . \quad (4.18)$$

The time at which the onset of natural convection occurs is taken to be the time, t_n , when $dJ/dt = 0$. The flux, $J(t)$, obtained from the DNS for various values of the initial amplitude, ε , is shown in figure 4.7(a) for $Ra = 500$, $\ell = 20$, $\sigma^2 = 0$, $a_r = 2\pi/\ell$ and $t_o = 0.01$. Symbols represent the diffusive flux in the linear regime, $1/\sqrt{\pi Ra t}$. Figure 4.7(a) shows that the flux follows the diffusive path initially. Eventually, nonlinear interactions between the perturbed mode and its harmonics modify the mean concentration to deviate the flux from the diffusive behavior (Tilton & Riaz, 2014).

The onset time t_n is plotted as a function of ℓ in figure 4.7(b). A critical time for the onset of convection, t_{nc} , can be defined as the minimum value of t_n over all perturbation wavenumbers. In order to associate t_{nc} with the dynamics in the linear regime, the amplification attained by a given perturbation over a specific time interval, $\{t_o, t\}$, is defined as,

$$\Phi(t; \ell) = \frac{\|\tilde{c}(z, t; \ell)\|_2}{\|\tilde{c}(z, t_o)\|_2} = \exp \int_{t_o}^t \omega_2(t; \ell) dt . \quad (4.19)$$

Note that the growthrates, ω_2 (IVP), and the perturbation profile, \tilde{c} , are obtained using linear theory, while the onset of convection is calculated via DNS. The term on the right in (4.19) indicates explicitly that the amplification measures the combined effect of the instantaneous growth rates, summed over a specific period of time. Clearly, $\Phi(t; \ell)$ is a function of t_o , see Chapter 2. The initial time is $t_o = 0.01$ which is about an order of magnitude smaller than the onset time for instability in

homogeneous media. The maximum amplification at any given time can then be defined as,

$$\Phi^*(t) = \sup_{\ell} \{\Phi(t; \ell)\} . \quad (4.20)$$

Tilton & Riaz (2014) show that the amplification based on the linear analysis accurately predicts the nonlinear amplification at the onset of convection because of the weak nonlinearity at t_{nc} . The critical time for the onset of convection thus occurs along the path followed by $\Phi^*(t)$ in (t, ℓ) -space, as shown in figure 4.7(b) with the dashed line. The minimum level of amplification needed to trigger the onset is also noted for different values of ε . Next, it is considered how the specific profile of the path of $\Phi^*(t)$ and its magnitude influence the time for the onset of convection.

4.4.2 Influence of mode switching on convection onset

The dependence of t_{nc} on ε , $\Phi^*(t)$ and the heterogeneity parameters is examined in figure 4.8 for $Ra = 500$, $t_o = 0.01$ and $a_r = 2\pi/\ell$. Figure 4.8(a) shows the effect of variance for three different values of σ^2 and $\varepsilon = 10^{-2}$. In each case, t_{nc} transitions from a set of small to large values with an increase in m . The transition is gradual when $\sigma^2 = 0.1$ but becomes progressively steeper for larger values of σ^2 . Figure 4.8(a) further shows that with an increase in the variance, t_{nc} decreases to the left of the transition region but increases to the right. This transition is similar to the one observed in figure 4.6 with respect to the critical time for the onset of instability, t_c . The behavior of t_{nc} depicted in figure 4.8(a) is a consequence of the mode switching mechanisms in the linear regime as discussed in §4.3.

In order to understand the effect of mode switching on the behavior of t_{nc} observed in figure 4.8(a), let us consider the temporal evolution of $\Phi^*(t)$ in figure 4.8(b-d). Figure 4.8(b) illustrates $\Phi^*(t)$ as a function of time for $m = 4\pi$ and two different values of $\sigma^2 = 0.1$ and 0.5 . The critical time for the onset of convection, t_{nc} , corresponding to $\varepsilon = 10^{-3}$, 10^{-2} and 10^{-1} is marked with symbols. Figure 4.8(b) shows that for all values of ε the amplification, $\Phi^*(t)$, is greater when the variance is larger. Therefore, the minimum amplification required for the onset is attained more quickly for the case of $\sigma^2 = 0.5$ resulting in an earlier onset time. This explains the behavior of the decrease in t_{nc} with an increase in σ^2 for small values of m , as shown in figure 4.8(b). Note further in figure 4.8(b) that the amplification needed to trigger the onset of convection for a fixed value of ε is similar to that in the homogeneous case shown in figure 4.7(b).

To examine the transition region noted in figure 4.8(b), let us consider the case of $m = 6.5\pi$ in figure 4.8(c). In this case, $\Phi^*(t)$ is greater for $\sigma^2 = 0.5$ until about $t = 3$. A point of crossover occurs beyond this time where the amplification is greater for the case of $\sigma^2 = 0.1$. As a consequence of the crossover, the critical onset time, t_{nc} , for various values of σ^2 depend additionally on ε . The crossover can be attributed to the mode switching effects that are brought about in this case by the shift in the relative strength of vorticity contributions as a result of boundary layer growth. For larger values of ε , t_{nc} occurs earlier for $\sigma^2 = 0.5$. On the other hand, for smaller values of ε , t_{nc} occurs later for $\sigma^2 = 0.5$ because the level of amplification needed to trigger the onset of convection is attained beyond the point of crossover. Finally, in the case of a large value of $m = 12\pi$ shown in figure 4.8(d), the crossover

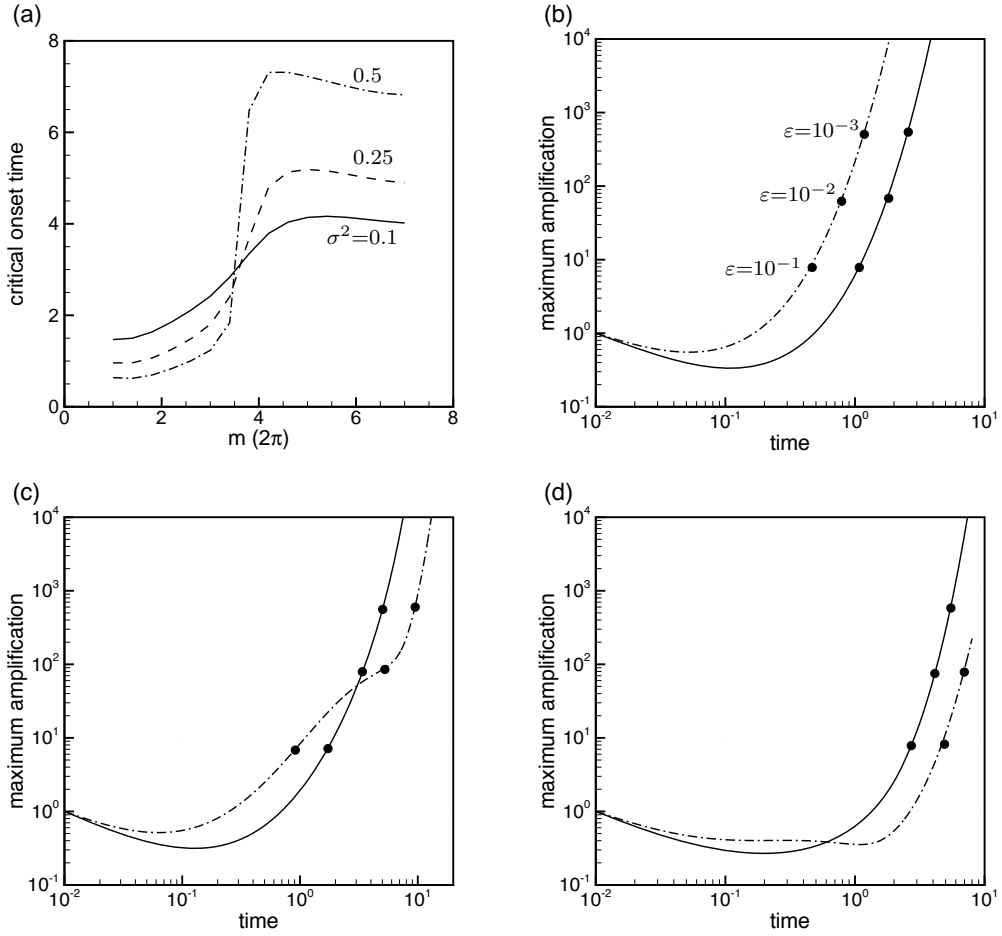


Figure 4.8: (a) Influence of permeability variance, σ^2 on the critical onset time, t_{nc} , for $Ra = 500$, $t_o = 0.01$ and $\varepsilon = 10^{-2}$. (b), (c) and (d) show $\Phi^*(t)$ vs. time for $m = 4\pi$, 6.5π and 12π , respectively. Solid symbols mark t_{nc} for three different values of ε .

occurs relatively early in time. Consequently, $\Phi^*(t)$ attains the threshold for the onset well beyond the point of crossover for all values of ε . This explains why t_{nc} is delayed with an increase in variance for large m , as observed in figure 4.8(a).

Note that in this chapter, the problem is studied with respect to a single value of the Rayleigh number. This is because a simple rescaling based on an internal length scale formed with buoyancy velocity and diffusivity can be used to obtain corresponding results at other values of the Rayleigh number, see §2.4.3 in Chapter 2. This type of rescaling is also appropriate for characterizing the onset of the nonlinear convection as long as the boundary layer does not interact with the bottom aquifer boundary.

4.5 Conclusions

This study explores the instability behavior with respect to interactions between the permeability and perturbation profiles within the transient boundary layer. Two main vorticity modes are discussed. The first mode is related to the coupling between the concentration field and the magnitude of permeability within the boundary layer. The second mode of vorticity is associated with the coupling of the velocity perturbation with the gradients of permeability within the boundary layer. The gradients of permeability become important when the wavelength of permeability oscillation is small compared with the thickness of the boundary layer. Perturbations in the velocity field either enhance or diminish the vorticity produced by the first mode, depending on the permeability phase. The time required by any

perturbation to amplify sufficiently and trigger the onset of nonlinear convection depends on the instantaneous contribution of each vorticity mode, which changes in time with an increase in the boundary layer thickness. Vorticity production can transition quickly from one mode to the other in response to small changes in the permeability field when the variance is high, resulting in abrupt changes in the onset time for convection.

Our description of physical mechanisms provides a framework for the evaluation of practical problems. For example, heterogeneity may be characterized by multiple length scales and sharp changes in the permeability field whose effect on the onset of convection can be understood with respect to the interaction of individual vorticity modes. In the case of multiple permeability length scales, mode switching effects are expected to be present depending upon the magnitude of permeability gradients in the boundary layer. In the limit of high permeability and high variance, the periodic model can also account for abrupt changes in permeability.

Chapter 5: Natural convection in vertically layered porous media

5.1 Overview

This chapter explores the onset of natural convection in a vertically layered porous medium in which permeability varies perpendicular to the direction of gravity. Past studies that have dealt with steady diffusive boundary layers (McKibbin, 1986; Nield, 1986) model the horizontally varying permeability field using discrete slabs. These studies also report higher instability compared to the constant permeability case. The distinguishing feature of the present stability problem, in addition to the transient nature of the base-state, is that the shape of the eigenmodes in the horizontal direction can no longer be represented by pure Fourier modes. Due to interaction with permeability field, perturbation modes are no longer independent of each other. The stability analysis therefore, cannot be performed using the classical normal mode decomposition. Instead, this chapter utilizes a multi-dimensional eigenvalue problem (Theofilis, 2011).

The chapter is outlined as follows. The governing equations are presented in §5.2. The linear stability results are shown in §5.3 and the onset of nonlinear convection in §5.4. The conclusions are discussed in §5.5.

5.2 Governing equations and methodology

The geometry and modeling assumptions are similar to those in previous chapters. This study considers a two-dimensional isotropic porous medium of infinite width and height H . To analyze the instability characteristics, a periodic permeability is adopted,

$$K^* = K_g \exp [a \cos (kx)], \quad (5.1)$$

where $K_g = (K_{max}K_{min})^{0.5}$ is the geometric mean, K_{max} and K_{min} refer to the maximum and minimum values of permeability, a is the permeability amplitude, k is the permeability wavenumber, and x is the horizontal direction perpendicular to the direction of gravity. Note that permeability phase is not modeled because linear stability results are independent of phase. The variations in dispersivity, D , and porosity, ϕ , are assumed to be small compared to the permeability variations. Viscosity is treated as a constant and the density profile is linear of the form, $\rho = \rho_0 + \Delta\rho c$, where ρ_0 is the density of pure brine, $\Delta\rho$ is the density difference of CO₂-saturated brine and pure brine. Because density differences are small, $\Delta\rho/\rho \ll 1$, Boussinesq approximation is applied. Using the characteristic length, $L_c = H$, time $T_c = H/(\phi U_c)$, permeability $K_c = K_g$, buoyancy velocity $U_c = K_g \Delta\rho g / \mu$ and pressure $P_c = \Delta\rho g H$, one obtains the non-dimensional form of the governing equations,

$$K \mathbf{v} + \nabla p - c \mathbf{e}_z = 0, \quad \nabla \cdot \mathbf{v} = 0, \quad \frac{\partial c}{\partial t} + \mathbf{v} \cdot \nabla c - \frac{1}{Ra} \nabla^2 c = 0, \quad (5.2)$$

These equations are the Darcy's law and the volume averaged forms of the continuity and concentration advection-diffusion equations respectively. The Rayleigh number is defined as $Ra = U_c H / (\phi D)$. The symbol $\mathbf{v} = [u, w]$ is the nondimensional velocity vector, c is the nondimensional concentration and p is the nondimensional pressure obtained from the dimensional pressure \hat{p} through the relation $p = (\hat{p} - \rho_0 g z) / P$. The symbol \mathbf{e}_z is the unit vector in the z direction.

The boundary conditions for (5.2) are,

$$c|_{z=0} = 1, \quad \frac{\partial c}{\partial z}\bigg|_{z=1} = 0, \quad w|_{z=0} = w|_{z=1} = 0, \quad t \geq 0. \quad (5.3)$$

Equations (5.2) admit the transient base state,

$$\mathbf{v}_b = \mathbf{0}, \quad c_b(z, t) = 1 - \frac{4}{\pi} \sum_{n=1}^{\infty} \frac{1}{2n-1} \sin\left[\left(n - \frac{1}{2}\right) \pi z\right] \exp\left[-\left(n - \frac{1}{2}\right)^2 \frac{\pi^2 t}{Ra}\right], \quad (5.4)$$

The linear stability of base-state (5.4) is studied with respect to infinitesimal perturbations. The linear stability problem is formulated in terms of perturbations of the concentration field $\hat{c}(x, z, t)$ and of the stream function $\psi(x, z, t)$,

$$\frac{\partial \hat{c}}{\partial t} + \frac{\partial \hat{\psi}}{\partial x} \frac{\partial c_b}{\partial z} - \frac{1}{Ra} \mathcal{D} \hat{c} = 0, \quad \mathcal{D} \hat{\psi} - \frac{1}{K} \frac{\partial K}{\partial x} \frac{\partial \hat{\psi}}{\partial x} - K \frac{\partial \hat{c}}{\partial x} = 0, \quad (5.5)$$

$$\hat{c}\big|_{z=0} = 0, \quad \frac{\partial \hat{c}}{\partial z}\bigg|_{z=1} = 0, \quad \hat{\psi}\big|_{z=0} = \hat{\psi}\big|_{z=1} = 0, \quad (5.6)$$

$$\hat{c}\big|_{x=0} = \hat{c}\big|_{x=x_p}, \quad \hat{\psi}\big|_{x=0} = \hat{\psi}\big|_{x=x_p}, \quad (5.7)$$

where $\mathcal{D} = \partial^2 / \partial z^2 + \partial^2 / \partial x^2$, and x_p is the cut-off length in the horizontal direction.

The concentration and stream function perturbations are split into spatial and temporal components,

$$\hat{c} = c_e(x, z) e^{\sigma t}, \quad \hat{\psi} = \psi_e(x, z) e^{\sigma t}. \quad (5.8)$$

Substituting (5.8) in (5.5)–(5.11) and after transforming the regular (x, z, t) space to the self-similar (x, ξ, t) space, where $\xi = za$ is the self-similar variable of the diffusive boundary layer with $a = \sqrt{Ra/4t}$, the resultant generalized eigenvalue problem may be expressed as,

$$\sigma c_e - \frac{\xi}{2} \frac{\partial c_e}{\partial \xi} + a \frac{\partial \psi_e}{\partial x} \frac{\partial c_b}{\partial \xi} - \frac{1}{Ra} \left(a^2 \frac{\partial^2}{\partial \xi^2} + \frac{\partial}{\partial x^2} \right) c_e = 0, \quad (5.9)$$

$$\left(a^2 \frac{\partial^2}{\partial \xi^2} + \frac{\partial}{\partial x^2} \right) \psi_e - \frac{1}{K} \frac{\partial K}{\partial x} \frac{\partial \psi_e}{\partial x} - K \frac{\partial c_e}{\partial x} = 0, \quad (5.10)$$

$$c_e|_{\xi=0} = c_e|_{\xi=\xi_c} = 0, \quad \psi_e|_{\xi=0} = \psi_e|_{\xi=\xi_c} = 0, \quad (5.11)$$

$$c_e|_{x=0} = c_e|_{x=x_p}, \quad \psi_e|_{x=0} = \psi_e|_{x=x_p}, \quad (5.12)$$

where $\xi_c = 8$ is the cut off length chosen such that the perturbations tend to zero at $\xi = \xi_c$, and $x_p = 2\pi$ such that discrete integer wavenumbers are resolved in the x direction.

The spatial derivatives in (5.9)–(5.10) are discretized using fourth order finite difference schemes. The two-dimensional (2D) eigenmodes are obtained using the sparse matrix eigenvalue solver ‘eigs’ in MATLAB. For a given t and Ra , the eigenmode with the largest eigenvalue, σ , represent the dominant perturbation structure. The corresponding eigenvalue represents the dominant perturbation growth rate. Note that growth rate, σ , obtained in the self-similar (x, ξ, t) space is equivalent to perturbation growth rate in the regular (x, z, t) space when the perturbation amplitude is measured using the L_∞ norm (Tilton *et al.*, 2013).

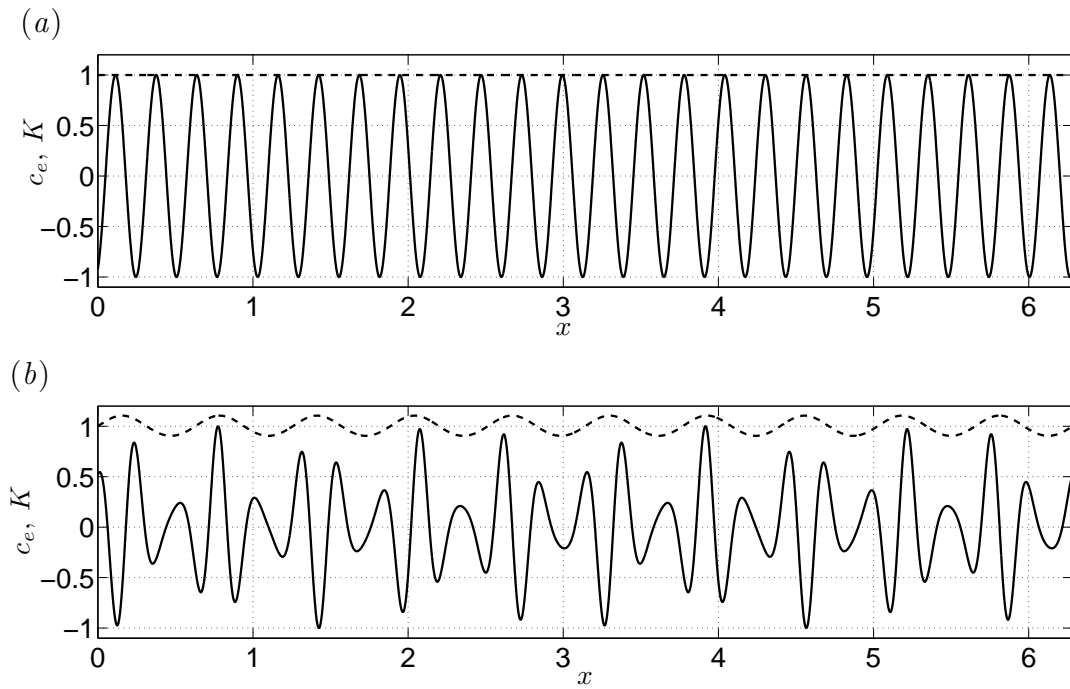


Figure 5.1: Concentration eigenmode, c_e (solid line), and permeability, K (dashed line), in the horizontal x direction for $Ra = 500$ and $t = 2$ for (a) Homogeneous porous media of $a = 0$. (b) Heterogeneous porous media of $a = 0.1$ and $k = 10$.

5.3 Linear growth characteristics

5.3.1 Quasi-steady 2D eigenmodes

Figure 5.1 illustrates the concentration eigenmode, c_e (solid line), and permeability, K (dashed line), in the spanwise x direction for $t = 2$ and $Ra = 500$. Note that these concentration shapes are identical at any horizontal slice within the boundary layer. Panel (a) illustrates the profile shapes for homogeneous porous media with $a = 0$. The least unstable eigenmode varies sinusoidally in the x direction with wavenumber of 25. This is in excellent agreement with results obtained using a normal mode decomposition, see figure 2.44(d) in Chapter 2. Figure 5.1(b) illustrates the profiles for heterogeneous porous media with permeability amplitude, $a = 0.1$, and permeability wavenumber, $k = 10$. The concentration eigenmodes, c_e , has a irregular wavy structure consisting of multiple sinusoidal or Fourier modes. It is unclear whether these modes are in phase with each other.

To further investigate the structure of the quasi-steady eigenmodes, a Fourier transform is applied in order to examine the individual Fourier components of the eigenmode. Figure 5.2 illustrates the Fourier sine coefficients, a_l (solid line), and cosine coefficients, b_l (dashed line), for $t = 2$, $Ra = 500$, and permeability amplitudes and wavenumbers of: $a = 0$ (panel a), $a = 0.1$ and $k = 1$ (panel b), $a = 0.1$ and $k = 10$ (panel c), and $a = 0.1$ and $k = 50$ (panel d). Figure 5.2(a) shows that for a homogeneous porous medium, $a = 0$, a single Fourier component is recovered at $l = 25$. This case corresponds to the eigenmode illustrated in figure 5.1(a).

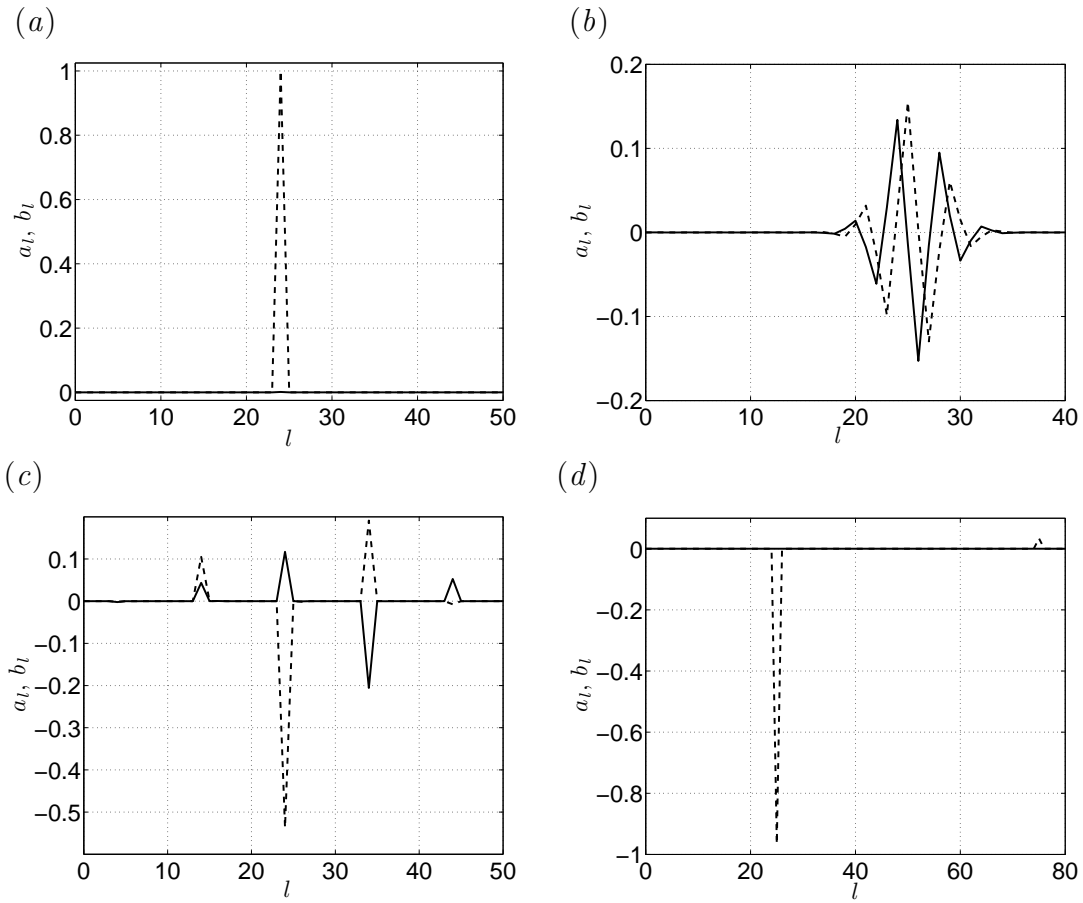


Figure 5.2: Fourier sine coefficients, a_l (solid line), and cosine coefficients, b_l (dashed line), for the horizontal variation of c_e for $t = 2$ and $Ra = 500$ in homogeneous porous media (panel *a*) and in heterogeneous porous media with $a = 0.1$, and $k = 1$ (panel *b*), $k = 10$ (panel *c*), and $k = 50$ (panel *d*) respectively.

For $a = 0.1$ and $k = 1$ (figure 5.2*b*), the least stable eigenmode consist of pure modes in the frequency band, $18 < l < 35$, clustered around the homogeneous dominant wavenumber of $l = 25$. The presence of both a_l and b_l components indicates that the eigenmode contains Fourier modes or harmonics that are not in phase with each other. With increasing permeability wavenumber, $k = 10$ (figure 5.2*c*), the sinusoidal modes are located wider apart in the spectrum. Interestingly, the Fourier component with the maximum magnitude is still located close to the homogenous dominant wavenumber, $l = 25$. The other modes located at $l = 14$, 34, and 44 are much smaller in magnitude. This case corresponds to the eigenmode illustrated in figure 5.1(*b*). When permeability wavenumber is increased to $k = 50$ (figure 5.2*d*), there is only one Fourier component at $l = 25$. This indicates that with increasing permeability wavenumber, the quasi-steady 2D eigenmodes recover the dominant perturbation structures observed for homogeneous porous media.

5.3.2 Perturbation growth

Figure 5.3 illustrates the effect of permeability wavenumber on the temporal evolution of growth rate, σ , for $Ra = 500$. Figure 5.3(*a*) illustrates σ versus t for the homogeneous case of $a = 0$ (circles) and the heterogeneous cases of $a = 0.1$ and $k = 1$ (crosses), $k = 10$ (squares), and $k = 50$ (diamonds) respectively. Perturbations experience an initial decay period, $\sigma < 0$, before experiencing positive growth rates, $\sigma > 0$, due to destabilizing effects. The smallest values for the growth rate are observed when $a = 0$, i.e. for homogeneous porous media. For $a = 0.1$, the largest

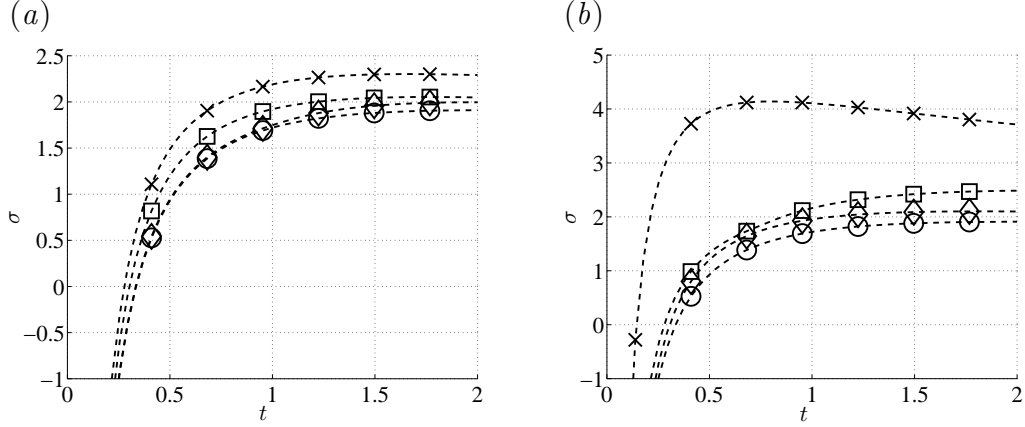


Figure 5.3: Effect of permeability wavenumber on the temporal evolution of growth rate, σ , for (a) $a = 0.1$ and $k = 1$ (crosses), $k = 10$ (squares), and $k = 50$ (diamonds). (b) $a = 0.5$ and $k = 10$ (crosses), $k = 50$ (squares), and $k = 100$ (diamonds). The results for homogeneous porous medium for $Ra = 500$ is shown using circles.

growth rates, σ , are observed for a smaller permeability wavenumber, $k = 1$. When permeability wavenumber is increased to $k = 10$, the magnitude of the growth rates decreases but remains larger than the homogeneous growth rates, $a = 0$. When $k = 50$, better agreement is observed with the homogenous case. With decreasing permeability length scales, the linear stability characteristics of a vertically layered porous medium are similar to that of a homogeneous medium.

Figure 5.3(b) illustrates σ versus t for a larger permeability amplitude, $a = 0.5$, for the heterogeneous cases with $k = 10$ (crosses), $k = 50$ (squares), and $k = 100$ (diamonds) respectively and the homogeneous case of $a = 0$ (circles). For $k = 10$, one observes the largest deviation of the growth rate from the homogeneous case. With increasing permeability wavenumbers, $k = 50$ and 100 , better agreement is found with the homogeneous case. With increasing permeability amplitude, the

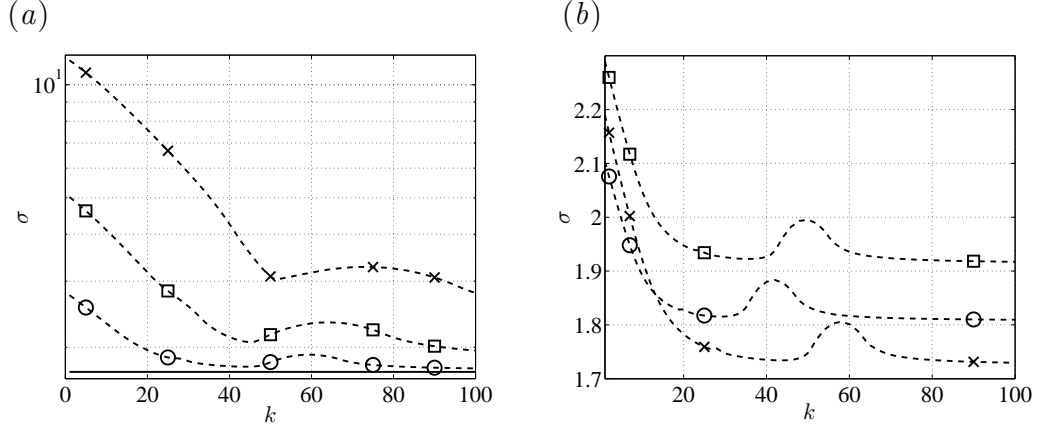


Figure 5.4: (a) Effect of permeability amplitude, a , on σ vs. k for $t = 1$ and $Ra = 500$ for $a = 0$ (solid line), $a = 0.2$ (circles), $a = 0.5$ (squares), and $a = 1$ (crosses). (b) Effect of time on σ vs k curves for $Ra = 500$ and $t = 1$ (crosses), $t = 2$ (squares) and $t = 4$ (circles).

instabilities are found to be more stronger. Our results suggest that the effect of horizontal permeability is to increase the instability of transient diffusive boundary layers. This instability enhancing effect of a horizontally varying permeability field is similar to the previous studies of McKibbin (1986) and Nield (1986) on steady diffusive boundary layers.

Studies on viscous fingering in heterogeneous media (DeWit & Homsy, 1997; Riaz & Meiburg, 2004) have reported a resonance behavior when the length scale of the viscous fingering instability is close to that of the heterogeneous instability. To examine whether similar effects exist for the case of a gravitational instability, let us look at the perturbation growth rate for a fixed time, $t = 1$, for $Ra = 500$ and vary the length scale of the horizontal heterogeneity field. Figure 5.4(a) illustrates growth rate, σ , for the permeability wavenumbers, $1 < k < 100$, for $a = 0$ (solid line) and $a = 0.2$ (circles), $a = 0.5$ (squares), and $a = 1$ (crosses). As observed earlier,

the maximum growth rates are bounded by the maximum value of permeability and occurs for large permeability length scales. In the limit of k approaching zero, $k \rightarrow 0$, the growth rate is equal to that of a homogeneous porous media with a constant permeability of $K_g \exp(a)$. Resonance behavior is observed for heterogeneous media when k is large. For $a = 0.2$, after the initial decay, the growth rate starts to increase at $k = 42$, reaches a local maxima at $k = 59$, and begins to decrease again. The local maxima is approximately twice the value of the dominant perturbation wavenumber, $\ell_{max} = 28$, for a homogeneous media of permeability K_g . For larger values of the permeability amplitude a , the resonance behavior occurs for higher permeability wave numbers k .

Because of the unsteady nature of the boundary layer, these resonance effects are also time dependent. Figure 5.4(b) illustrates σ versus k curves for $a = 0.1$ and $t = 1$ (crosses), $t = 2$ (squares), and $t = 4$ (circles). Note that the maximum growth rates are observed at $t = 2$. It is known that the dominant wavenumbers for a homogeneous porous medium decrease monotonically with time, see figure 2.44(d). Consequently, the location of the resonance behavior, which is approximately around permeability wavenumbers that are twice in magnitude to that of the homogeneous dominant perturbation wavenumbers, shifts with time. With increasing time, resonance occurs for smaller permeability wavenumbers. In §5.4, it is shown how these resonance behaviors observed in the linear regime affect the onset of nonlinear convection.

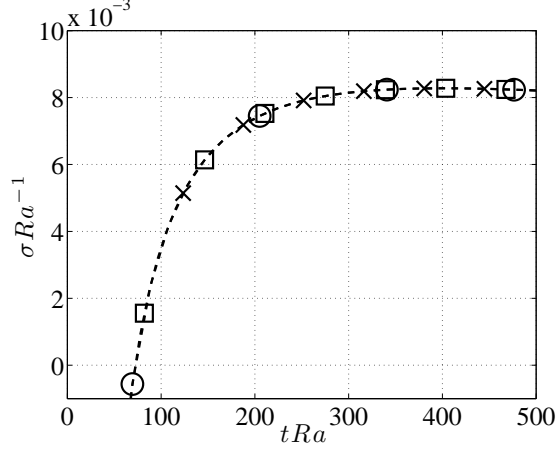


Figure 5.5: σRa^{-1} vs. tRa , for $a = 0.5$ and combinations of $Ra = 500$ and $k = 10$ (circles), $Ra = 250$ and $k = 5$ (crosses), and $Ra = 750$ and $k = 15$ (squares).

5.3.3 Scaling with Rayleigh number

Figure 5.5 illustrates the temporal evolution of the perturbation growth rate for a fixed perturbation amplitude of $a = 0.5$ and different combinations of $Ra = 500$ and $k = 10$ (circles), $Ra = 250$ and $k = 5$ (crosses), and $Ra = 750$ and $k = 15$. The growth rates and times are scaled such that the plot shows curves of σRa^{-1} versus tRa . The results for different Ra and k collapse to a single curve. Consequently, all the results in this study can be generalized using the following scaling. If (σ, t, k) is known for a given Ra , then the corresponding values for Ra^* are $(\sigma Ra^*/Ra, tRa/Ra^*, kRa^*/Ra)$.

5.4 Onset of natural convection

Two-dimensional direct numerical simulations (DNS) are performed using a vorticity stream function formulation of the nonlinear governing equations (5.2)–(5.3). This scheme uses a spectral discretization in the x -direction, compact finite differences in the z -direction and a 3rd order Runge-Kutta, explicit time integration. The horizontal domain is truncated to $x \in [0, 2\pi]$ with periodic boundary conditions on $x = 0$ and $x = 2\pi$. The initial conditions are $u = w = 0$ with initial concentration field prescribed at $t = 0.1$,

$$c(x, z) = c_b(z) + \varepsilon \cos(\ell x + \gamma) \frac{c_i(z)}{\|c_i(z)\|_\infty}, \quad (5.13)$$

where c_b is the base state from the linear stability analysis, $\varepsilon = 0.1$ is the initial perturbation amplitude, ℓ is the perturbation wavenumber, γ is the perturbation phase, and $c_i(z) = z \exp(-z^2 \sqrt{Ra/(4t)})$, is the initial perturbation. This initial condition was found previously in Chapter 2 to be a good approximation of the optimal shape for linear growth.

As in previous chapters, the onset time of natural convection, t_o , occurs when $dJ/dt = 0$, where J is the mean flux of CO₂ into the brine given by,

$$J(t) = -\frac{1}{2\pi} \int_0^{2\pi} \frac{1}{Ra} \frac{\partial c}{\partial z} \Big|_{z=0} dx. \quad (5.14)$$

Simulations are first performed to measure t_o as a function of the perturbation wavenumber ℓ for a fixed permeability wavenumber k and perturbation phase γ . The critical time for the onset of convection is defined as follows

$$t_o^{min}(k, \gamma) = \min_{0 \leq \ell < \infty} t_o(\ell, k, \gamma). \quad (5.15)$$

Figure 5.6 illustrates the critical onset times of natural convection, t_o^{min} (vertical axis) versus the permeability wavenumbers (horizontal axis) for $Ra = 500$ and for perturbation phases of $\gamma = 0$ (circles) and $\gamma = \pi/2$ (crosses). The dashed line without symbols measures the onset times of linear instabilities, t_c , i.e the time corresponding to $\sigma = 0$, obtained using the 2D eigenvalue problem. The linear onset time, t_c , decreases with increase in permeability wavenumber. As explained earlier in §5.3.2, the maximum linear growth rates are observed for $k \rightarrow 0$. For permeability amplitude of $a = 0.1$ (panel *a*), the onset of instabilities is close to the onset time predicted by linear theory for homogeneous media, $t_c \sim 0.34$. The values for critical nonlinear onset times are much greater with $t_o^{min} \sim 1$.

For $a = 0.5$ (panel *b*), the boundary layer is more unstable. When $k < 50$, the values for the linear onset time, t_c , and the nonlinear onset time, t_o^{min} , are smaller compared to $a = 0.1$. When $k > 50$, the values for t_c are similar to the case of $a = 0.1$, but the corresponding values for nonlinear onset times, $t_o^{min} \sim 0.9$, are smaller than the previous case of $a = 0.1$. The earlier onset times for t_o^{min} for larger permeability wavenumbers may be due to stronger resonance between instability and permeability structures, see §5.3.2. At small times, resonance effects are observed for much larger permeability wavenumbers while for large times, they are observed for smaller permeability wavenumbers. Because t_o occurs much later than t_c , perturbation structures are more prone to resonance effects when $k > 50$.

Resonance effects are notably enhanced when the permeability amplitude is increased to $a = 1$ (panel *c*). Nonlinear onset times, t_o^{min} , when $k > 60$, occur even earlier even though linear onset times, t_c , have been delayed compared to the

$a = 0.5$ case. The variation of onset times due to different perturbation phase, γ , may signify the resonance interactions taking place between perturbation and permeability structures.

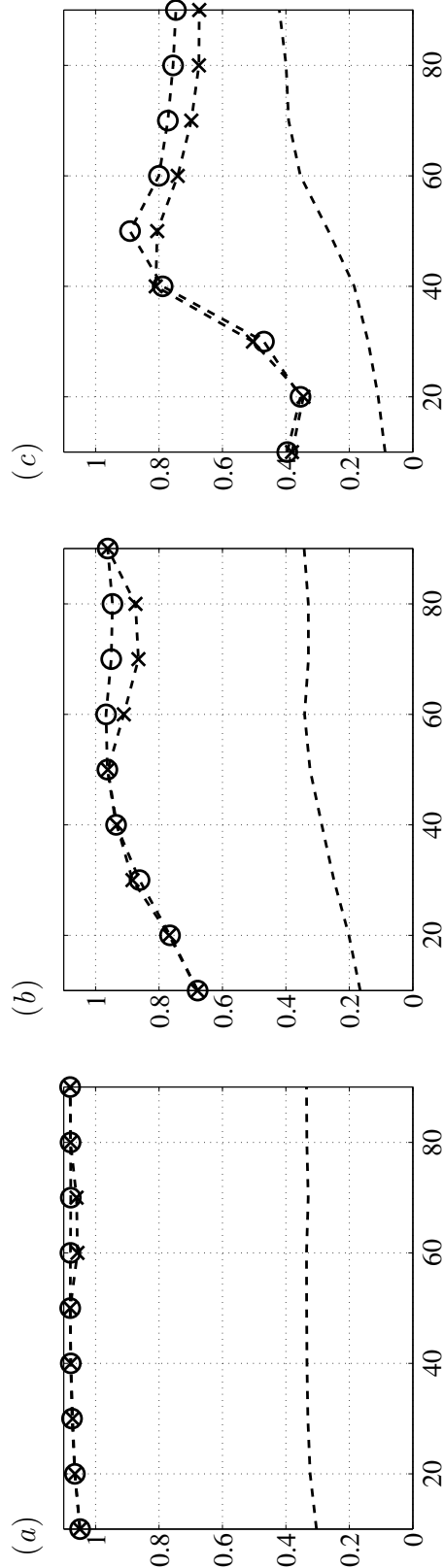


Figure 5.6: t_0^{min} (vertical axis) vs. permeability wavenumbers, k (horizontal axis) for $Ra = 500$ and for $\gamma = 0$ and $\gamma = \pi/2$ (crosses). The dashed line (no symbols) corresponds to the onset time of linear instabilities obtained using the 2D eigenvalue problem. The three figures correspond to cases of permeability amplitude of (a) $a=0.1$, (b) $a=0.5$, and (c) $a=1$. The onset time of instabilities qualitatively represents the trends in the onset of natural convection

5.5 Conclusions

This chapter explores the linear instability of transient, diffusive boundary layers in a vertically layered isotropic porous media using a multi-dimensional eigenvalue formulation. Due to interactions between permeability and perturbation structures, the shape of dominant quasi-steady eigenmodes in the transverse direction may consist of multiple sinusoidally varying modes. This is in contrast to previous linear stability analysis on transient, diffusive boundary layers. The boundary layer is more unstable in a vertically layered porous medium and is bounded by the maximum local value of permeability. The perturbation growth rates are always larger than the corresponding values for homogeneous media. Furthermore, resonant interactions between the permeability and perturbation fields are found to enhance the growth rates for large permeability wavenumbers. Because of the transient boundary layer, these resonant interactions are also time-dependent. The location around which these effects act vary from large permeability wavenumbers at small times to small permeability wave numbers at large times. Our results suggest that resonant interactions play an important role in determining the onset of nonlinear convection in aquifers with small permeability length scales.

Chapter 6: Contributions and Future work

6.1 Contributions

The following journal articles have been published/submitted as part of this work on gravitationally driven instabilities in porous media:

- “Optimal perturbations of gravitationally unstable, transient boundary layers in porous media”, D. Daniel, N. Tilton, and A. Riaz, *Journal of Fluid Mechanics*, 727, 456-487, 2013.
- “Effect of viscosity contrast on gravitationally, unstable, diffusive boundary layers”, D. Daniel and A. Riaz, *Physics of Fluids*, 26, 116601, 2014.
- “Onset of natural convection in layered saline aquifers”, D. Daniel, A. Riaz, and H. Tchelepi, *Journal of Fluid Mechanics*, in review.
- “Onset of natural convection in a vertically layered porous medium”, D. Daniel and A. Riaz, in preparation.

In addition to the above works, the dissertation author D. Daniel has made scientific contributions via the following articles:

- “The linear transient period of gravitationally unstable, diffusive boundary layers developing in porous media”, N. Tilton, D. Daniel, and A. Riaz, *Physics of Fluids*, 25, 092107, 2013

Contribution: In the development and analysis of modal and nonmodal linear stability procedures.

- “An empirical theory for gravitationally unstable flow in porous media”, R. Farajzadeh, B. Meulenbroek, D. Daniel, A. Riaz, J. Bruining, *Computational Geosciences*, 17, 515-527, 2013

Contribution: In the analysis of nonlinear computational simulations.

6.2 Future work

The following areas have been identified for future exploration:

- In chapter 2 of this study, an optimization procedure was employed to examine the perturbation structure with the maximum amplification in the linear regime. Similarly, one could carry out an optimization procedure to find the optimal initial profile that results in the earlier onset of nonlinear convection. The new optimization procedure would consist of a weakly nonlinear analysis that can efficiently predict the onset of nonlinear convection.
- This study predominantly explores gravity-driven instabilities of CO₂ sequestration using a fixed interface model which assumes a fixed two-phase interface between CO₂ and underlying brine. On the other hand, experimental studies

of CO₂ sequestration, see Chapter 3, model a moving two-phase interface. The degree to which either the fixed, or the moving interface model corresponds to the actual physical problem of two-phase flow remains to be determined because of the difficulty of setting up such an experiment and making quantitative measurements. Further work in developing suitable models of CO₂ sequestration is vital to understand CO₂ storage mechanisms in subsurface saline aquifers, and consequently, improve estimates for the onset times of natural convection.

- This study provides a robust foundation on the effect of horizontal and vertical variation of permeability on the stability of transient, diffusive boundary layers in porous media. Characterizing the stability behavior in random permeability fields is an avenue for future work.
- This study explores the time scales associated with the onset of linear instabilities and the onset of natural convection. A further exploration into the regime beyond the onset of natural convection is beckoning and is currently missing in literature.

Bibliography

- BACKHAUS, S., TURITSYN, K. & ECKE, R., E. 2011 Convective instability and mass transport of diffusion layers in a Hele-Shaw geometry. *Phys. Rev. Lett.* **106**, 104501.
- BANDO, S., TAKEMURA, F., NISHIO, M., HIHARA, E. & AKAI, M. 2004 Viscosities of aqueous NaCl solutions with dissolved CO₂ at (30-60) C and (10 to 20) MPa. *J. Chem. Eng. Data* **49**, 1328–1332.
- BEAR, J. 1988 *Dynamics of Fluids in Porous Media*. Dover Publications.
- BEN, Y., DEMEKHIN, E. A. & CHANG, H.-C 2002 A spectral theory for small-amplitude miscible fingering. *Phys. Fluids* **14** (3), 999–1010.
- BICKLE, MIKE, CHADWICK, ANDY, HUPPERT, HERBERT E., HALLWORTH, MARK & LYLE, SARAH 2007 Modelling carbon dioxide accumulation at Sleipner: Implications for underground carbon storage. *Earth. Planet. Sci. Lett.* **255** (1-2), 164–176.
- BLAIR, L. M. & QUINN, J. A. 1969 The onset of cellular convection in a fluid layer with time-dependent density gradients. *J. Fluid Mech.* **36** (02), 385–400.
- CALTAGIRONE, J. P. 1980 Stability of a saturated porous layer subject to a sudden rise in surface temperature: Comparison between the linear and energy methods. *Q. J. Mech. Appl. Math.* **33** (1), 47–58.
- CAMHI, E, MEIBURG, E & RUTH, M 2000 Miscible rectilinear displacements with gravity override. Part 2. Heterogeneous porous media. *J. Fluid Mech.* **420**, 259–276.
- CHADWICK, R. A., ARTS, R. & EIKEN, O. 2005 4D seismic quantification of a growing CO₂ plume at Sleipner, North Sea. In *6th Petroleum Geology Conference, Geological Society London*, , vol. 6, p. 13851399. Geological Society London.
- CHEN, CY & MEIBURG, E 1998 Miscible porous media displacements in the quarter five-spot configuration. Part 2. Effect of heterogeneities. *J. Fluid Mech.* **371**, 269–299.

- CHENG, P., BESTEHORN, M. & FIROOZABADI, A. 2012 Effect of permeability anisotropy on buoyancy-driven flow for CO₂ sequestration in saline aquifers. *Water Resour. Res.* **48** (9).
- CHRISTIE, M. A., MUGGERIDGE, A. H. & BARLEY, J. J. 1993 3D simulation of viscous fingering and wagg schemes. *SPE Reservoir Eng.* **8** (1), 19–26.
- CLIFTON, P. M. & NEUMAN, S. P. 1982 Effects of kriging and inverse modeling on conditional simulation of the Avra valley aquifer in Southern Arizona. *Water Resour. Res.* **18** (4), 1215–1234.
- DAGAN, G. 1984 Solute transport in heterogeneous porous formations. *J. Fluid Mech.* **145**, 151–177.
- DELHOMME, J. P. 1979 Spatial variability and uncertainty in groundwater-flow parameters - geostatistical approach. *Water Resour. Res.* **15** (2), 269–280.
- DEWIT, A & HOMS, GM 1997 Viscous fingering in periodically heterogeneous porous media .1. Formulation and linear instability. *J. Chem. Phys.* **107** (22), 9609–9618.
- DOUMENC, F., BOECK, T., GUERRIER, B. & ROSSI, M. 2010 Transient Rayleigh–Bénard–Marangoni convection due to evaporation: a linear non-normal stability analysis. *J. Fluid Mech.* **648**, 521–539.
- DRAZIN, PG & REID, WH 2004 *Hydrodynamic Stability*. Cambridge University Press.
- EHYAEI, D. & KIGER, K. T. 2014 Quantitative velocity measurement in thin-gap Poiseuille flows. *Exp. Fluids* **55** (4), 1–12.
- ELDER, J. W. 1968 The unstable thermal interface. *J. Fluid Mech.* **32** (01), 69–96.
- ELENIUS, M. T., NORDBOTTEN, J. M. & KALISCH, H. 2012 Effects of capillary transition on the stability of a diffusive boundary layer. *IMA J. Appl. Math.* **77** (6), 771–787.
- ENNIS-KING, J. & PATERSON, L. 2005 Role of convective mixing in the long-term storage of carbon dioxide in deep saline formations. *SPE J.* **10**, 349–356.
- ENNIS-KING, J., PRESTON, I. & PATERSON, L. 2003 Onset of convection in anisotropic porous media subject to a rapid change in boundary conditions. *Phys. Fluids* **17**, Article no. 084107.
- FARAJZADEH, R., MEULENBROEK, B., DANIEL, D., RIAZ, A. & BRUINING, J. 2013 An empirical theory for gravitationally unstable flow in porous media. *Computat. Geosci.* **17** (3), 515–527.

- FARAJZADEH, R., SALIMI, H., ZITHA, P. L. J. & BRUINING, H. 2007 Numerical simulation of density-driven natural convection in porous media with application for CO₂ injection projects. *Int. J. Heat Mass Tran.* **50**, 5054–5064.
- FARRELL, B. F. & IOANNOU, P. J. 1996*a* Generalized stability theory. Part I: Autonomous operators. *J. Atmos. Sci.* **53** (14), 2025–2040.
- FARRELL, B. F. & IOANNOU, P. J. 1996*b* Generalized stability theory. Part II: Nonautonomous operators. *J. Atmos. Sci.* **53** (14), 2041–2053.
- FLEURY, M. & DESCHAMPS, H. 2008 Electrical conductivity and viscosity of aqueous NaCl solutions with dissolved CO₂. *J. Chem. Eng. Data* **53** (11), 2505–2509.
- FOSTER, T. D. 1965 Stability of a homogeneous fluid cooled uniformly from above. *Phys. Fluids* **8** (7), 1249–1257.
- FREEZE, R. A. 1975 Stochastic-conceptual analysis of one-dimensional groundwater flow in nonuniform homogeneous media. *Water Resour. Res.* **11** (5), 725–741.
- GHEMAT, K., HASSANZADEH, H. & ABEDI, J. 2011 The impact of geochemistry on convective mixing in a gravitationally unstable diffusive boundary layer in porous media: CO₂ storage in saline aquifers. *J. Fluid Mech.* **673**, 480–512.
- GJERDE, K. M. & TYVAND, P. A. 1984 Thermal convection in a porous medium with continuous periodic stratification. *Int. J. Heat Mass Transfer* **27**, 2289–2295.
- GOLDSTEIN, A. W. 1959 Stability of a horizontal fluid layer with unsteady heating from below and time-dependent body force. *Tech. Rep.* NASA-TR-R-4. NASA.
- GREEN, C. P. & ENNIS-KING, J. 2010 Effect of vertical heterogeneity on long-term migration of CO₂ in saline formations. *Transport Porous Med.* **82**, 31–47.
- GREEN, L. L. & FOSTER, T. D. 1975 Secondary convection in a Hele Shaw cell. *J. Fluid Mech.* **71** (04), 675–687.
- GRESHO, P. M. & SANI, R. L. 1971 The stability of a fluid layer subjected to a step change in temperature: Transient vs. frozen time analyses. *Int. J. Heat Mass Tran.* **14** (2), 207 – 221.
- HEWITT, D. R., NEUFELD, J. A. & LISTER, J. R. 2014 High Rayleigh number convection in a porous medium containing a thin low-permeability layer. *J. Fluid Mech.* **75**, 844–869.
- HOEKSEMA, R. J. & KITANIDIS, P. K. 1985 Analysis of the spatial structure of properties of selected aquifers. *Water Resour. Res.* **21** (4), 563–572.
- HOMSY, G. M. 1973 Global stability of time-dependent flows: impulsively heated or cooled fluid layers. *J. Fluid Mech.* **60**, 129–139.

- HORTON, C. W. & ROGERS, F. T. 1945 Convection currents in a porous medium. *J. Appl. Phys.* **16**, 367–370.
- HUPPERT, H. E. & NEUFELD, J. A. 2014 The fluid mechanics of carbon dioxide sequestration. *Annu. Rev. Fluid Mech.* **46** (1).
- HUPPERT, H. E., S., TURNER J., N., CAREY S., STEPHEN R., SPARKS J. & A., HALLWORTH M. 1986 A laboratory simulation of pyroclastic flows down slopes. *J. Volcanol. Geotherm. Res.* **30**, 179199.
- JHAVERI, B. S. & HOMSY, G. M. 1982 The onset of convection in fluid layers heated rapidly in a time-dependent manner. *J. Fluid Mech.* **114**, 251–260.
- JONES, G. & FORNWALT, H. J. 1936 The viscosity of aqueous solutions of electrolytes as a function of the concentration. III. Cesium iodide and potassium permanganate. *J. Am. Chem. Soc.* **58** (4), 619–625.
- KAVIANY, M. 1984 Onset of thermal convection in a saturated porous medium: experiment and analysis. *Int. J. Heat Mass Tran.* **27** (11), 2101 – 2110.
- KIM, M.C. & CHOI, C.K. 2011 The stability of miscible displacement in porous media: nonmonotonic viscosity profiles. *Phys. Fluids* **23** (8), 084105.
- KIM, M.C. & CHOI, C.K. 2012 Linear stability analysis on the onset of buoyancy-driven convection in liquid-saturated porous medium. *Phys. Fluids* **24** (4), 044102.
- KIM, M.C. & KIM, S. 2005 Onset of convective stability in a fluid-saturated porous layer subjected to time-dependent heating. *Int. Commun. Heat Mass* **32**, 416 – 424.
- KIM, M. C. & CHOI, C. K. 2007 Relaxed energy stability analysis on the onset of buoyancy-driven instability in the horizontal porous layer. *Phys. Fluids* **19**, 088103.
- KUMAGAI, A. & YOKOYAMA, C. 1998 Viscosities of aqueous solutions of CO₂ at high pressures. *Int. J. Thermophys.* **19**.
- KUMAGAI, A. & YOKOYAMA, C. 1999 Viscosities of aqueous nacl solutions containing co₂ at high pressures. *J. Chem. Eng. Data* **44**, 227–229.
- LAPWOOD, E. R. 1948 Convection of a fluid in a porous medium. *Proc. Cambridge Philos. Soc.* **44**, 508–521.
- LICK, WILBERT 1965 The instability of a fluid layer with time-dependent heating. *J. Fluid Mech.* **21** (03), 565–576.
- MACMINN, C. W., NEUFELD, J. A., HESSE, M. A. & HUPPERT, H. E. 2012 Spreading and convective dissolution of carbon dioxide in vertically confined, horizontal aquifers. *Water Resour. Res* **48** (11).

- MANICKAM, O. & HOMSY, G. M. 1995 Fingering instabilities in vertical miscible displacement flows in porous media. *J. Fluid Mech.* **288**, 75–102.
- McKIBBIN, R. 1986 Heat transfer in a vertically-layered porous medium heated from below. *Transport Porous Med.* **1**, 361–370.
- McKIBBIN, R. & O’SULLIVAN, M.J. 1980 Onset of convection in a layered porous medium heated from below. *J. Fluid Mech.* **96**, 375–393.
- McKIBBIN, R. & O’SULLIVAN, M.J. 1981 Heat transfer in a layered porous medium heated from below. *J. Fluid Mech.* **111**, 141–173.
- MEULENBROEK, B., FARAJZADEH, R. & BRUINING, H. 2013 The effect of interface movement and viscosity variation on the stability of a diffusive interface between aqueous and gaseous CO₂. *Phys. Fluids* **25**, 074103.
- MORTON, B. R. 1957 On the equilibrium of a stratified layer of a fluid. *J. Mech. Appl. Math.* **10**, 433–447.
- NEUFELD, J. A., HESSE, M., A., RIAZ, A., HALLWORTH, M., A., TCHELEPI, H. A. & HUPPERT, H. E. 2010 Convective dissolution of carbon dioxide in saline aquifers. *Geophys. Res. Lett.* **37**, L22404.
- NEUFELD, JEROME A. & HUPPERT, HERBERT E. 2009 Modelling carbon dioxide sequestration in layered strata. *J. Fluid Mech.* **625**, 353–370.
- NIELD, D. A. 1986 Convective heat transfer in porous media with columnar structure. *Transport Porous Med.* **2**, 177–185.
- NIELD, D. A. & BEJAN, A. 2006 *Convection in Porous Media*, 3rd edn. Springer, New York.
- NOAA-ESRL 2014 CO₂ data from Mauna Loa Observatory, <http://co2now.org>.
- ORR, F. M. 2009 Onshore geologic storage of CO₂. *Science* **325**, 1656–1658.
- PEYRET, R. 2002 *Spectral Methods for Incompressible Viscous Flows*. Springer-Verlag.
- PRASAD, A. & SIMMONS, C. T. 2003 Unstable density-driven flow in heterogeneous porous media: A stochastic study of the Elder [1967b] short heater problem. *Water Resour. Res.* **39** (1).
- PRITCHARD, D. 2004 The instability of thermal and fluid fronts during radial injection in a porous medium. *J. Fluid Mech.* **508**, 133–163.
- RAPAKA, S., CHEN, S., PAWAR, R. J., STAUFFER, P. H. & ZHANG, D. 2008 Non-modal growth of perturbations in density-driven convection in porous media. *J. Fluid Mech.* **609**, 285–303.

- RAPAKA, S., PAWAR, R. J., STAUFFER, P. H., ZHANG, D. & CHEN, S. 2009 Onset of convection over a transient base-state in anisotropic and layered porous media. *J. Fluid Mech.* **641**, 227–244.
- REDDY, S. C., SCHMID, P. J. & HENNINGSON, D. S. 1993 Pseudospectra of the Orr-Sommerfeld Operator. *SIAM J. Appl. Math.* **53** (1), 15–47.
- RIAZ, A. & CINAR, Y. 2014 Carbon dioxide sequestration in saline formations: Part I- Review of the modeling of solubility trapping. *J. Petrol. Sci. Eng.* .
- RIAZ, A., HESSE, M., TCHELEPI, H. A. & ORR, F. M. 2006 Onset of convection in a gravitationally unstable diffusive boundary layer in porous media. *J. Fluid Mech.* **548**, 87–111.
- RIAZ, A. & MEIBURG, E. 2004 Vorticity interaction mechanisms in variable-viscosity heterogeneous miscible displacements with and without density contrast. *J. Fluid Mech.* **517**, 1.
- ROBINSON, J. L. 1976 Theoretical analysis of convective instability of a growing horizontal thermal boundary layer. *Phys. Fluids* **19**, 778–791.
- SCHINCARIOL, R. A. 1998 Dispersive mixing dynamics of dense miscible plumes: natural perturbation initiation by local-scale heterogeneities. *J. Contaminant Hydrology* **34** (3), 247–271.
- SCHINCARIOL, R. A., SCHWARTZ, F. W. & MENDOZA, C. A. 1997 Instabilities in variable density flows: Stability and sensitivity analyses for homogeneous and heterogeneous media. *Water Resour. Res.* **33** (1), 31–41.
- SCHMID, P. J. 2007 Nonmodal stability theory. *Annu. Rev. Fluid Mech.* **39**, 129–162.
- SELIM, A. & REES, D. A. S. 2007*a* The stability of developing thermal front in a porous medium. I. Linear theory. *J. Porous Media* **10**, 1–16.
- SELIM, A. & REES, D. A. S. 2007*b* The stability of developing thermal front in a porous medium. II. Nonlinear evolution. *J. Porous Media* **10** (1), 17–34.
- SIMMONS, C. T., FENSTEMAKER, T. R. & SHARP, J. M. 2001 Variable-density groundwater flow and solute transport in heterogeneous porous media: approaches, resolutions and future challenges. *J. Contaminant Hydrology* **52** (1-4), 245–275.
- SLIM, A.C. & RAMAKRISHNAN, T.S. 2010 Onset and cessation of time-dependent, dissolution-driven convection in porous media. *Phys. Fluids* **22** (12), 124103.
- SLIM, A. C., BANDI, M. M., MILLER, JOEL C., & MAHADEVAN, L. 2013 Dissolution-driven convection in a Hele-Shaw cell. *Phys. Fluids* **25**, 024101.

- SPANGENBERG, W. G. & ROWLAND, W. R. 1961 Convective circulation in water induced by evaporative cooling. *Phys. Fluids* **4**, 743–750.
- TAN, C. T. & HOMSY, G. M. 1986 Stability of miscible displacements in porous media: Rectilinear flow. *Phys. Fluids* **29**, 3549–3556.
- TAN, C. T. & HOMSY, G. M. 1992 Viscous fingering with permeability heterogeneity. *Phys. Fluids A* **4** (6), 1099–1101.
- TICHELEPI, H. A. & ORR, F. M. 1994 Interaction of viscous fingering, permeability heterogeneity, and gravity segregation in 3 dimensions. *SPE Reservoir Eng.* **9**, 266–271.
- TICHELEPI, H. A., ORR, F. M., RAKOTOMALALA, N., SALIN, D. & WOUmeni, R. 1993 Dispersion, permeability heterogeneity, and viscous fingering - Acoustic experimental-observations and particle-tracking simulations. *Phys. Fluids A* **5** (7), 1558–1574.
- THEOFILIS, V. 2011 Global linear instability. *Annu. Rev. Fluid Mech.* **43**, 319–352.
- TILTON, N., DANIEL, D. & RIAZ, A. 2013 The initial transient period of gravitationally unstable diffusive boundary layers developing in porous media. *Phys. Fluids* **25**, 092107.
- TILTON, N. & RIAZ, A. 2014 Nonlinear stability of gravitationally unstable, transient, diffusive boundary layers in porous media. *J. Fluid Mech.* **745**, 251–278.
- WESSEL-BERG, D. 2009 On a linear stability problem related to underground CO₂ storage. *SIAM J. Appl. Math.* **70** (4), 1219–1238.
- WHITAKER, S. 1999 *The Method of Volume Averaging*. Kluwer Academic Publishers.
- WOODING, R. A., TYLER, S. W. & WHITE, I. 1997 Convection in groundwater below an evaporating salt lake: 1. Onset of instability. *Water Resour. Res.* **33** (6), 1199–1217.
- XU, X., CHEN, S. & ZHANG, D. 2006 Convective stability analysis of the long-term storage of carbon dioxide in deep saline aquifers. *Adv. Water Resour.* **29**.
- ZHANG, H. R., SORBIE, K. S. & TSIBUKLIS, N. B. 1997 Viscous fingering in five-spot experimental porous media: New experimental results and numerical simulations. *Chem. Eng. Sci.* **52**, 37.